On-Chip Engineered Human Lymphatic Microvasculature for Physio-/Pathological Transport Phenomena Studies

by

Jean Carlos Serrano

B.S. Mechanical Engineering, University of Puerto Rico at Mayaguez (2016)
S.M. Mechanical Engineering, Massachusetts Institute of Technology (2018)

Submitted to the department of mechanical engineering in partial fulfillment of the requirements for the degree of

DOCTOR OF PHILOSOPHY IN MECHANCIAL ENGINEERING
at the
MASSACHUSETTS INSTITUTE OF TECHNOLOGY

JUNE 2021

Signature of Author: _____

Department of Mechanical Engineering
April 30, 2021

Certified by: _____

Roger D. Kamm
Professor of Mechanical Engineering
Professor of Biological Engineering
Thesis Supervisor

Accepted by: _____

Nicholas G. Hadjiconstantinou
Professor of Mechanical Engineering
Graduate Officer

On-Chip Engineered Human Lymphatic Microvasculature for Physio-/Pathological Transport Phenomena Studies

by

Jean Carlos Serrano

Submitted to the Department of Mechanical Engineering
on April 30, 2021 in Partial Fulfillment of the Requirements for the Degree of

Doctor of Philosophy in Mechanical Engineering

ABSTRACT

In addition to the blood vasculature, the majority of tissues contain a secondary vascular system known as the lymphatics that supports tissue homeostasis and immune cell trafficking. As such, impairment of the lymphatic capillaries can result in diverse diseases including abnormal tissue swelling (edema) and compromised immunity, while their excessive growth in the tumor microenvironment facilitates cancer metastasis. Current *in vitro* models for the lymphatic vasculature, in health and disease, mostly rely on monolayer and transwell culture systems which only lend themselves to reductionist studies with a considerable lack of physiological relevance. In comparison, animal models provide the full spectrum of biological complexities; however, they offer limited control over biological events in the cellular microenvironment, thus making it increasingly difficult to conduct and interpret results from mechanistic studies. To address these limitations, we developed a 3D lymphatic microvasculature model, that physiologically emulates the lymphatic structure and function, within a microfluidic system that allows for high spatial-temporal control over the biological transport phenomena to study cellular events.

For the first part in this thesis, we implemented a microfluidic-based cell culture system to screen for the optimal balance of growth factors, extracellular matrix composition and interstitial fluid flow that would induce controlled-levels of angiogenic sprouting by the lymphatic endothelial cells. From this study, we developed two distinct approaches to generate 3D lymphatic microvasculature on-chip in which lymphangiogenesis is achieved by diffusive exposure to growth factors or via a mechanotransduction response to high levels of interstitial fluid flow. After validating the *in vivo*-like morphology of our engineered lymphatics, we quantified their solute drainage functionality using fluorescent tracers of varying molecular weights, resembling interstitial soluble proteins. Results validated that the lymphatic microvasculature exhibited solute drainage rates approaching *in vivo* lymphoscintigraphy standards. Computational and scaling analyses were performed to understand the underlying transport phenomena which elucidated the importance of a 3D geometry and the lymphatic endothelium to recapitulate physiological drainage. We then examined the capability of our on-chip lymphatics to elicit an immune response under a pathological-inflammatory condition by locally recruiting immune cells. Experimental and computational results demonstrate an increased infiltration of immune cells into the lymphatics guided by chemotactic gradients that trigger the CCR7-CCL21/19 and CXCR4-CXCL12 inflammatory axes. Finally, we demonstrate the utility of our microphysiological system for pre-clinical studies, specifically by screening the vascular absorption rate of therapeutic monoclonal antibodies developed by Amgen Inc. We coupled our experimental measurements with a physiological-based analysis to describe their systemic transport which allowed us to quantitatively assess their corresponding pharmacokinetics.

Keywords: lymphatics, microfluidics, tissue engineering, transport phenomena

Thesis Committee:
Roger D. Kamm, Professor of Mechanical and Biological Engineering, MIT (Thesis Advisor)
Alan J. Grodzinsky, Professor of Mechanical, Biological Engineering and EECS, MIT
Ming Guo, Professor of Mechanical Engineering, MIT

Acknowledgements

The journey undertaken to finish a PhD is undoubtedly one of the most memorable experiences in a lifetime, but even more memorable are the people that stand by your side during this odyssey. The first to be recognize for such is Roger Kamm, whom I owe every opportunity to grow as scientist and engineer during my time at MIT. I will notably remember Roger's incredible patience, kindness and humbleness as my advisor, and with whom I had the most insightful conversations and lessons on biological fluid mechanics and transport phenomena. However, my particular interest to work on those topics came from what was undoubtedly the most fascinating class I've taken, Field, Forces and Flows, taught by Al Grodzinky, who has been the most engaging and committed teacher that I've had the pleasure to learn from. And to my other thesis committee member, Ming Guo, with whom I always felt energized and motivated to pursue the most ambitious research questions after every chat we had. I am sincerely grateful for their academic support, and challenging me to become a better researcher.

I owe a special thanks to all the Kammsters, who not only became colleagues and collaborators but also mentors that introduced me to the experimental techniques in the lab and provided invaluable guidance throughout my work. A special mention goes to my first officemates: Vivek Sivathanu, Jordy Whisler and Ran Li who constantly supported and cheered me through my first year at MIT. In particular, Ran who became my first mentor at MIT, without the obligation to do so, and eventually a dear friend. A special thanks also goes to: Mark Gillrie, Tatsuya Osaki, Tina Haase, Alex Boussommier, Michelle Chen, and many other Kammsters that helped me along the way. Last but definitely not least, I'm immensely grateful for the friendships I was able to build with Giogi Offeddu and Cynthia Hajal, thank you both for your endless support and kind gestures.

I also want to thank those special friends at MIT that helped get through courses, quals, and everyday life as a grad student, especially Claudia Varela, Peter Godart, Dan Oropeza, Ashley Beckwith, Carlos Barajas, Ricardo Baptista and German Parada.

I'm also extremely grateful for my fellow "Boricuas", both back home and here at Boston, that helped through my transition from the warmth of Puerto Rico to living in the forever-cold weather at Boston. I will forever be proud of being part of this amazing community and thankful for the moments that we share together as "Boricuas". A special shout out goes to Tiara Rodriguez, Luis Rosa, Baldin Llorens, Juan Antonio, Benito Antonio Martinez (aka Bad Bunny), and my best bro, Pedro Colon.

Finally, I owe everything that I've been able to achieve in my life to the unconditional love and support from my amazing family, in particular my parents and sister. I will be forever in debt to my parents, for their countless sacrifices to provide me with the best education they could afford, and for supporting me at every stage of my academic career. I dedicate this thesis to you both.

Table of Contents

Chapter 1: Introduction, Background and Motivation

1.1 Physiology and Relevance of the Lymphatic Vascular System

In addition to the blood vasculature, we contain a secondary vascular system known as the lymphatics (**Figure 1**). In similar aspects to the blood vascular system, the lymphatics are an elaborate, hierarchal network of vessels lined by endothelial cells that serve as conduits for fluid, protein and cellular transport[1]. However, despite these physical similarities, their physiological function and organization are quite distinctive. Conversely to the blood vascular system where fluid is continuously recirculating through different tissues, the lymphatic system operates as a one-way transport system that collects fluid, proteins and cells from the interstitial space of tissues and returns them to the systemic circulation[2]. Under this mechanism, lymphatics regulate fluid and osmotic pressure homeostasis in tissues. Furthermore, the lymphatic system acts as an immune checkpoint by transporting antigen and antigen-presenting cells from the interstitial tissue to the lymph node, where housed immune cells respond to localized or systemic inflammation and infections[3]. In addition, there are organ-specific lymphatic vessels that have unique functions such as the lymphatic vessels inside the intestinal villi that are responsible for absorbing dietary fats[4].

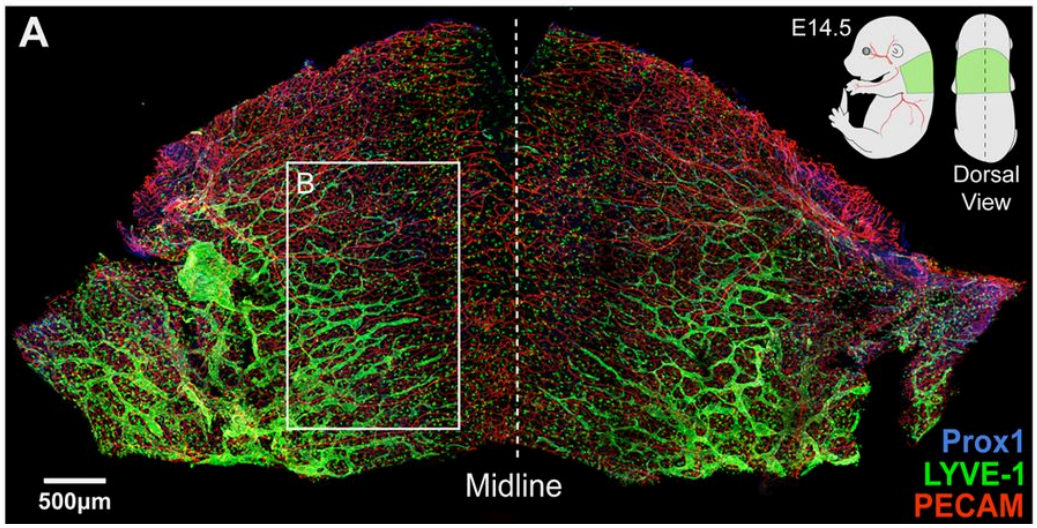

Figure 1: Dermal histological section depicting the native vascular environment with blood (PECAM-Red) and lymphatic vasculature (LYVE1-Green/Prox1-Blue). Modified from James et al.[5]

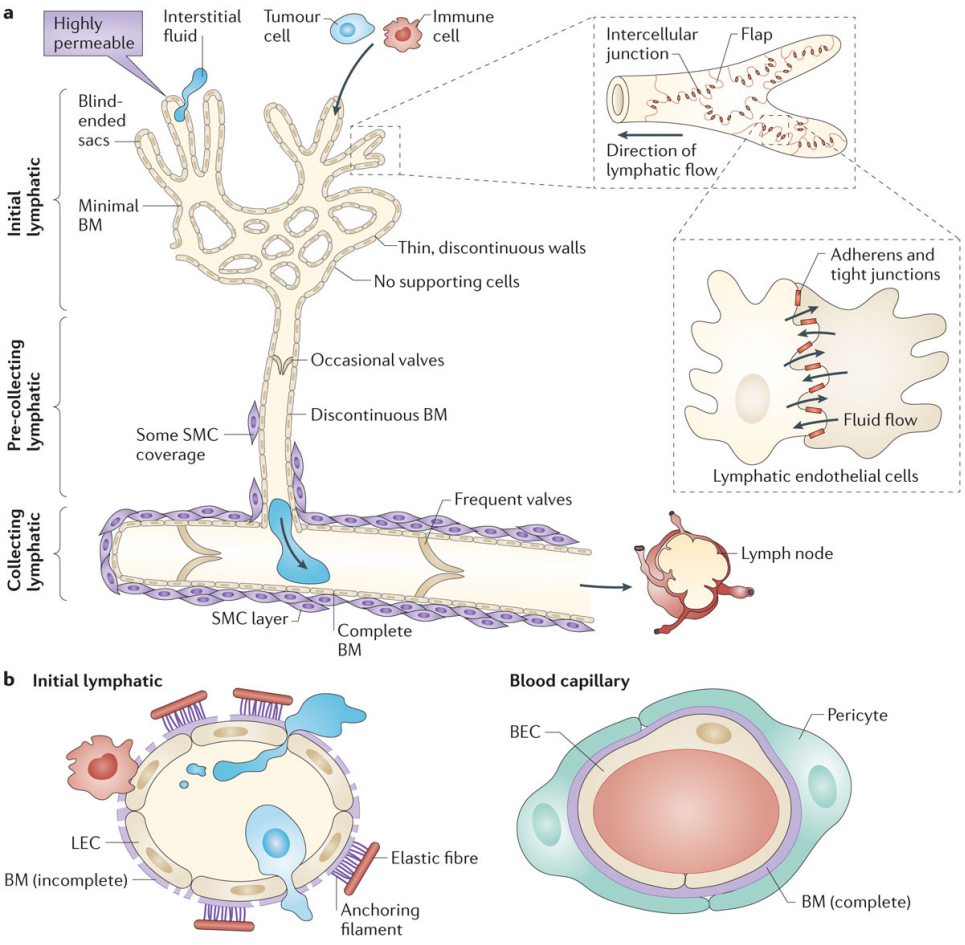

Figure 2: Anatomy and organization of the lymphatic vascular system. Modified from Stacker et al.[6]

The unique architecture and organization of the lymphatic system facilitates their physiological functionality to recover fluid, solutes and cells that have percolated from the systemic circulation[7]. The lymphatic system is initially composed of an intricate network of blind-ended capillaries, also called initial lymphatics, interlaced between blood capillaries and responsible for draining interstitial fluid and its diluted contents (also known as lymph) from the extracellular space of tissues (**Figure 1**). The lymph then travels into the collecting lymphatics, which are double-lined vessels, with lymphatic endothelial cells in the inner surface and smooth muscle cells on the outer surface, that actively contract to assist in the drainage of fluid[8]. Additionally, to avoid the backflow of the collected lymph, these lymphatic vessels have multiple locations along their extent with one-way opening valves. Finally, the collected fluid, with proteins and immune cells, reaches the lymph nodes where interstitial fluid is filtered in terms of foreign particles and harmful pathogens[9].

Additionally, the lymph nodes house numerous adaptive immune cells (such as B cells and T cells), which are activated when certain antigens or antigen-presenting cells are brought to them[10]. The filtered lymph fluid is then returned into circulation through lymph ducts connected to the venous circulation. Overall, this process prevents the excessive accumulation of interstitial fluid and proteins in surrounding tissues, and, in cases of infections, the lymph nodes release lymphocytes into the blood stream to address the pathogens[11].

Fundamentally, these key functions, contributed by the lymphatic vasculature, are dependent on the orchestrated fluid transport initiated at the lymphatic capillaries (**Figure 2**). These vessels are one continuous layer of lymphatic endothelial cells, about 10-50 microns in diameter, with few localized intercellular junctions, typically referred to as button-like junctions[12,13]. In contrast to blood capillaries, lymphatic capillaries are devoid of pericyte-coverage and have a discontinuous basement membrane. Additionally, the lymphatic endothelial cells, at the capillaries, are attached to the extracellular matrix by anchoring filaments which connects the cells' basal lamina to adjacent extracellular matrix fibers, thus allowing them to collapse when there is high fluid pressure in the interstitial tissue[14]. These particular attributes allow the lymphatic capillaries to be highly permeable to solutes, proteins and migrating cells, as well as to intake large volumes of interstitial fluid[15,16].

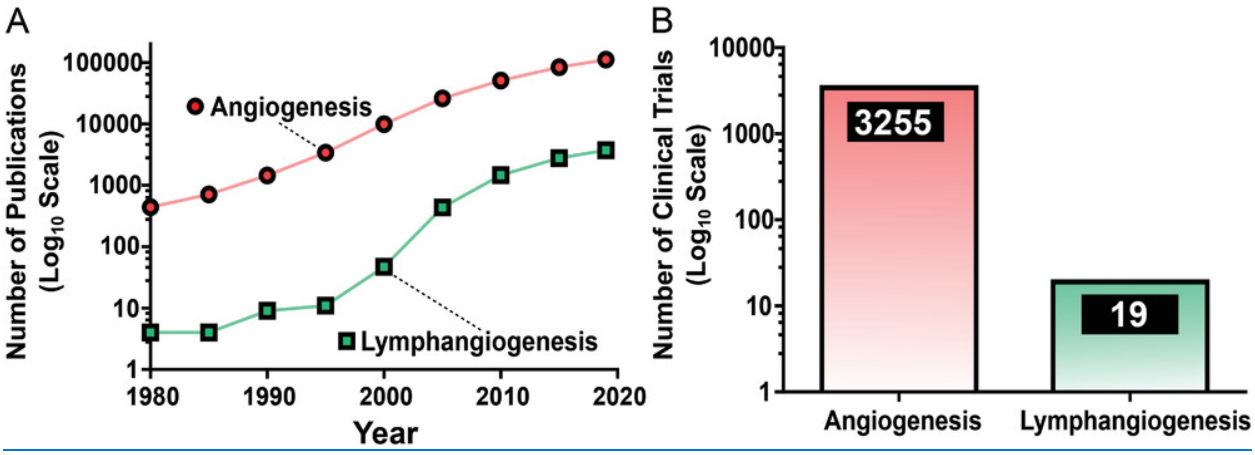

Figure 3: (A) Plot of the number of cumulative publications over the years regarding angiogenesis or lymphangiogenesis. (B) Log plot of the number of clinical trials to date implementing angiogenesis or lymphangiogenesis. Modified from Campbell et al.[17]

Interestingly, the biological phenomena by which these capillaries originate (angiogenesis and vasculogenesis) is not limited to developmental and wound healing scenarios. Lymphatic angiogenesis (lymphangiogenesis) is also known to occur in pathological settings, such as the tumor microenvironment, and plays a crucial role in the progression of diseases[18,19]. Similarly to blood capillaries, local causes in the pathological environment can lead to abnormal morphology and impaired function of lymphatics that can result in serios heath conditions such as lymphedema[20], impaired immunity[21] and cancer metastasis[22]. Despite corresponding to imperative physiological functions and pathological response, the lymphatic system has been historically understudied, compared to blood vascular research[17] (**Figure 3**). In fact, clinical trials for therapies exploiting lymphangiogenesis for regenerative medicine applications are drastically falling behind by considerable orders of magnitude[17] (**Figure 3**). One of the overriding challenges in lymphatic-focused research has been the lack of experimental models that facilitate studies to interrogate biological mechanisms implicated in lymphatic development, physiology and disease.

1.2 In Vitro-Based Studies on Lymphatic Morphogenesis and Function

Animal models have served as the gold standard to evaluate the biological function of lymphatics, as well as its implications in pathological phenomena such as inflammation, pathogen response and cancer progression [23–25]. Despite fully recapitulating the physiological responses, *in vivo* models offer limited control over the local environmental cues, thus adding difficulties to decouple their effects, as well as adding difficulty to isolate the direct and indirect systemic effects of the modulated parameters. Alternatively, numerous groups have implemented *in vitro* system to perform reductionist studies and isolate the individual contribution of the regulated cues in the cellular microenvironment. Under this approach, key studies have been published that have broaden our understanding on the role and significance of lymphatics in different biological events. For example, the underlying factors that drive lymphatic endothelial cell differentiation have been identified including the upregulation in the expression of Prospero homeobox 1(PROX-1) [26] and lymphatic vessel endothelial hyaluronan receptor 1 (LYVE-1) [27] coupled with an increase of distinctive tyrosine kinase receptors, such as VEGF receptor-3 [28]. Additionally, in a pathological context, the underlying molecular mechanisms that drive lymphatic sprouting has been mostly

attributed to VEGF receptor-3 activated by vascular endothelial growth factors (VEGF-C and VEGF-D) while an increase of endogenous transforming growth factor-β (TGF-β) has been shown to suppress lymphangiogenesis[29]. Other *in vitro* studies have shown the influence of flow-induced shear stress on lymphatic endothelial cell behavior [30]. For instance, the Swartz lab has extensively studied the effects of interstitial flow on lymphatic endothelial cells, and demonstrated unique sprouting and morphogenetic responses controlled by this stimulus [31,32], with, more recently, changes in their ability to transcellularly transport solutes [33]. In another study by Petrova and colleagues, monolayers of lymphatic endothelial cells exposed to oscillatory fluid flow leaded to the stabilization of the cells' cytoskeleton and intercellular junctions which was molecularly mediated by the transcriptional activation of FOXC2 [34]. In addition to probing the direct response on lymphatics, *in vitro* platforms have been implemented to investigate the influence of lymphatic endothelial cells on the behavior of other cell types. For example, a key study by Shields. et al. demonstrated an autologous chemotaxis mechanism that drives the migration of cancer cells and is exacerbated by the presence of a lymphatic endothelium [35]. While another recent study by Brown et al. showed that inflammatory-driven lymphatic exosomes increases the migration behavior of dendritic cells which correlates to lymphatic-mediated immune response [36].

Altogether, these *in vitro* assays, coupled *with in vivo* models, have provided fundamental insight into the biology of lymphatics. However, these *in vitro* studies provide a limited scope of physiological mimicry, while animal models impose limits on the ability to perform parametric studies. Therefore, there is a high demand for next generation platforms that provides a higher degree of physiological relevance compared, to traditional *in vitro* systems, while facilitating the tight control over the local biochemical and biophysical cues. Under this effort, microfluidic technologies have emerged as a possible solution to these limitations.

1.3 Engineering Strategies for On-Chip Vascularization

During the last two decades, microfluidic technologies have attracted the attention of the biological community by finding numerous applications in fundamental biomedical studies [37,38] to diagnostics and personalized medicine [39,40]. More specifically, microfluidic cell culture systems provide precise control over the geometrical features of the cellular microenvironment to model

tissue organization and hierarchy, as well as high spatial and temporal control over the biochemical and biomechanical factors integrated in the system[41] (**Figure 4**). With these advantages, researchers have leveraged the tight microenvironment control to decouple the specific contribution biochemical and biophysical signals during cell migration and tissue morphogenesis [42].

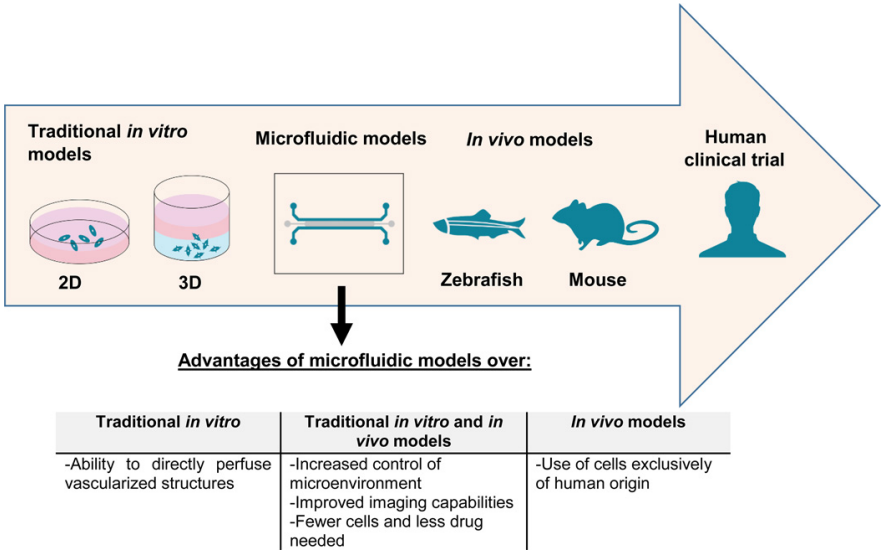

Figure 4: Overview of the various types of research models and the potential advantages microfluidic platforms compared to traditional *in vitro* models and *in vivo* models. Modified from Boussommier et al.[41]

In terms of vascular biology, the key features provided by microfluidic platforms are well-tailored to increase the physiological relevance of these studies such as precise geometrical patterning of the microvascular environment, high-resolution imaging of vascular morphogenesis events and the ability to perform functional studies [43]. Engineering approaches to integrate a microvasculature on-chip, include two distinctive methods: cellular patterning and self-assembly (**Figure 5**). Early attempts to engineer a vascular bed within a microfluidic system relied on casting methods (predesigned microfluidic channels[44] or sacrificial molding [45]) to define the vascular architecture where endothelial cells are introduce to form a confluent monolayer around the patterned features. However, a major limitation faced by these patterning methods comes from the large-scale geometry they generate (in the order of hundreds of microns) which lack the appropriate size of *in vivo* capillaries. Additionally, the artificial fabrication by which these *in vitro* vasculatures are engineered does not ensure their physiological functionality (endothelial barrier function and cell-secreted factors). In an alternate approach, recent research has relied on the self-assembly

phenomena by endothelial cells (angiogenesis[46] and vasculogenesis[47]) to create microvasculature on-chip (**Figure 5**). By this approach, researchers can engineer capillaries that more closely resemble vascular structures found *in vivo,* while facilitating their ability exhibit physiological functionality (high barrier function and paracrine signaling).

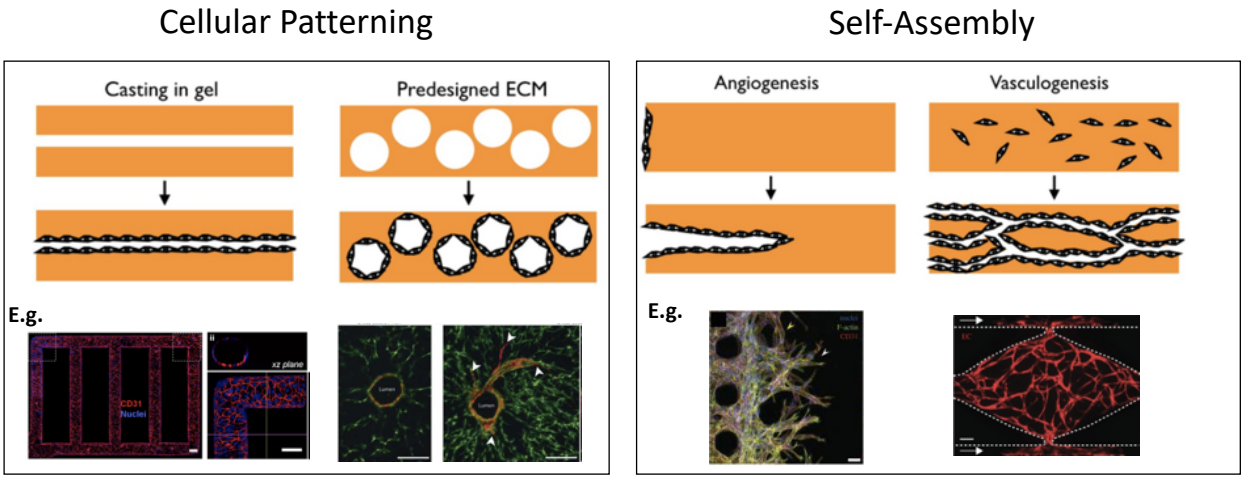

Figure 5: Examples of on-chip vascularization strategies. Modified from Miura et al.[43]

However, studies implementing microfluidic systems to generate lymphatic vasculature are extremely scarce. Apart from simple monolayer systems that lack anatomical resemblance [48], less than a dozen published works have attempted to recreate the native lymphatic vasculature on-chip. A recent study by Tien and colleagues utilized needle-based sacrificial molding to engineer a single lymphatic capillary in a microfluidic system to study its solute and fluid drainage functionality [49]. In a similar approach, Beebe and colleagues have published several works implementing a single lymphatic capillary on-ship to study solute permeability, and paracrine signaling/conditioning between lymphatic and fibroblast/tumor cells[50,51] (**Figure 6**). However, these platforms have limited utility to study lymphatic function given their overly-simplistic, single-capillary system which completely lacks tissue-scale functionality. In an alternate approach, Jeon and colleagues achieved the self-organization of multiple lymphatic capillaries by the induction of angiogenesis, through simultaneous biochemical and mechanical factors, in a microfluidic system with multiple gel channels for fibroblast co-culture[52]. Such study validated the implementation of a lymphangiogenesis approach to generate *in vivo*-like lymphatic sprouts, within the microfluidic gel region, that also resembled the lymphatic capillary blind-ended structure since the sprouts did

not fully extend across the gel region (**Figure 6**). In a follow up work[53], lymphatic sprouting was potentiated towards a middle gel region, in their microfluidic system, containing a tumor spheroid, with the opposite side of the tumor compartment having blood vascular angiogenic sprouts; thus, recapitulating both angiogenic and lymphangiogenic invasion in a tumor microenvironment model. In their latest work[54], Jeon and colleagues generated lumenized lymphatic structures through vasculogenesis in a microfluidic system that also integrated melanoma tumor cells, and/or blood microvascular networks. In this study, they also validated the immune response of cytotoxic lymphocytes that trans-migrated though the lymphatic endothelium to attack the cancer cells, thus mimicking anti-tumor immunology in their on-chip system. While these studies provide significant progress in the development of physiologically-relevant lymphatic *in vitro* systems, they still lack fundamental efforts towards fully validating the physiological functionality of a tissue-scale lymphatic engineered vasculature.

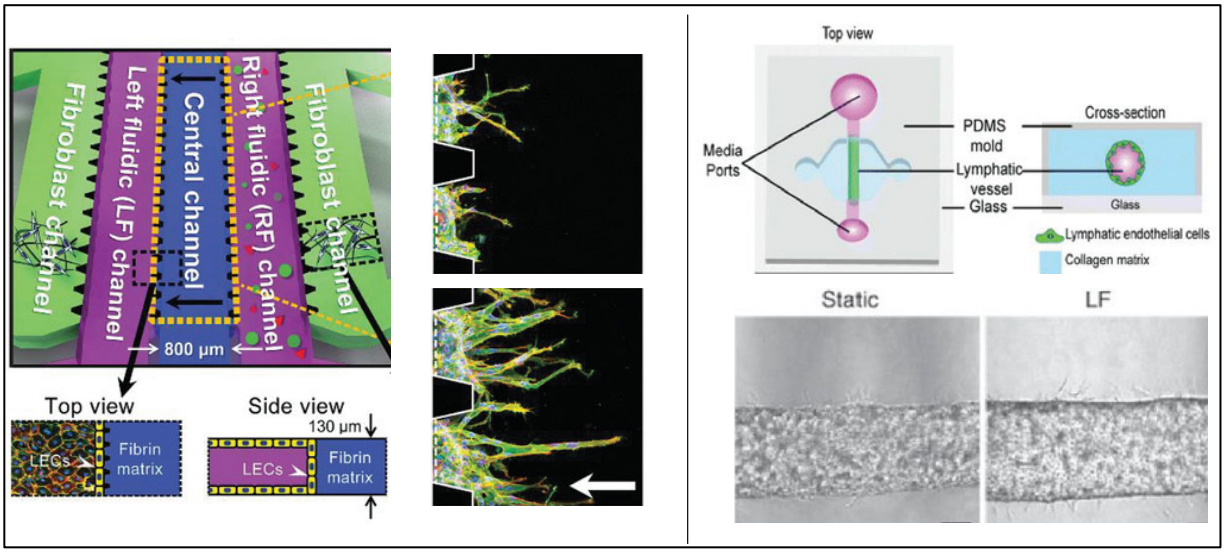

Figure 6: Examples of on-chip systems to generate lymphatic capillaries, by either lymphangiogenic-induction[52] (left) or pre-patterning a collagen-based vascular microchannel[50] (right).

To the best of our knowledge, no published work to date has exploited controlled lymphangiogenic-induction in a microfluidic system to generate a lymphatic microvascular bed with tissue-level functionality. Such work would first require an optimized tissue engineering protocol to generate the on-chip lymphatic capillaries that mimic their *in vivo* counterpart, followed by the functional characterization of the fluid and solute drainage capabilities by the

engineered lymphatics. Additionally, other functional capabilities could be studied such as cell trafficking through the lymphatics during pathological events. After validating the physiological attributes of the on-chip lymphatics, we could then implement such system to dissect biological mechanisms underlying lymphatic function in health and disease, as well for pre-clinical studies to predict human-physiological response to drugs and therapeutics biologics.

1.4 Thesis Objectives and Overview

From our previous discussion, we underscore that current *in vitro* technologies to study lymphatic physiology/pathology have limited capabilities to recapitulate the structural and functional complexities corresponding to their native *in vivo* microenvironment. As such, the majority of *in vitro* studies on lymphatic development and function have been restricted to the experimental capabilities of transwell and 2D gel systems. In fact, even the most advanced platforms to date, based on microfluidic technologies, are limited to functional studies on the basis of a single-capillary system or a lymphangiogenesis system lacking functional characterization. Taken together, this technological gap led to the objectives of this thesis, which broadly consist of improving upon the existing microfluidic techniques to generate physiologically-relevant lymphatic microvasculature with tissue-level functionality. Such a platform would have the versatility to be implemented for fundamental biological studies, as well as drug screening applications regarding the role and function of lymphatic capillaries in different physiological and pathological settings.

To achieve these goals, we leveraged the unique capabilities offered by our previous microfluidic systems, such as exerting precise control over the transport phenomena in the cellular microenvironment to recapitulate the adequate conditions for lymphatic vascularization. Additionally, due to its optical transparency, our system facilitates real-time assays, based on the fluorescent signals, of interacting cells and soluble interstitial proteins. In **Chapter 2**, we address the first objective of this thesis which was to systematically study the influence of both biochemical and biomechanical factors, known to modulate lymphangiogenesis. From this study, we were able to identify the optimal combination of growth factors, extracellular matrix and interstitial flow for generating lymphatic vascular structures that closely mimic those found *in vivo*. Following morphological validation, we demonstrate the vascular functionality of the engineered lymphatics

by quantifying its ability to drained interstitial solutes in **Chapter 3**. Additionally, we developed a computational framework to understand the transport phenomena underlying increased solute drainage in our system. We continue to functionally characterize our on-chip lymphatics in **Chapter 4**, where we validate their ability to elicit an increase recruitment of immune cells through key chemotactic gradients, in response to inflammatory signals. In **Chapter 5**, we extend the capabilities of our system as a pre-clinical model to screen for the absorption, and corresponding pharmacokinetics of therapeutic monoclonal antibodies developed by our industry collaborator. Finally, **Chapter 6** provides concluding remarks of our presented work as well as the future direction and applications. In particular, we provide examples of biological questions or phenomena that can uniquely be answered by the implementation of the on-chip lymphatics platform developed in this thesis.

Chapter 2: Engineering on-chip human lymphatic microvasculature under controlled biochemical and biomechanical stimuli

2.1 Microfluidic device implementation and transport phenomena characterization

Microfluidic systems provide a unique set of advantages over traditional *in vitro* systems, especially in terms of recapitulating key physical and biochemical features of the cellular microenvironment[41,55,56]. This is of special interest for the present study since our principal approach to engineer the lymphatic vasculature relies on introducing the appropriate environmental cues that will facilitate the self-organization of lymphatic capillaries, with lymphatic endothelial cells introduced into the system under no prior patterning of vascular structures. The device implemented in this work was based on earlier designs from our lab with three, parallel fluid channels[57–59] (**Figure 7A**) The middle channel is lined by a series of trapezoidal posts at the edges adjacent to the other fluid channels. These provide adequate surface tension to facilitate the compartmentalization of the injected extracellular matrix in the middle region. The side channels are then utilized as medium channels that allow the exchange of nutrients and metabolic waste, as well as to supply growth factors at specific boundaries of the gel region. Additionally, the length scales of the system were optimized to facilitate lymphatic vascularization in the middle, gel channel. For the distance between media channels, which defines the width of the gel region, a length of 1.2 mm was implemented. This length scale is sufficiently short to allow the steady diffusion of growth factors from one media channel to another within several hours (additional analysis on diffusive transport provided below), while providing sufficient distance for the lymphatic cells to generate vascular sprouts in the gel region[57]. On a similar basis, a width of 1 mm was set for the media channels. In regards to the device height, 300 μm was chosen to maximize the three-dimensional space of lymphatic vascularization, while still facilitating high-resolution confocal imaging. Finally, the length of the media-gel interface was extended to 1cm to approach a tissue-relevant scale while still maintaining a small device footprint.

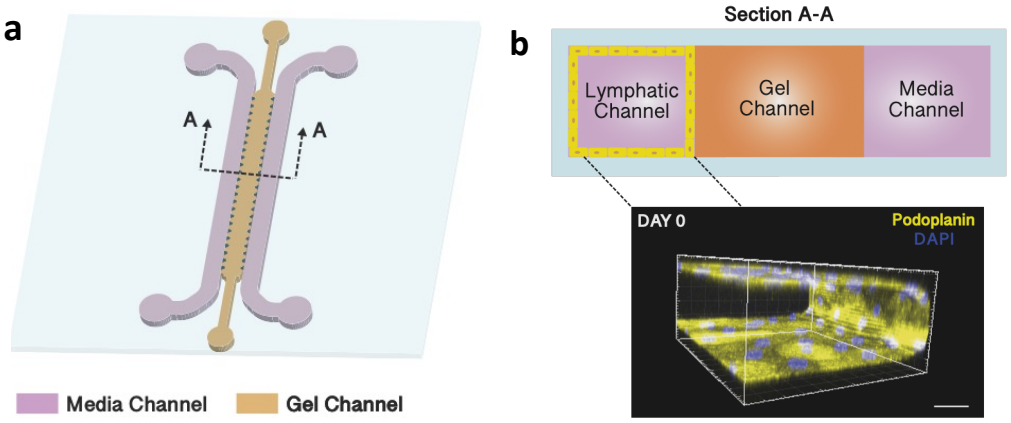

Figure 7: (a) Schematic of the microfluidic device with the corresponding channels labeled. (b) Cross-sectional view of the microfluidic device. Confocal projection of a lymphatic monolayer seeded at the media channel with podoplanin staining the cell membrane and DAPI staining the nuclei. Scale bar is 100 µm.

Microfluidic devices were fabricated via soft lithography from SU-8 coated silicon molds similarly to previous protocols[60,61]. Briefly, molds were prepared by photopolymerizing a 300 µm thick SU-8 photoresist (Micro-Chem, USA) on the silicon wafer. After developing the SU-8 layer, the wafer was silanized overnight in a vacuum desiccator to facilitate the passivation of the surfaces, thus preventing PDMS adhesion during removal. Subsequently, a 10:1 mix of PDMS (Sylgard 184, Ellsworth Adhesives, USA) and curing agent was poured onto the mold, allowed to degas in a desiccator for ~30 min, and polymerized at 70 °C for at least 2 hrs. PDMS was then removed from the mold and cut to individual devices. Scotch tape was used to further clean the surface of the device removing dust and particulates. To allow upper access to the fluid channels, ports were punched using a 1.2 mm biopsy punch for the gel channel, and a 6 mm or 4 mm biopsy punch for the media channels in devices used to grow the lymphatic microvasculature via growth factors or interstitial flow, respectively. After dry sterilization of the devices, the surface was treated with plasma (Harrick Plasma, USA) for 90 seconds, and then bonded to a coverslip slide. After plasma bonding, devices were left overnight to recover hydrophobicity and kept sterile until use.

As aforementioned, the device allows for the compartmentalized culture of cells which will prove to be advantageous for additional biological assays to be carried out in this system. To introduce lymphatic endothelial cells in the systems, we first introduce fibrinogen from bovine plasma

(Sigma) by dissolving it in Dulbecco's Phosphate-Buffered Saline (DPBS, Lonza) at twice the final concentration: 2.5–10 mg/mL for varying fibrin concentration experiments and 5 mg/mL for all other experiments. The fibrinogen solution was then mixed via pipetting, over ice, in a tissue culture hood at a 1:1 ratio with 4 U/mL thrombin to produce a fibrin solution with the desired fibrinogen concentration (1.25–5 mg/mL). The mixture was then pipetted into the device using the gel filling ports, thus providing the three-dimensional extracellular matrix for cell culture. Devices were placed in a humidified enclosure and allowed to polymerize at room temperature for 15 min. Human Plasma Fibronectin (EMD Millipore) was diluted to a concentration of 100 µg/mL in DPBS, prior to being injected in one of the media channels where the cells would be seeded in order to facilitate their adhesion to the walls of the device. While the devices were left incubating with the fibronectin solution for at least 30 min, human dermal lymphatic microvascular endothelial cells (HDLMEC, Lonza, USA) were trypsinized and resuspended to a concentration of 3 x 10^6 cells/mL. After incubation, fresh media was introduced into the fibronectin coated channels and aspirated, to wash away the remaining unbound fibronectin, followed by perfusion of 30 µL of the cell suspension into the channel. Immediately after cell seeding, devices were tilted by approximately 120° and incubated for 15 min to facilitate the agglomeration and adhesion of cells on the gel-media interface. Subsequently, devices were returned to their original position and fresh media was supplemented into the remaining media channel devoid of cells. A pressure height difference of ~4 mm is established between media channels with flow directed from the lymphatic, media channel towards the opposite media channel to further assist the accumulation of cells at the interface. After 24 hours of culture under these conditions, a confluent monolayer of lymphatic endothelial cells forms at the gel media interface (**Figure 7B**) and the remaining unattached cells are aspirated.

In addition to compartmentalized cell culture, the implemented microfluidic system allows for tight control over the transport of biologically relevant molecules (e.g., nutrients, growth factors, antibodies) across the extracellular compartment. To characterize the nature of diffusive transport of such biomolecules, we conducted a diffusion assay[60] in which cell culture media supplemented with 70 kDa-FITC dextran (Sigma) was added to one of the media channels and the middle, gel region was imaged at different time intervals on a confocal microscope (Olympus FV-1000) with custom enclosure for temperature and atmosphere control. 70kDa-dextran was chosen to reflect the molecular weight of growth factors implemented in this work to stimulate the growth of

lymphatics. Fluorescent signal obtained from the images depicted changes in the concentration profile over time due to the diffusive transport of the molecules across the gel[60] . Images were taken at the midplane with a 10x objective, since the concentration profile would be invariant throughout the height of the device, then analyzed using ImageJ (NIH) to extract the fluorescence intensity profile across the width of the gel channel (**Figure 8a**).

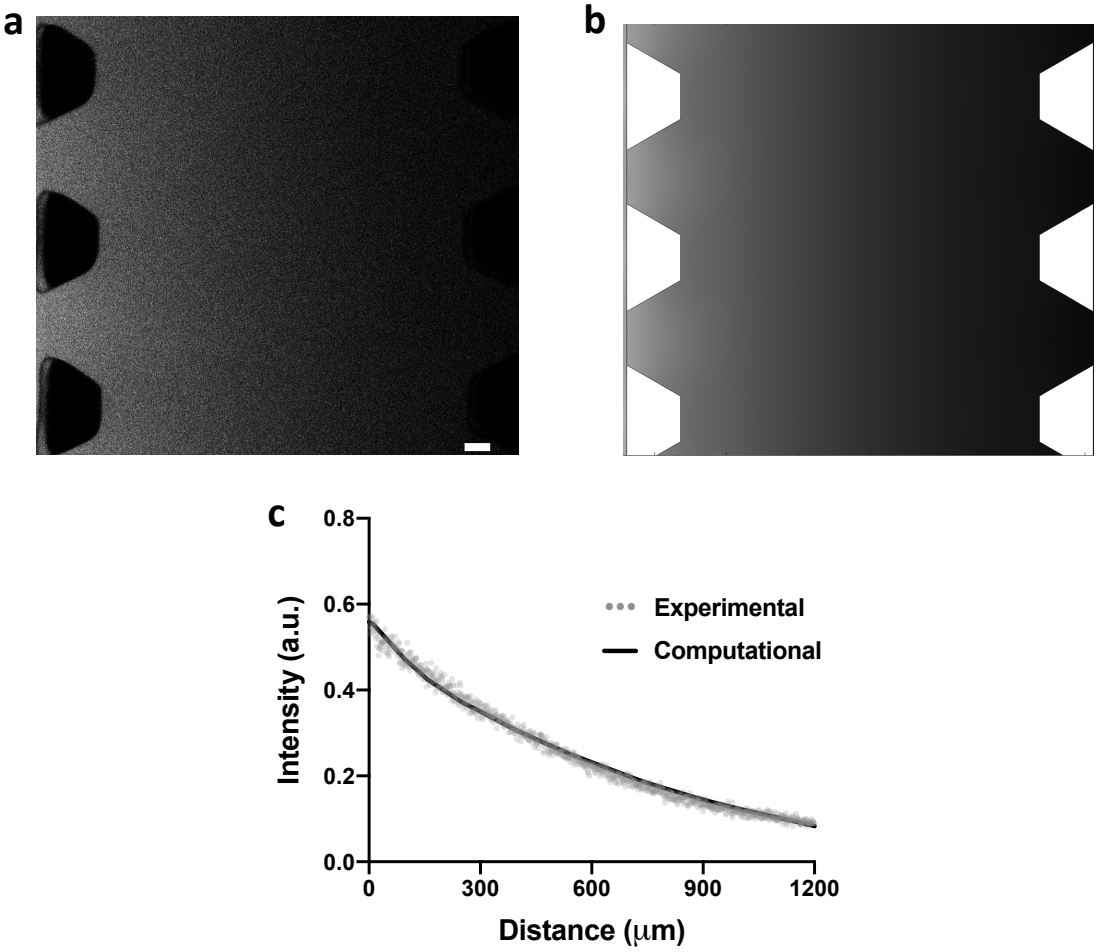

Figure 8: (a) Representative image of the diffusion of fluorescently-balled dextran in the microfluidic device. Scale bar is 50 μm. (b) Grayscale image of the computational model solving for the diffusion profile in the imported CAD of the microfluidic device. (c) Intensity-concentration profile for the experimental and computational data at the same time interval. All data presented correspond to a time interval of 2 hours.

Finite element computational simulations were performed in COMSOL to obtain the diffusion coefficient of the tracer within the gel region. An AutoCAD file (Autodesk, USA) of the device geometry was imported and the model solved Fick's Second Law of Diffusion[60] (**Figure 8b**):

$$\frac{\partial C}{\partial t} = D\frac{\partial^2 C}{\partial x^2}$$

where the time and second order spatial derivative is taken for the molar concentration of the diluted molecule (C) and D corresponds to the diffusion coefficient in a particular medium. Initial, boundary conditions of normalized concentrations $C_{max} = 1$ and $C_{min} = 0$ were applied on the left and right media channels, respectively, on a similar basis as the experimental characterization. Zero flux conditions were imposed on the walls of the device. The diffusion coefficient value was iterated to estimate the corresponding value that best matched the resulting concentration profile across the width of the gel compared to the fluorescence profile from the experimental results at a time interval of 2 hours.

Quantitative comparison of the simulated and experimental results (**Figure 8c**) revealed that the diffusion coefficient within the fibrin gel is approximately 45 $\mu m^2/s$, which is within the range of values measured *ex vivo* for the same fluorescent tracer in tissues[62,63]. Thus, we are able to model physiologically-relevant diffusive transport in our microfluidic system. Furthermore, we can use this parameter to make an order of magnitude estimate of the timescale required for biomolecules, of similar molecular weight, to reach the lymphatic channel by taking the scaling the time as $\sim w^2/D$, where w is the width of the gel channel. By this estimation, we find biochemical factors would steadily diffuse from the source channel within several hours after they are introduced in the system. Since the process of lymphatic vascularization studied in our system occurs over a period of days, this time is sufficiently short to ensure the adequate delivery of growth factors.

In addition to the diffusive transport of growth factors, fluid flow ubiquitously drives biological phenomena including vascular development and function[64–66]. Previous *in vivo* studies have elucidated that interstitial flow facilitates the formation of the lymphatic vasculature during development[67], and, in fact, its absence can lead to dysfunctional lymphatic function (lymphedema)[68]. Furthermore, *in vivo* characterization of interstitial fluid velocities has proven that lower velocities (0.1 – 1 μm/s) correspond to physiological, homeostatic conditions[69], while

higher velocities (4 – 6 μm/s) are indicative of a pathological, inflamed tissue[70,71]. It is in our interest to have the capability to emulate these different flow conditions to enable studies on lymphatic formation and function.

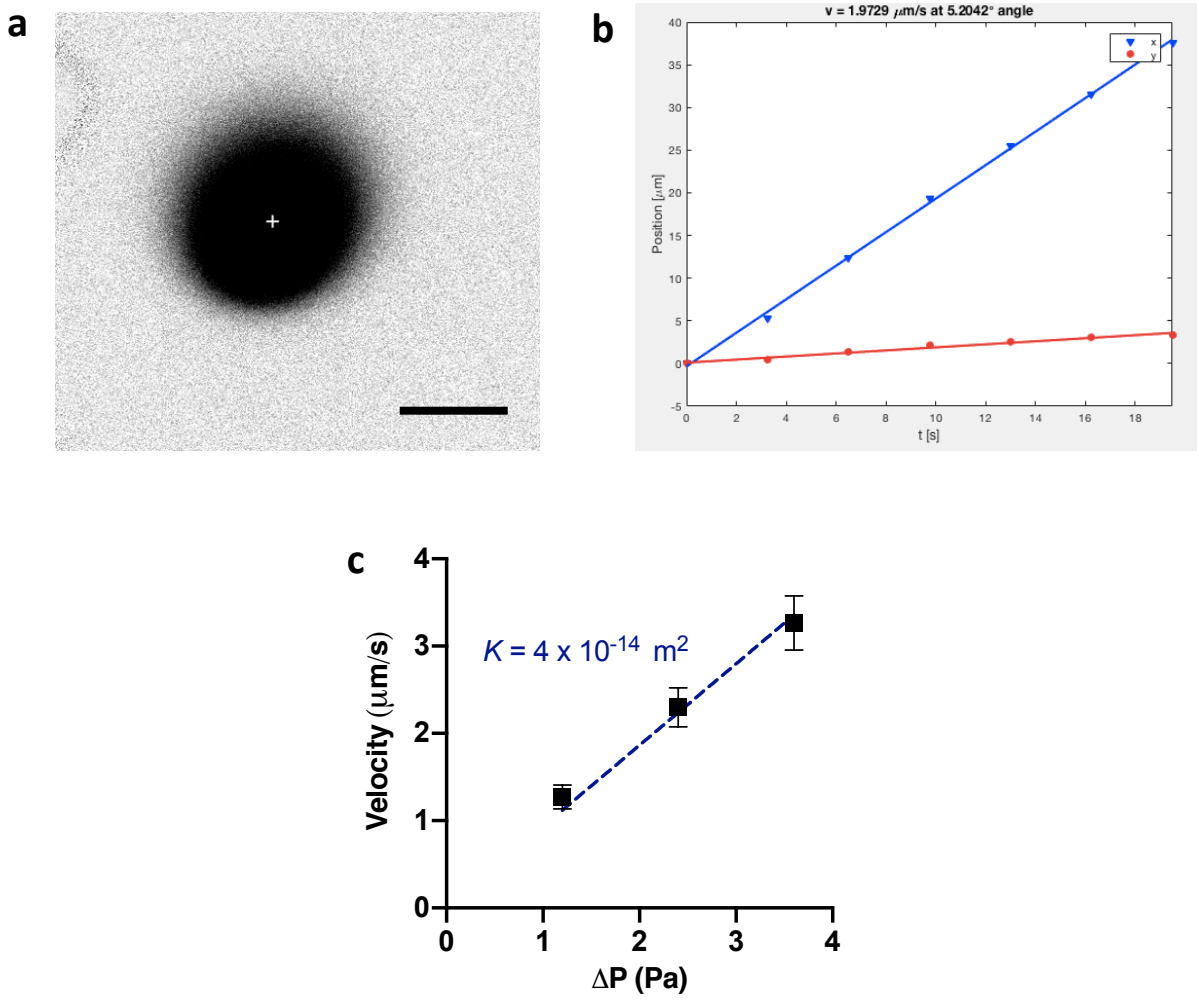

Figure 9: (a) Representative image of a fluorescently bleached spot with centroid identified by the Matlab frap_analysis plugin. Scale bar is 25 μm. (b) Centroid position with respect to time, and estimation of centroid velocity and angle of translation. (c) Interstitial flow velocity as a function of the pressure differential. The linear fit applied is based on Darcy's law to extract the hydraulic permeability (*K*) of the gel.

The dual media channel configuration in our microfluidic platform uniquely allows us to establish a hydraulic-driven pressure difference across the gel region which would potentiate interstitial fluid flow in the ECM. To quantify interstitial fluid velocity accordingly to the established pressure

difference, a variation of the Fluorescence Recovery After Photobleaching (FRAP) technique was implemented as previously reported[72]. Devices were perfused with 70 kDa-FITC dextran supplemented media and left overnight to ensure its uniform distribution throughout the gel. Subsequently, 3 to 5 small regions of interest (ROIs) 30 μm in diameter were photobleached by setting the confocal laser power to 100% for ~5 seconds within the gel matrix. Time-lapse images were captured at 10x immediately after photobleaching every 1.5 seconds. In the presence of a pressure difference, the photobleached area travels across the gel matrix towards the lower pressure source. By measuring the translation of its centroid using the MATLAB frap_analysis plugin[73], we can extract the interstitial fluid velocity accordingly to the pressure head difference (**Figure 9**). The efficacy of this technique to measure fluid velocities relies on the following assumptions: (1) the tracer molecule follows fluid streamlines with no hindrance from the gel matrix, which remains valid given the nanometric scale of the molecule compared to the microscale pore size of the fibrin matrix[74], and (2) the photobleached area travels in a uniform flow field, which is also valid since the length scale over which the pressure gradient is balanced is orders of magnitude larger than the pore size of the gel matrix ($w >> K^{0.5}$); thus, the pressure gradient is balanced by Darcy's averaged velocity instead of the Laplacian velocity[75]. This measurement was repeated as the hydraulic head was increased to obtain an experimental trend between the pressure offset (Δp) and interstitial flow velocity (u) which was then fitted to Darcy's law[73], thus allowing the estimation for the hydraulic permeability of the gel (K) given by:

$$K = \frac{w\,\mu\,u}{\Delta p}$$

where w indicates the length over which the pressure drop is imposed (gel channel width), and μ corresponds to the fluid viscosity taken as 0.78 cP from previous studies[76]. From the obtained data and linear fit to the described equation, we were able to estimate the hydraulic permeability of our implemented fibrin gel to be 4×10^{-14} which is within the magnitude of expected values for *in vitro* engineered ECM[77,78]. Additionally, we can extrapolate a rough estimate for the mean pore size of our gel from this parameter by considering that the pore size scales as $\sim K^{0.5}$, as established by previous analytical relationships[79,80]. From this approximation, we obtain a value of approximately 200 μm which is within the range of values we would expect for this fibrin-based gel[74]. Notably,

prior knowledge of the hydraulic permeability allows us to determine the required pressure differential to model either physiological or pathological flow conditions accordingly to the biological phenomena studied with our platform.

2.2 Growth of Lymphatic Microvasculature under Biochemical Stimulus

During development, lymphatic formation is highly orchestrated by the activation of angiogenic signaling pathways initiated by locally delivered growth factors[81]. As such, an extensive amount of work has identified various growth factors at different stages of lymphatic vascularization[81]. One of the most documented growth factors corresponding to this vascularization phenomena is vascular endothelial growth factor-c (VEGF-C) binding to the lymphatic vascular endothelial growth factor receptor-3 (VEGFR-3)[82]. In fact, locally delivered VEGF-C from implanted biomaterial scaffolds have been consider as a therapeutic strategy to treat the lack of functional lymphatic vasculature leading to lymphedema[83]. Alternately, signaling pathways can mediate lymphangiogenesis in a VEGFR-3-signaling independent manner[84], an example of this includes the activation of the lymphatic hepatocyte growth factor receptor (HGF-R) via the binding of hepatocyte growth factor (HGF) which has been shown to promote lymphatic proliferation, migration and tube formation[85]. Furthermore, growth factors can uniquely activate angiogenic signals in lymphatic endothelial cells, while serving as antagonistic signals for the blood endothelium[86]. Such growth factors include angiopoietin-1 (ANG-1) which promotes lymphangiogenesis in a VEGFR-3-dependent manner, while potentiating TEK tyrosine kinase (TIE-2) activation which drives blood vessel quiescence[87,88].

Motivated by such *in vivo* studies that have elucidated the signaling mechanisms of lymphatic vascularization, we exogenously introduced these growth factors under controlled concentrations to stimulate lymphatic sprouting in our microfluidic cell culture system. It should be noted that, in addition to the growth factors mentioned above, a multitude of cytokines are responsible for the generation of the lymphatic system during embryonic development. However, we focused our efforts on these growth factors given their promising initial, screening results for inducing lymphangiogenesis in our *in vitro* platform[89].

To grow lymphatic capillaries in our microfluidic system, following the formation of a confluent lymphatic monolayer (Day 0), ~350 µL of cell culture medium supplemented with the specified growth factor was added to the adjacent media channel, and replenished on a daily basis for up to 6 days. In a previous set of screening experiments, we identified the minimum concentration required for each growth factor to elicit a lymphangiogenic response, which came out to be around the same concertation of 100 ng/mL for all of them. Growth of the lymphatic vasculature was measured every second day over a course of 6 days by taking epifluorescence images of their RFP signal (**Figure 10**) on a Nikon Eclipse Ti-S (Nikon Instruments, USA) at 4x with a numerical aperture of 0.13. These parameters permit an imaging thickness of ~25 µm, which is of similar thickness as histological sections used to quantify *in vivo* lymphatic morphology[90]. The Lymphatic Vessel Analysis Protocol-plugin in ImageJ (NIH) was utilized to measure morphological properties under the same protocol as implemented for lymphatic capillaries from tissue cryosections[91]. Sprouting length was measured relative to the normal direction starting from the gel-media interface of the device, while the area of coverage was quantified from binarized images that showed the relative area within the gel invaded by the lymphatics. Vessel diameter was measured at the mid-point region of each sprout with 2-3 measurements per sprout (as the sprouts became longer, additional measurements were taken), for a total of 5-20 sprouts per imaged area (depending on the number of available sprouts to measure accordingly to experimental condition and day). All reported measurements, hereinafter, were taken from an average of at least three separate devices and with error bars correspond to standard error of mean.

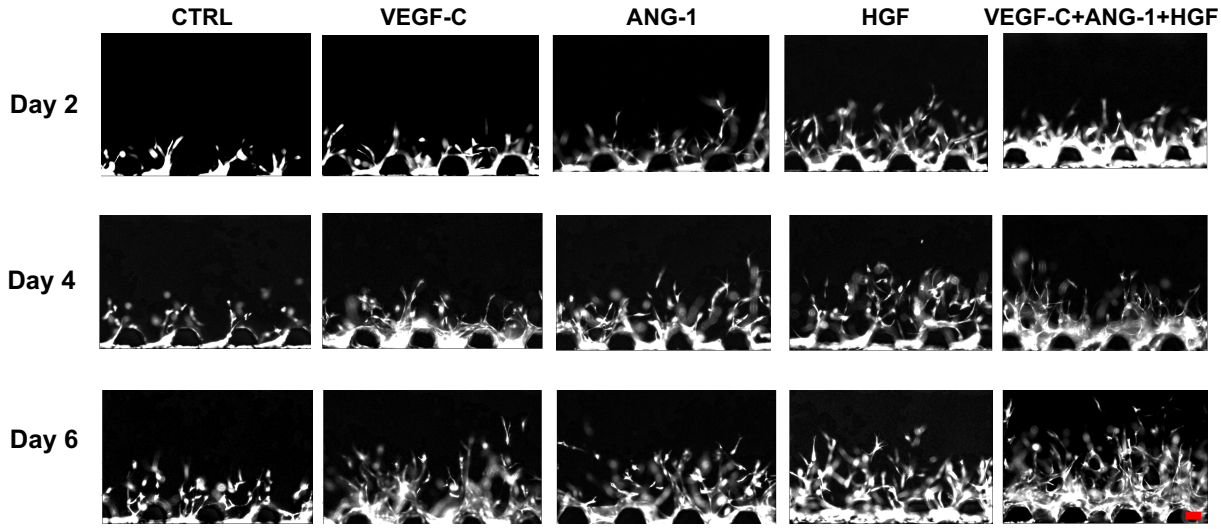

Figure 10: Representative images of lymphatic sprouting for different experimental conditions under biochemical stimulus at different days. Scale bar is 100 µm.

By systematically screening each one of these growth factors in our microfluidic system, with a pre-established lymphatic monolayer at the opposite media channel, allowed for the preferential growth of lymphatic sprout through the gel matrix towards the source channel. Correspondingly, quantitative measurement of this phenomenon revealed that each growth cytokine induces the consistent sprouting of lymphatic vessels, with the most pronounced effects corresponding to HGF-stimulation and the simultaneous stimuli of all three growth factors combined (**Figure 11a**).

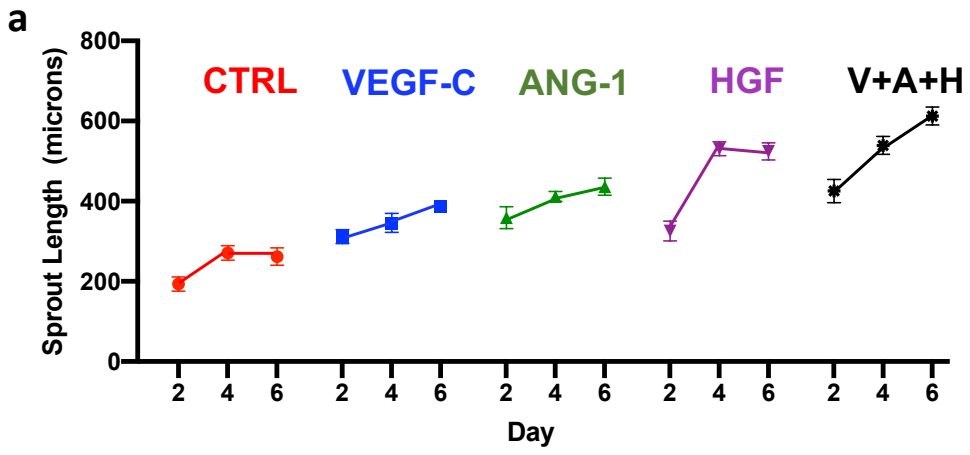

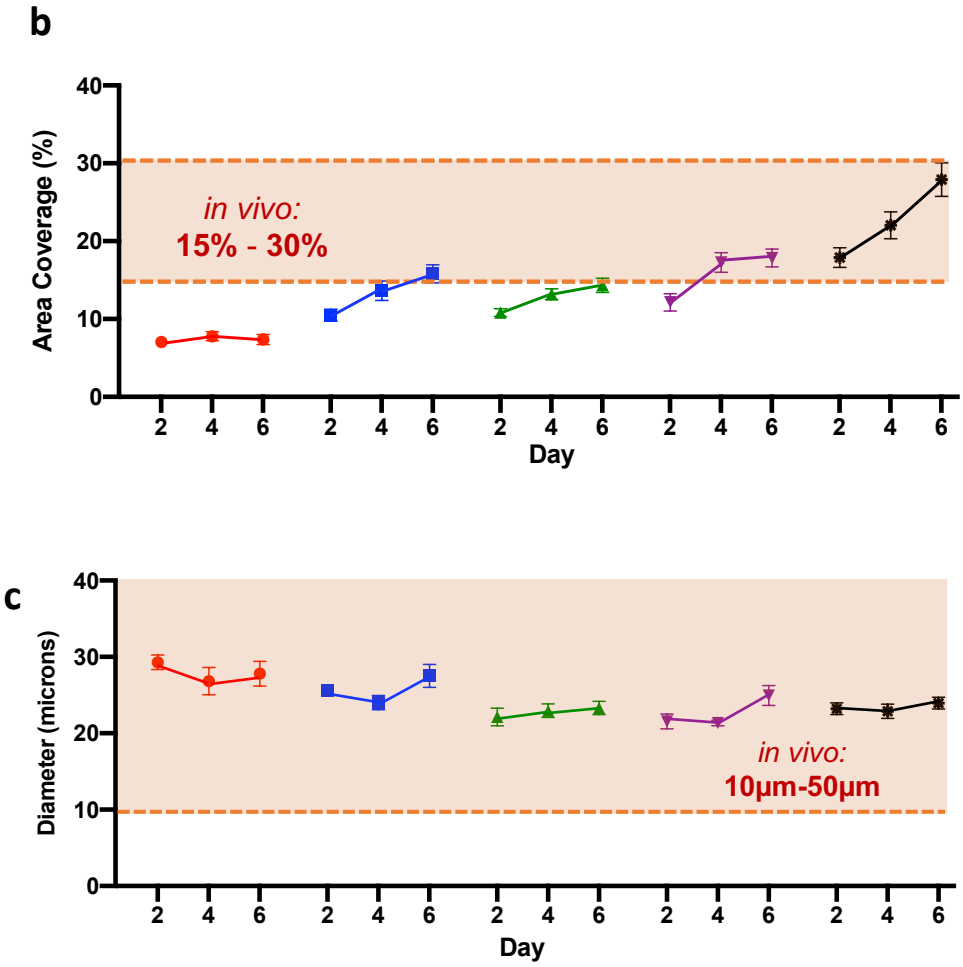

Figure 11: Quantitative analysis of lymphatic microvasculature morphology under biochemical stimulus: (a) sprouting length, (b) lymphatic area of coverage and (c) lymphatic vessel diameter. Highlighted regions correspond to *in vivo* values.

Additional quantitative analysis of the vascular morphology was undertaken to evaluate the lymphatic vascular density, taken as a percentage of the area coverage relative to the gel region. This is the same metric implemented in the morphological analysis of cryogenic sections to evaluate the development of *in vivo* lymphatics[92]. As such, we can bound our analysis to a window that corresponds to the area of coverage measured *in vivo* (15 – 30 %)[93–97]. As we compare the area coverage corresponding to the different factors (**Figure 11b**), we can quickly observe that most experimental conditions fail to overlap with *in vivo* values of lymphatic area coverage. However, by simultaneously stimulating the lymphatics with all the growth cytokines we were able to recapitulate the full range of *in vivo*, lymphatic area coverage within 6 days of culture. This result underscores the necessity of introducing multiple growth molecules to physiologically-emulate the formation of the lymphatic vasculature, as it occurs during development. Additionally, the

diameters of the lymphatic sprouts were measured accordingly to the experimental condition and days in culture (**Figure 11c**). Similarly, to our comparisons to *in vivo*, we bounded an area within our measurements that would correspond to the diameter of lymphatic capillaries. Remarkably, every experimental condition studied achieved diameter values that remained within the bounds of *in vivo* values[12]. These findings highlight one of the many advantages of relying on the self-organization of endothelial cells to form vascular structures, given that this technique achieves a significantly smaller scale in diameters, when compared to most artificial patterning methods. However, a limitation we still face was to achieve a broader range of diameters. This could be managed by investigating additional angiogenic or quiescent inputs to modulate the velocity of sprout invasion, which inversely scales with the sprout diameter, as studied by previous colleagues[98]. Under practical and efficient considerations, we limited our experimentation to a six-day time period, and identified culture conditions that allowed us to recapitulate the physiological morphology of lymphatic capillaries within this short time frame. However, additional studies could be done to grow lymphatic capillaries for longer periods under angiogenic stimuli that potentiate their growth under slower rates, compared to the "optimal" conditions identified in the previous experiment. Specially, to compare the long-term (weeks) stability of the resulting lymphatic structures between culture conditions.

2.3 Probing the Effects of Matrix Density during Lymphangiogenesis

In addition to the wide range of soluble factors that act as chemical signals that guide lymphangiogenesis, the physical properties of the surrounding environment play an equally significant role during lymphatic development. Of special interest is the wound healing microenvironment, where lymphangiogenesis is a locally induced to counteract the increased tissue swelling and inflammation[99,100]. Preceding the VEGFR-3-mediated biochemical signals that lead to lymphangiogenesis, fibrin is deposited at the site of the wound to halt any possible bleeding and reconstruct the damaged ECM[101]. During this process, the structural properties of the matrix are significantly altered by the surrounding stromal, which in turn mediates the migration and remodeling by lymphatic endothelial cells[102]. In order to investigate the effects of fibrin matrix with distinctive physical properties, we varied the concentration of fibrinogen in the fibrin matrix

(**Figure 12**) which globally alters its structural and mechanical attributes (i.e., pore size, fiber density, stiffness)[74].

For this set of experiments, two experimental conditions were considered per fibrinogen composition: a control condition with no induction of lymphangiogenic factors and a set of devices stimulated with the combination of growth factors (VEGF-C, ANG-1, HGF) as described in the previous section. Fibrin gels with varying fibrinogen content were prepared with the corresponding concentrations of: 2.5 mg/mL (which is the standard implemented in protocols established by our lab for the generation of microvascular networks), 5 mg/mL (representative of a dense ECM), and 1.25 mg/mL (analogous of a sparse matrix). All of the implemented fibrin concentrations are within the range of fibrinogen content measured in human plasma[103]. Quantitative comparison of the resultant lymphatic morphology revealed a high tendency of vascular invasion with decreasing fibrinogen concentration (**Figure 13a & b**) for both the control and biochemically stimulated conditions. This is consistent with observation in biological scenarios were matrix remodeling and degradation by cancer-associated fibroblast facilitate angiogenesis[102]. However, from a tissue engineering perspective, the lowest concentration of fibrinogen concentration resulted in an exceedingly and undesired amount of lymphatic invasion with up to half of the matrix populated by lymphatic sprouts at day 6. In fact, this high degree of vascularization was also evident for even unstimulated samples (control devices) which further indicates that this corresponding matrix condition facilitates an uncontrolled growth of lymphatics in our system.

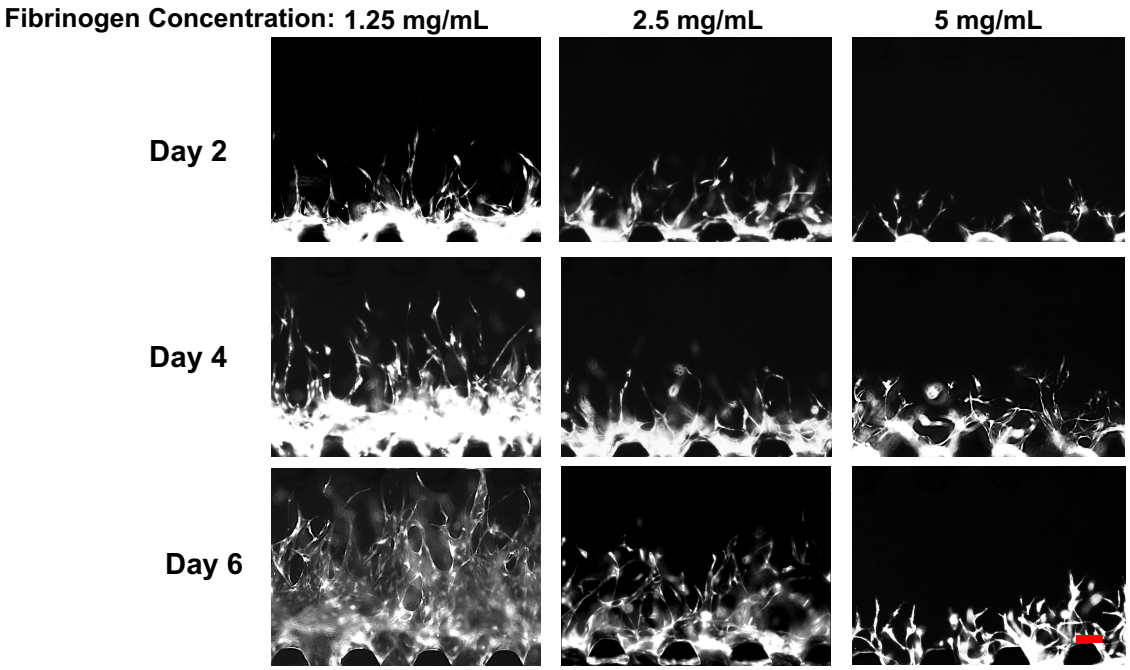

Figure 12: Representative images of lymphatic sprouting for different experiments corresponding to varying fibrinogen concentration in the fibrin matrix. All samples were simultaneously stimulated with VEGF-C, ANG-1 and HGF at a concentration of 100 ng/mL, each. Scale bar is 100 µm.

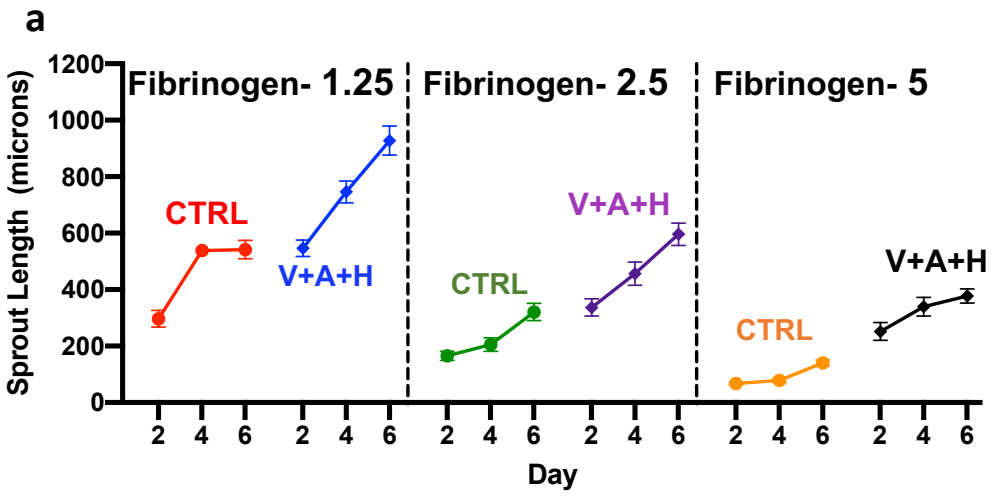

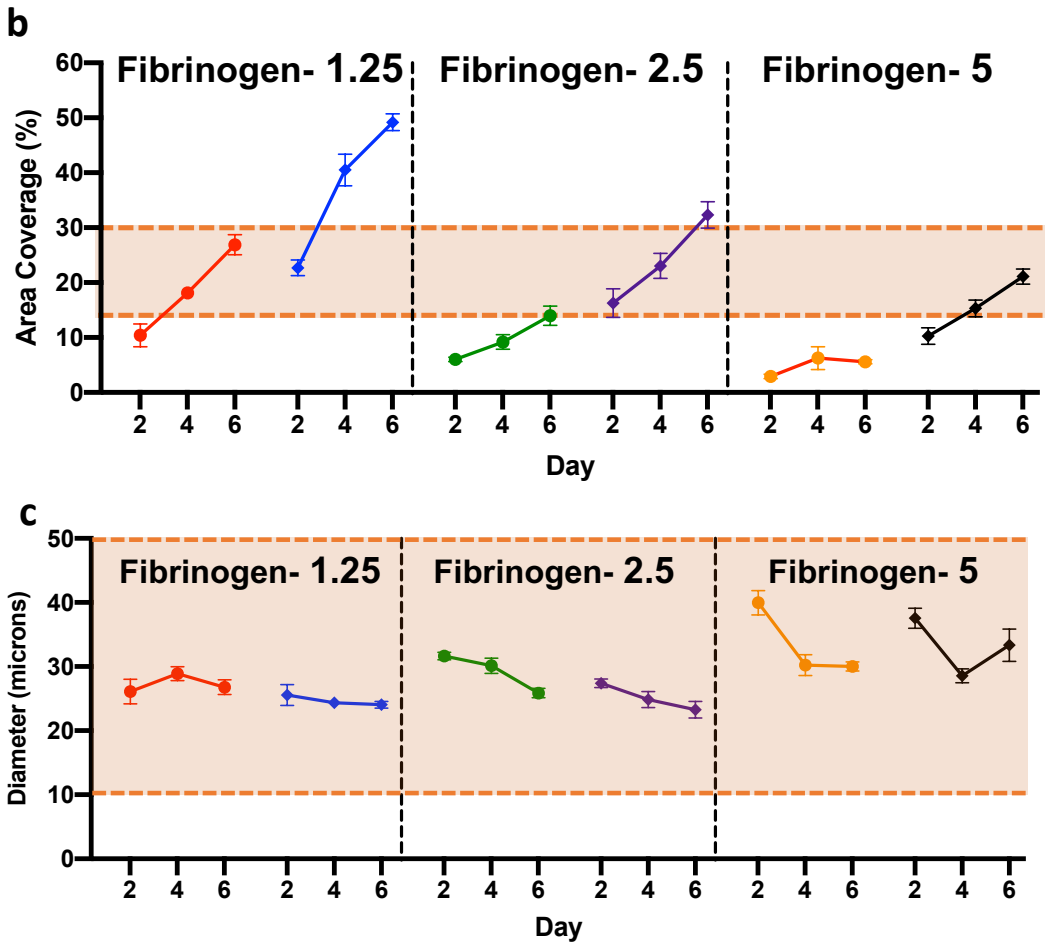

Figure 13: Quantitative analysis of lymphatic microvasculature morphology under varying fibrinogen concentrations: (a) sprouting length, (b) lymphatic area of coverage and (c) lymphatic vessel diameter. Highlighted regions correspond to *in vivo* values.

Consistent with our previous experiments, the biochemical stimulated lymphatics in a 2.5 mg/mL fibrinogen-based matrix achieved the full range of area coverage corresponding to *in vivo* ranges. However, when this fibrin content is doubled, a slower growth rate is imposed on the emerging lymphatic structures. This delayed growth was especially evident when we evaluated the area coverage achieved under this condition, to which we observed that on a partial range of *in vivo* values is achieved within a six-day period. Although continued culture of these samples may still achieve the full range of physiological lymphatic density, to some extent this is unpractical given that it would result in a higher time and cost to grow the lymphatics compared to implementing the lower (2.5 mg/mL) fibrinogen condition. Interestingly, the lower contents of fibrinogen in the

matrix resulted in persistent vessel diameters, while the highest fibrinogen concentration led to larger vessels at the initial days of culture which then regressed to smaller diameters.

2.4 Interstitial Flow-Driven Formation of Lymphatic Vasculature

Fluid flow is an additional pervasive element in the cellular microenvironment that shapes the architecture and function of lymphatic capillaries[1]. In terms of the developmental role of fluid transport during lymphangiogenesis, two distinctive mechanisms have been proposed: (a) by facilitating the transport of stromal cell-secreted VEGF-C to the developing lymphatic sacs[67], from which the initial lymphatic capillaries emerge, (b) for pathological scenarios, such as a tumor microenvironment or inflammation at a wound site, where elevated fluid velocities impart higher fluid-generated forces on cells which activates mechanotransduction pathways resulting in upstream lymphatic sprouting[6]. Given that our microfluidic platform allows for the compartmentalization of an ECM with adjacent fluid channels, a pressure differential across this gel channel would drive interstitial flow through the matrix, thus recapitulating the fluid transport encountered *in vivo* by the lymphatics. We carefully considered different magnitudes of fluid flow velocities (**Figure 14**) corresponding to either physiological interstitial flows (low flow – 0.1 to 1 μm/s)[69], or pathological interstitial fluid velocities (high flow – up to 10 μm/s)[104], which have been shown to elicit distinctive mechanisms of lymphatic vascularization *in vivo*[18,22]. In addition, we studied the synergistic effects of biochemical and fluid flow stimuli, in an effort to gain insight on how the superposition of these factors could be implemented to engineer the lymphatic microvasculature in our system.

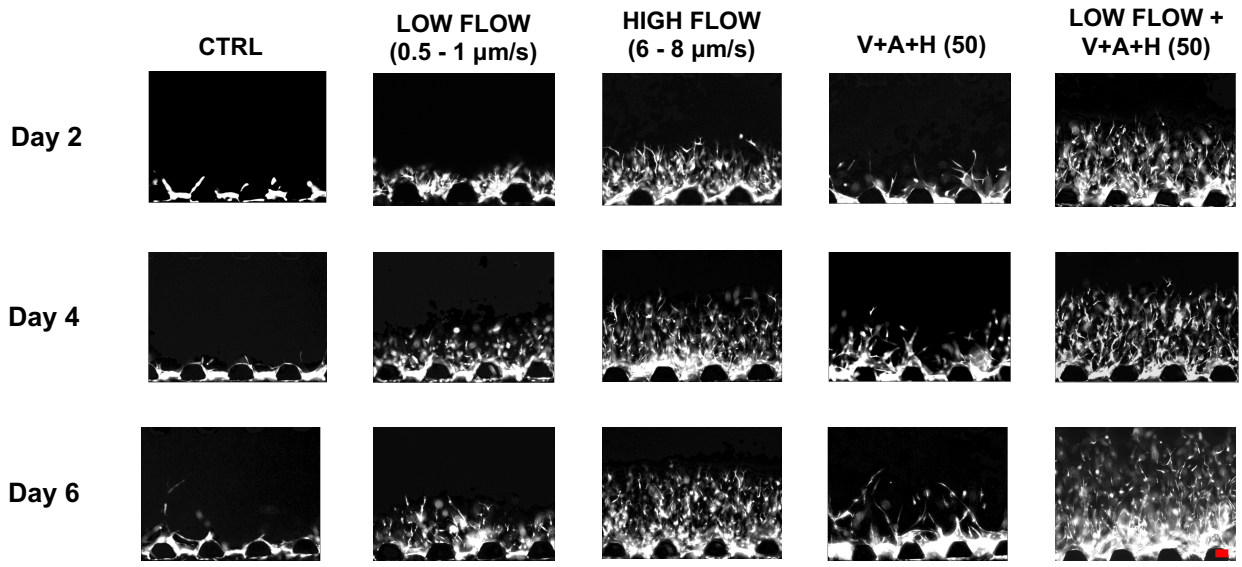

Figure 14: Representative images of lymphatic sprouting for different experimental conditions corresponding to stimulus by interstitial flow at different velocities All samples contained a fibrin matrix with a 2.5 mg/mL content of fibrinogen. Scale bar is 100 µm.

Remarkably, both the low and high interstitial flow velocities elicited lymphatic sprouting during the initial days of culture, however, the extent of vascular invasion was significantly greater for the high flow-stimulated lymphatics (**Figure 15a & b**). At later days, the low flow condition led to the regression of the lymphatic vasculature, while the high flow-stimulated samples appeared to stabilize after day 4. Closer inspection of relevant morphological parameters shows that higher interstitial flow velocities accommodate the desired area of coverage for *in vivo* restitution, while slower flow regimes fall short of this morphological requirement. Thus, biomechanical stimulus imparted by pathological-levels of interstitial flow can be exploited as a means to generate tissue-scale lymphatic vasculature (**Figure 15b**). In fact, this finding is in line with *in vivo* documentation of pathological microenvironments (i.e., a developing tumor or an inflamed wound site) where a buildup of interstitial fluid pressure, from a leaky blood vascular endothelium, leads to higher interstitial fluid flow towards the lymphatics, thus evoking lymphangiogenic activity[18]. In a previous study by our lab[105], vascular angiogenic sprouting was documented to solely occur when the interstitial flow direction was set to induce basal-to-apical transendothelial fluid transport which also corresponds to our experimental setup in this section. Such study also identified the polarized phosphorylation of focal adhesion and Src kinase at the basal surface of the cells under this flow exposure, thus suggesting that the cell adhesion complexes act as key

mechanotransductors to this biomechanical stimulus. As reported by this study, we believe that the lymphatic endothelial cells are eliciting a similar response where fluid pressure stresses, exerted by the interstitial flow, are balanced by tensional forces at the endothelial adhesion sites to the matrix, which would result in the mechanotransduction-driven sprouting against the direction of flow.

In an effort to further study the role of fluid transport in facilitating the transport of pro-lymphangiogenic factors, we also looked into a separate set of experimental conditions where a lower dose of the growth factors, implemented in the prior section, was introduced for both static, no flow and low flow-stimulated samples. As such, we can compare the emergent lymphatic vasculature accordingly to either the biochemical or biomechanical input, or the additive effects of both factors. Given that the implemented concentration of growth factors for this study is lower (50 ng/mL), the resulting lymphatic morphology fell short of recapitulating the *in vivo* area coverage (**Figure 15b**), previously achieved by implementing a higher dose (2x) of these factors. Interestingly, when this lower dose (50 ng/mL) is coupled with low levels of interstitial flow (0.1 to 1 μm/s), exacerbated lymphangiogenic activity is observed with an exceeding amount of lymphatic vasculature invading the gel by day 4 and continuing at later days (**Figure 15a & b**). This resulted in hyper-physiological values for the area coverage by the grown lymphatics. Thus, from this set of experimental conditions, we identified that biomechanically stimulating the lymphatics with pathological levels of interstitial flow provided the optimal approach to generate physiologically relevant lymphatic vasculature. Similarly, to our previous screening experiments, all the diameters remained within range of *in vivo* values, thus further validating this angiogenic-based approach to grow lymphatic capillaries of appropriate length scale.

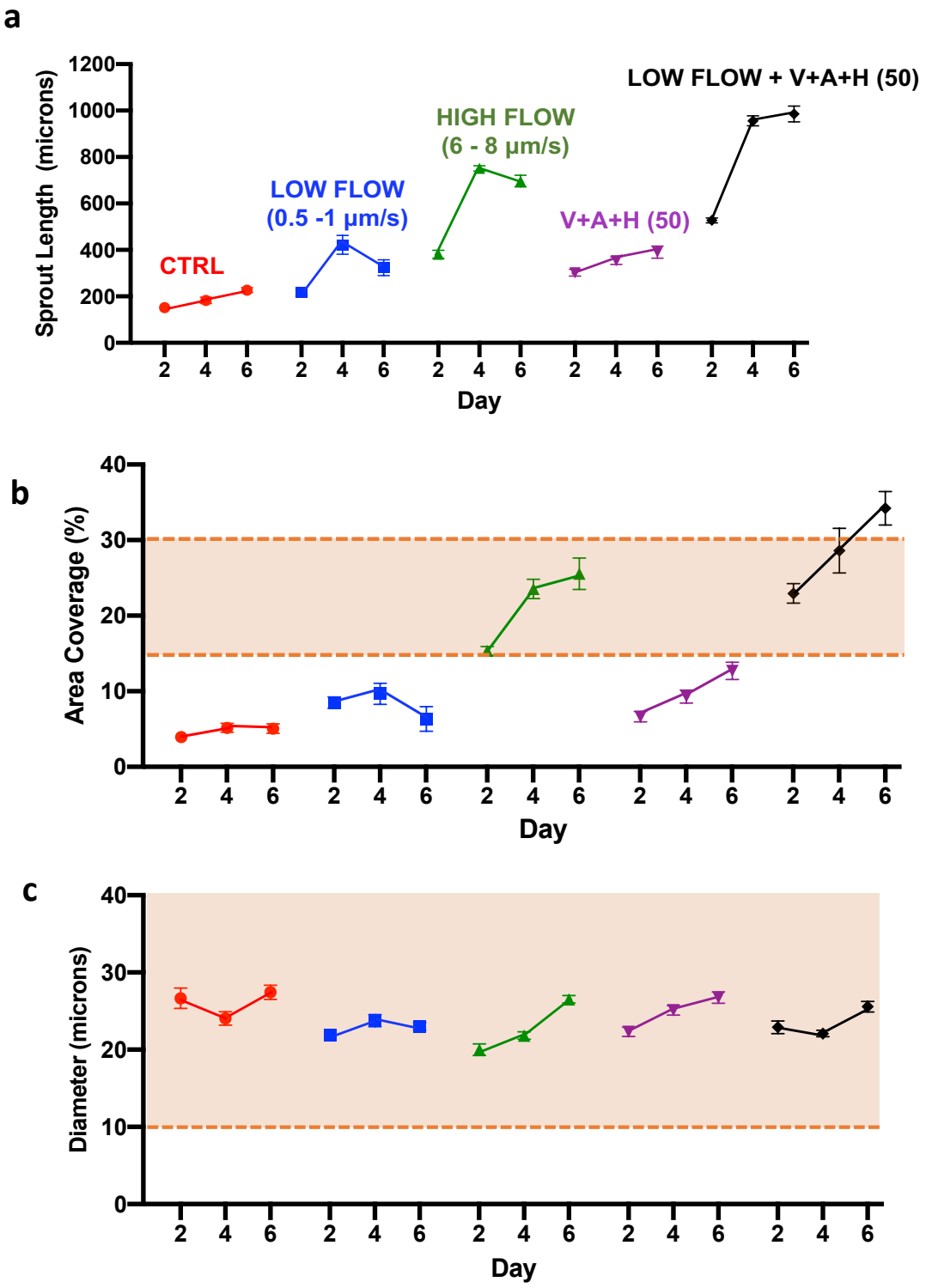

Figure 15: Quantitative analysis of lymphatic microvasculature morphology under varying interstitial flow velocities: (a) sprouting length, (b) lymphatic area of coverage and (c) lymphatic vessel diameter.

2.5 Optimal Lymphangiogenic Parameters for Engineering Lymphatic Capillaries

From the extensive set of experimental conditions studied, we identified two independent approaches to engineer tissue-scale lymphatic vasculature. These approaches rely on either invoking lymphangiogenic signaling pathways, such as VEGFR-3 activation, via growth cytokines (VEGF-C, ANG-1 and HGF at 100 ng/mL) or, alternatively, implementing biomechanical stimulus via high levels of interstitial flow (6 - 8 μm/s) to invoke lymphatic sprouting against the direction of flow. Both methods requiring a fibrin-based matrix with a physiological concentration of 2.5 mg/mL of fibrinogen. From these approaches, we achieved a broad range of lymphatic area coverage (15% - 30%), corresponding to different organ and tissue sites. It should be noted that additional combinations could be exploited to engineer these lymphatic structures with *in vivo* morphological properties, such as further optimizing the combination of growth factors with interstitial flow. However, practical and cost-effective considerations should also be taken, such as minimizing the amount of cell culture media required to induce flow for long periods (days), given that the addition of human recombinant grow factors to the culture media, significantly increases the price of culturing these systems. Thus, more efficient flow setups should be implementing to minimize the amount of media required for long-term flow experiments such as the one developed by our lab, MicroHeart pump[106] (see Appendix A).

To further examine the vascular morphology, immunofluorescence imaging was implemented. Briefly, cells were fixed with 4% paraformaldehyde (Electron Microscopy Sciences) for 15 minutes, followed by permeabilization with 0.01% Triton™ X-100 (Sigma) for 10 minutes. Subsequently, blocking was performed with 5% BSA (Sigma) and 3% goat serum (Sigma) for 1 hour at room temperature. All the reagents were diluted in DPBS. Cells were then incubated overnight at 4°C with a corresponding protein-antibody of interest (diluted in washing buffer at 1:100). Confocal images were acquired with IX81 microscope (Olympus) equipped with Fluoview FV1000 Software. From the acquired confocal images, we were able to observe that in addition to generating small-scale (~20 μm), three-dimensional and lumenized structures that are more representative of their *in vivo* counterpart (**Figure 16 & 15)**. The angiogenic approach undertaken in this study also allows us to generate blind-ended vasculature, a distinctive feature of lymphatic capillaries (**Figure 16**). Furthermore, the engineered vasculature also expressed lymphatic-specific markers such as the lymphatic vascular endothelial receptor-1 (LYVE-1)[107], the upregulated

transcriptional factor PROX-1[108], as well the lymphatic cell surface marker podoplanin[109] (**Figure 18**).

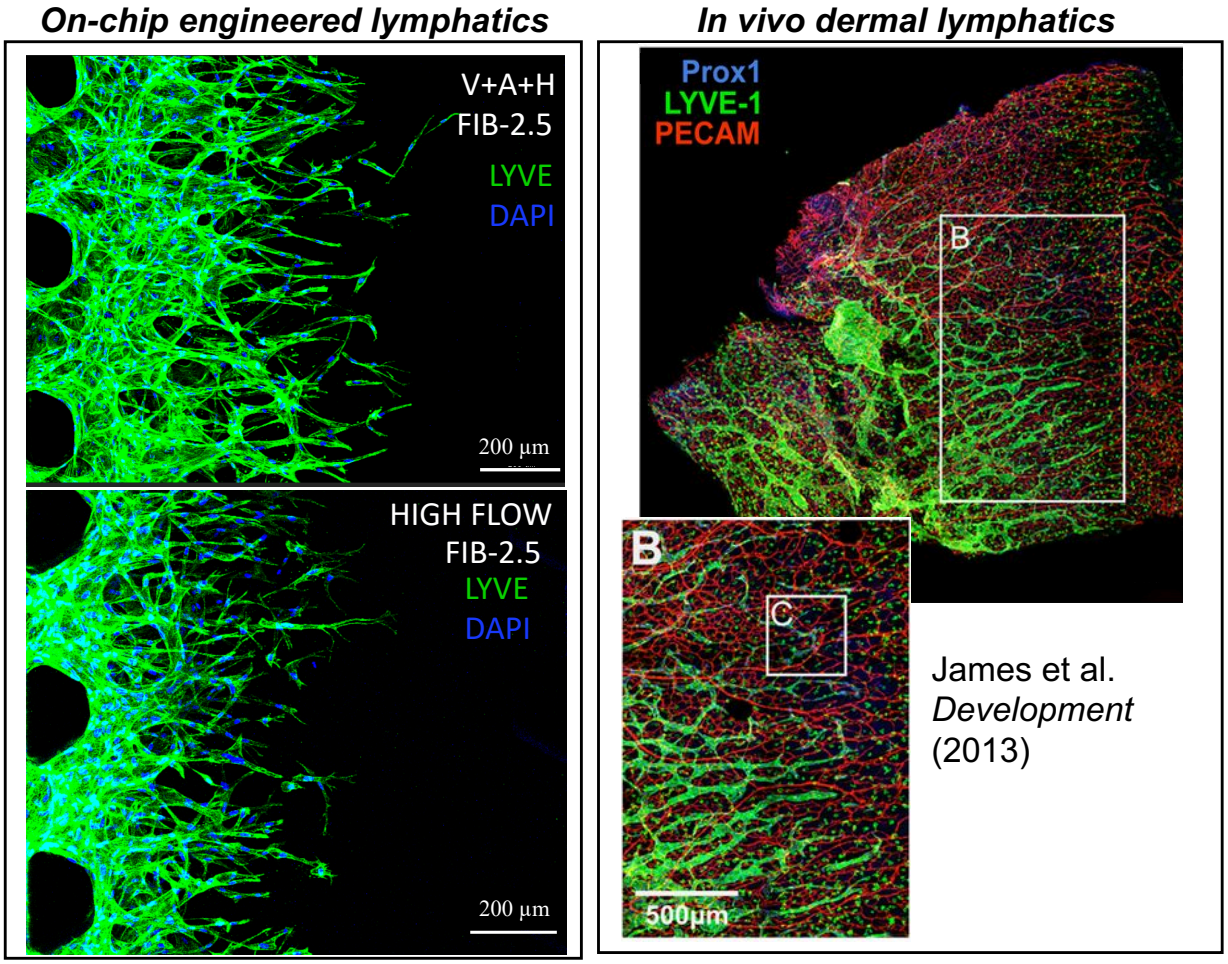

Figure 16: Representative images corresponding to lymphatic vasculature grow in our microfluidic platform (left) and *in vivo* dermal lymphatics[5] (right). Scale bars are specified within the image.

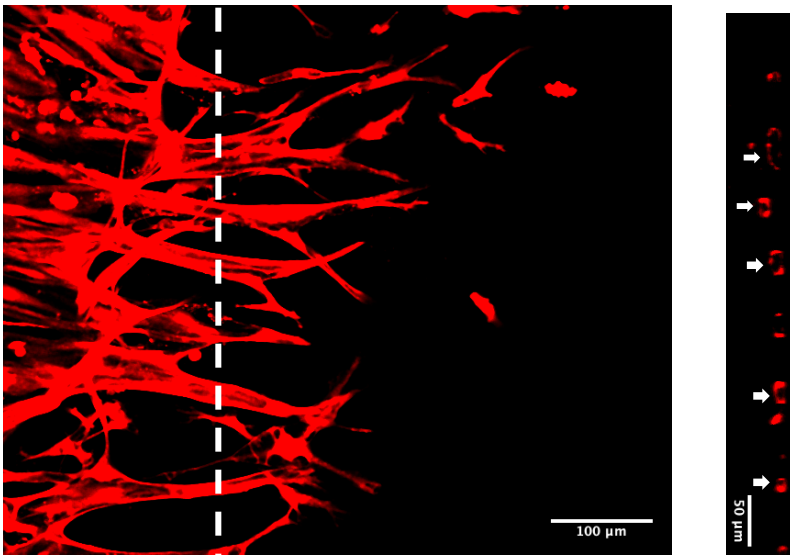

Figure 17: Representative images of the lymphatic vasculature expressing RFP with an orthogonal view of the vessel depicting lumen compartments. White arrows indicate vascular lumens. Scale bars are specified within the image.

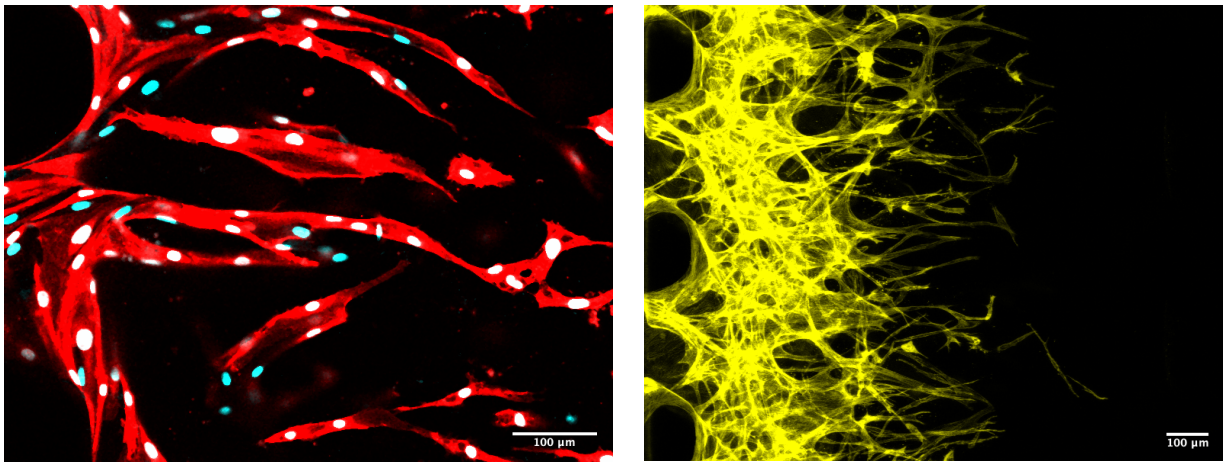

Figure 18: Representative images of engineered lymphatic vasculature expressing RFP and stained for PROX-1 transcriptional factor (cyan) and cell surface staining of podoplanin (left and right images, respectively). Scale bars are specified within the image.

Chapter 3: Functional characterization of physiological solute and protein drainage by engineered lymphatics

3.1 Solute Drainage Rate Assessment of Engineered Lymphatics

The lymphatic system serves an integral role in maintaining tissue homeostasis by clearing excess fluid, macromolecules (plasma proteins), pathogenic agents (such as bacteria and antigens) and small molecules packaged into endogenous carriers (vesicles or exosomes) from the peripheral tissues into the systemic circulation[110]. Typically, the transport of these factors is initiated by their exit from the blood vasculature followed by their transport through the tissue interstitium. This movement, through the interstitial space, is guided mostly by diffusive and convective phenomena that leads the diluted factors towards the lymphatics, due to their lower intraluminal pressure and concentration[111]. As such, research efforts have been guided towards studying the transport of solutes and proteins to the lymphatic circulation with potential applications on: (a) identifying the key biological regulators (intracellular and paracrine signaling) that lead to healthy or dysfunctional lymphatic drainage during lymphedema[112–114] and lymphoma[115], and (b) superior design of therapeutic particles that leverage lymphatic delivery to achieve higher therapeutic exposure and efficacy[116].

In vivo studies quantifying lymphatic drainage have implemented a similar methodology as the clinical imaging technique known as lymphoscintigraphy[116], where the clearance of an injected radiolabeled tracer from the interstitial space is monitored as it is collected by the lymphatics. From such method, lymphatic functionality can be quantified by measuring the clearance of the tracer from the interstitium during a given time interval[117]. The simplicity of this technique has made it amenable for use in animal models to gain insight into the biological mechanisms that lead to the dysfunctional clearance of proteins by the lymphatics (lymphedema)[118]. Furthermore, this functional assay has been implemented in studies with transgenic mice to identify key genetic regulators of lymphatic growth and quiescence[119,120]. However, by utilizing radiolabeled tracers, certain limitations are met due to the radioactive half-life of the tracer, as well as adverse effects due to radioactivity[121]. Alternatively, fluorescence imaging techniques provide a convenient (radiation devoid) and cost-effective approach to monitor the concentration of a particular solute

or protein via conjugation with a fluorophore, this also allows the multiplexed observation of different solutes by implementing fluorophores of varying fluorescence signal[122]. An example of this implemented approach is depicted in **Figure 19**, where the ear flap of a mouse is injected with a fluorescent tracer and the fluorescence signal is monitored over time at the injection site[83]. The decrease in fluorescence signal over time is quantified, by a linear trend in this case, and normalized by the initial fluorescence signal, thus providing a rate (temporal response) of clearance by the lymphatics. Such measurement has been widely implemented for various *in vivo* studies along different dermal sites and with tracers of distinctive molecular weights and electrochemistry, thus providing us with a range of clearance rates (~ 0.025 - 0.005 min^{-1}) from our literature review[83,123–127].

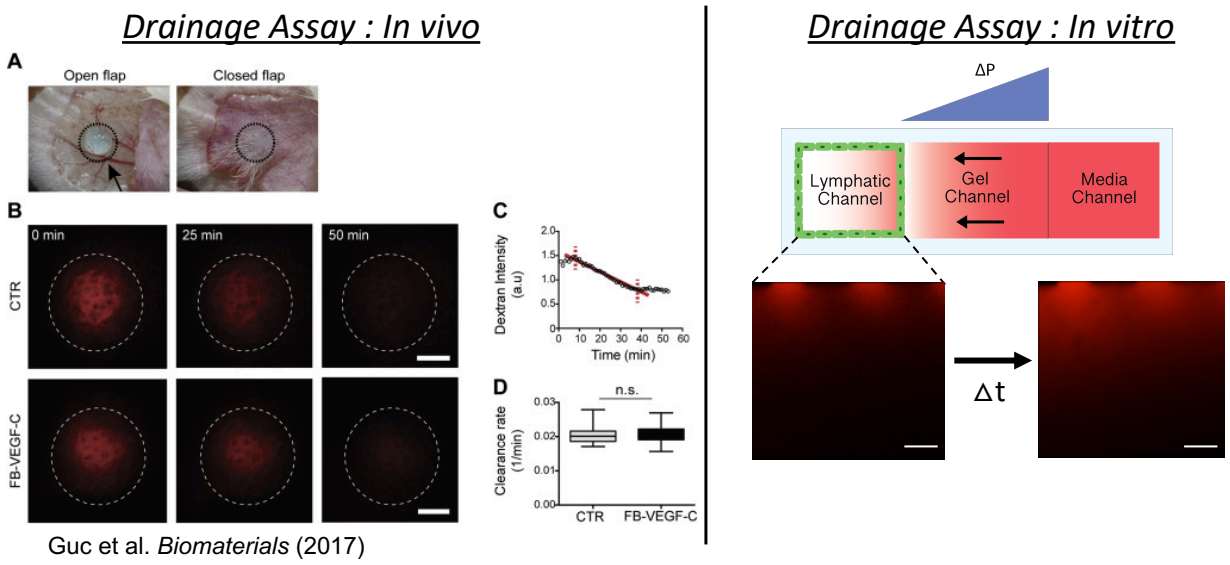

Guc et al. *Biomaterials* (2017)

Figure 19: *In vivo* solute clearance assay with representative images and, fluorescence intensity and clearance rate plots[83] (left image). Schematic *in vitro*-based assay within our microfluidic system to measure the drainage rate via fluorescence signal at the lymphatic media channel (right image).

To measure lymphatic clearance in our *in vitro* engineered lymphatics, we implemented a similar approach previously reported by Tien and colleagues, which is also based on the aforementioned *in vivo* technique to measure lymphatic drainage/clearance rate[49]. Briefly, on day 4 post-seeding/culture of the engineered lymphatics, media supplemented with a specified fluorescent tracer was introduced into one of the media channels to establish a hydraulic pressure difference across the gel region and drive flow across the gel channel at an average interstitial fluid velocity of 0.1μm/s, thus recapitulating physiological flows towards the lymphatics. Immediately after, a

series of 4 ROIs at the opposite media channel (initially solute-free) are imaged as a confocal stack throughout the full height of the device (4 slices at 80 μm) at 10x every 2 - 4 minutes for up to 12 minutes to obtain the increase of fluorescent signal over time. Additional images were acquired for the source channel, where the fluorescently-conjugated solutes are originally introduced. The average fluorescence intensity of each corresponding ROI was extracted using ImageJ-based quantification and used to calculated the solute drainage rate:

$$Solute\ Drainage\ Rate = \frac{\Delta I_v}{\Delta t}\frac{1}{I_s}$$

where ΔI_v indicates the increase in the average fluorescence intensity within the lymphatic vasculature in a given time interval (Δt), and I_s corresponds to the average intensity of the source channel (used to normalized this measurement). A fundamental assumption imposed by this metric is the linear increase in fluorescence intensity as the tracer is drained into the lymphatic channel, which is a rough approximation for the transport of solutes in such system. However, measurements from this assay by Tien and colleagues[49], and our group (**Figure 20**) validate a nearly linear trend in the fluorescence signal corresponding to convection-dominated transport of solutes into the lymphatic channel which we further validate in later sections. A set of four experimental conditions were studied which included three-dimensional engineered lymphatics via optimized protocols implementing either growth factors or high interstitial flow, as described in Chapter 2. In addition, a set of two control conditions were included corresponding to an acellular, gel system, and samples with a lymphatic monolayer cultured under no angiogenic stimuli, thus the lymphatic endothelial cells mostly remained in a two-dimensional setting at the gel-media interface.

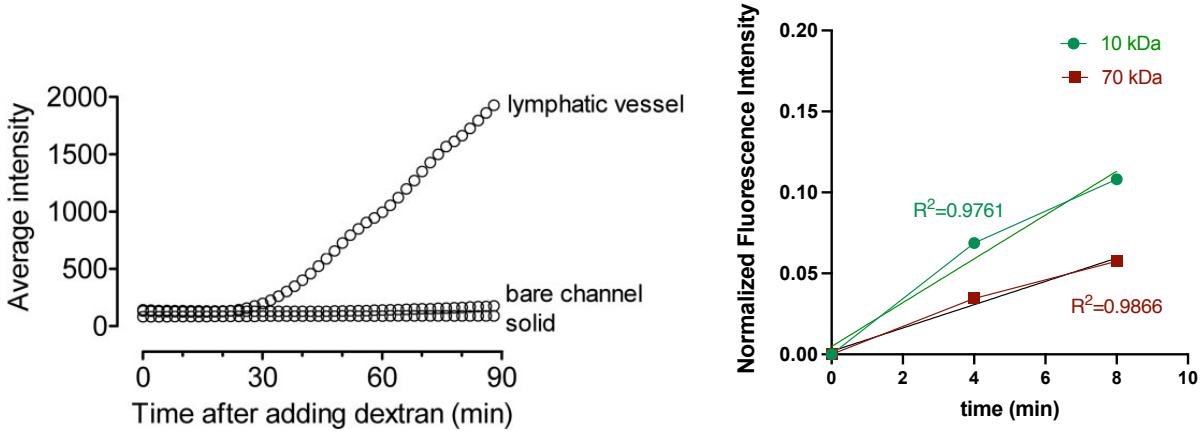

Figure 20: Temporal plot of fluorescence intensity corresponding to solute drainage measurements of 10 kDa dextran by Tien and colleagues[49] (left) and our 3D lymphatics on-chip system (right).

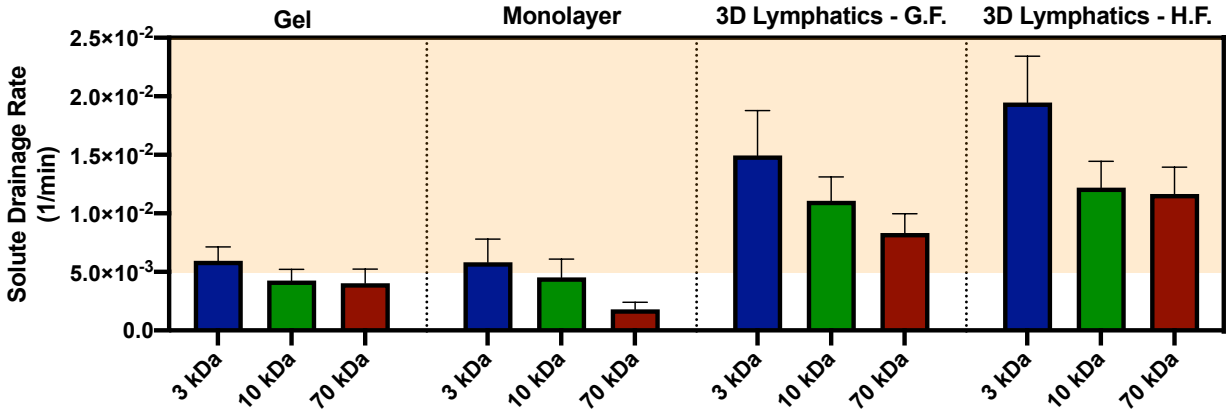

Figure 21: Quantification results of solute drainage rates accordingly to the experimental condition and dextrans of varying molecular weight. Shaded area corresponds to reported *in vivo* values of drainage/clearance rate. From left to right, conditions correspond to: bare gel (devoid of cells), lymphatic monolayer (devoid of angiogenic stimuli), 3D lymphatics grown with growth factors (GF), and 3D lymphatics grown with high-levels of interstitial flow (HF).

From the overall experimental measurements for solute drainage rates (**Figure 21**), a series of interesting trends can be observed between systems and varying molecular weight of the tracer. For the gel system, solute drainage rates, for the range of molecular sizes tested, fell within or below a value of 0.005 min^{-1} which barely recapitulates *in vivo* measured rates of solute drainage. Interestingly, if we take the inverse of the average measured rate (~0.005 min^{-1}) a time of 200 minutes is obtained which represents the timescale for the solutes to be drained through this bare

gel system. This timescale is in agreement with the scaling analysis: 1200 μm / 0.1 μm/s (*w/v*) which is the convective timescale for transport across the gel width. However, given the low fluid velocity in this system, diffusive transport could also play a significant role in the migration of the solutes. To characterize the relative importance between diffusive and convective transport, we can implement the dimensionless parameter known as the Peclet number which accounts for the timescale of each phenomena:

$$Pe_{gel,\parallel} = \frac{u/L}{D/L^2} = \frac{uL}{D}$$

where u indicates the local velocity, L is the characteristic length of the system, and D denotes the diffusion coefficient of the solute. Notably, in the above expression, we consider that the relative modes of mass transfer are competing in the same direction (||), thus their timescale correspond to the same characteristic length. Considering the fluid velocity and length of the system under study, we find that the Peclet ranges from 8 – 26 with lower bound values corresponding to smaller tracer molecules (higher diffusion coefficient) and, conversely, higher Peclet numbers accord to larger molecules. Thus, transport within the gel is dominated by convection which validates the convective timescale agreement with the gel drainage rates.

Interestingly, when we turn our attention to the lymphatic monolayer system, we observe a consistent drop in the measured solute drainage rates as we increase the molecular weight of the tracer (**Figure 21**). This trend is similarly observed in previous experiments by our lab, studying blood microvascular systems, in which both the diffusive and convective transport rates decrease with increasing tracer molecule size as a result of the inherent difficulty of larger molecules to migrate between the small dimensions of the endothelial intercellular space. Hence, the introduction of the lymphatics as a monolayer in our microfluidic system imposes an additional barrier of solute transport which effectively reduces the solute drainage rates to sub-physiological levels.

Evaluation of the solute drainage rates for the three-dimensional lymphatics, engineered by angiogenic induction with either growth factors or pathological levels of interstitial flow, confirms their physiological functionality for solute drainage as we compared the measured values to *in vivo*-based measurements of solute clearance rates (**Figure 21**). Furthermore, as we increase the

molecular weight of the dextran, physiological levels of interstitial solute clearance are still achieved by the engineered lymphatic microvasculature, conversely to the other systems (bare gel and lymphatic monolayer).

We also tested the drainage rates for more biologically relevant proteins, avidin and albumin. The former is extensively implemented for therapeutic particle conjugation due to its highly functional and stable affinity interaction for desired molecular targets[128], while the former is the most ubiquitous plasma protein responsible for maintaining oncotic pressure homeostasis in the blood stream[129]. Additionally, despite being of similar molecular weight (~ 65 kDa), avidin and albumin exhibit significantly different isoelectric points which correspond to their distinctive positive and negative charge, respectively, at a physiological pH. Thus, the selected proteins allow us to probe the influence of distinctive surface charge which is representative of various plasma and interstitial proteins[130].

The experimental measurements further validated that the bare gel or lymphatic monolayer system failed to recapitulate physiological ranges of protein drainage rates (**Figure 22**). In fact, both proteins were cleared at similar rates as the fluorescent dextran of similar molecular weight (70 kDa). However, systems that incorporate three-dimensional lymphatic microvasculature recurrently exhibit protein drainage rates comparable to the *in vivo* measured values (**Figure 22**). Furthermore, avidin (positively-charged)[131] was drained at slightly higher, but not significant, rate than the albumin (negatively-charged)[132] in both systems. This could be the result of charge interactions between the cationic protein and the lymphatic glycocalyx, a negatively-charged cell surface coating of glycoproteins and proteoglycans[133]. While we are able to confirm the expression of this proteoglycan/glycoprotein layer in our engineered lymphatics (**Figure 23**), to date, no *in vivo* studies have addressed the role of the glycocalyx during lymphatic protein drainage. Thus, additional *in vitro* and *in vivo* studies are merited.

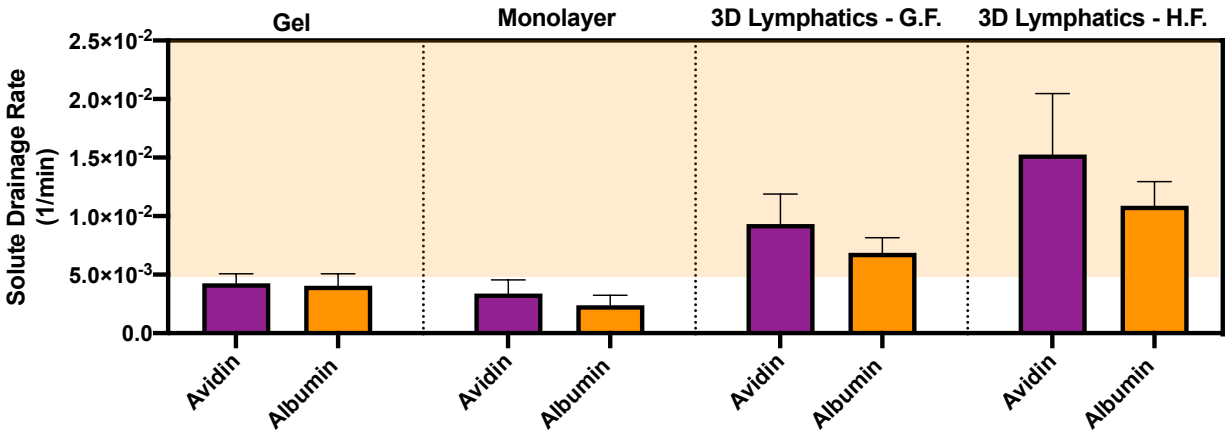

Figure 22: Quantification results of solute drainage rates accordingly to the experimental condition and dextrans of varying biological molecules. Shaded area corresponds to reported *in vivo* values of drainage/clearance rate.

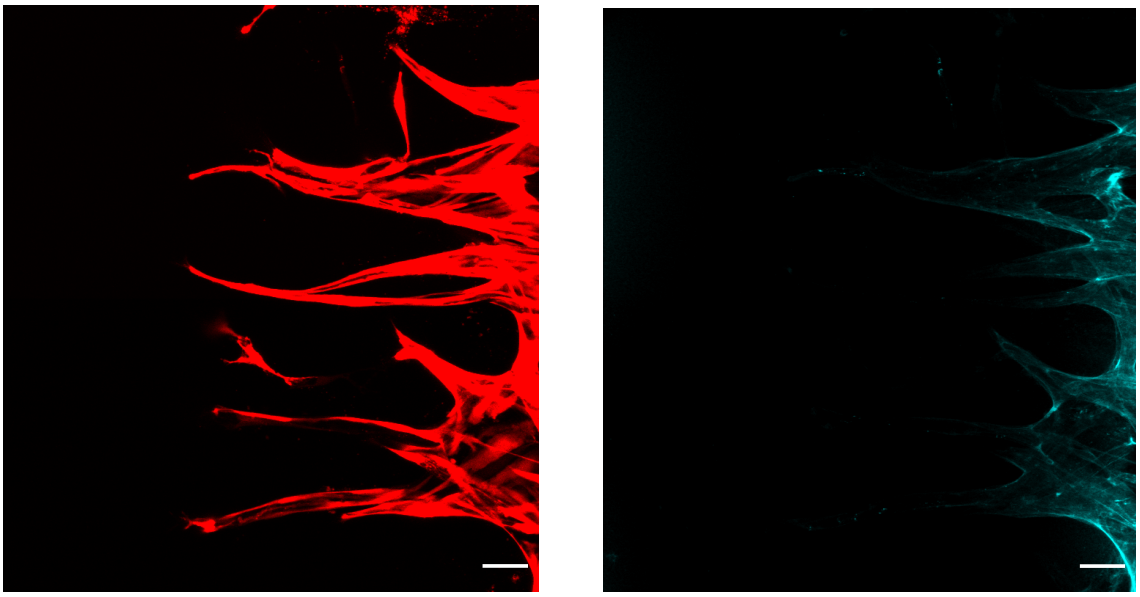

Figure 23: Representative images of the engineered lymphatic microvasculature where lymphatic express RFP (left) are also stained with lectin (right) to stain the glycocalyx. At the same fluorescence imaging settings, glycocalyx staining reveals significantly less expression relative to the RFP signal. All scale bars are 50 µm.

Beyond confirming the physiological drainage functionality of our engineered lymphatics, a fundamental question arises from these results: what is the physical basis by which the three-dimensional engineered lymphatics can exhibit higher drainage rates? By initial inspection, one

could hypothesize that the invading lymphatic microvascular structures, within the gel region, increases their surface area, which in turn increases the total flux of solutes into the lymphatics. Hence, the pronounced difference in geometry between the three-dimensional lymphatics and the monolayer system determines their distinctive drainage rate. However, this could lead to a second question: is the presence of the lymphatic endothelium contributing to this physiological transport phenomenon or is the three-dimensional structure the only determinant for higher drainage rates? This last question bears significance for tissue engineering applications given recent efforts to incorporate artificial lymphatics in engineered tissue constructs by simply casting empty microchannels.

In an effort to examine the relative drainage contribution of the lymphatics across different systems implemented in this work, an additional solute drainage rate assessment was conducted after decellularizing the system. This was done by washing away the cells with a detergent solution of 1% Triton™ X-100 in DPBS for 10 minutes immediately after the first solute drainage measurement, followed by washing the previous fluorescent tracer using DPBS for 5 minutes. All the washing steps were done under a slight pressure head difference (4 mm). Solute drainage rate measurements were repeated with decellularized devices to determine the relative difference between measured values prior and post lymphatic decellularization.

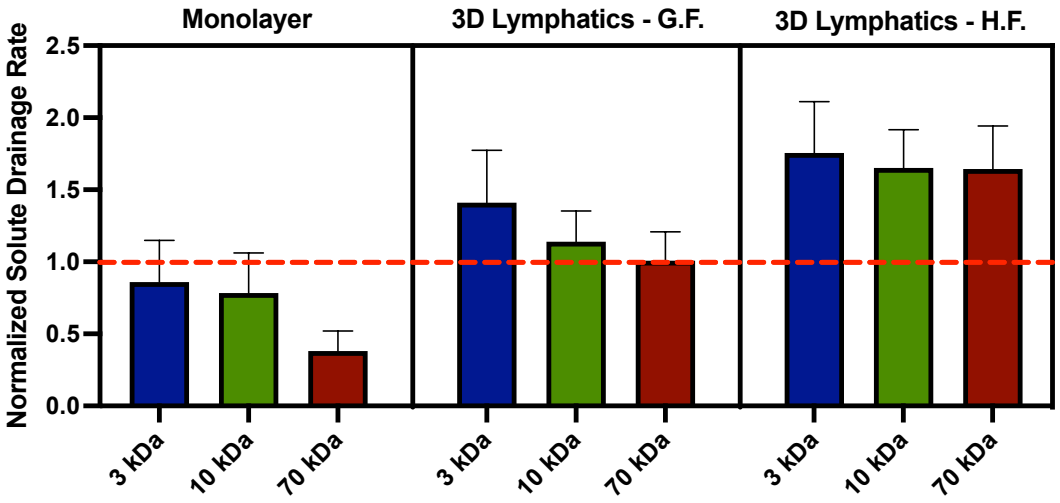

Figure 24: Normalized solute drainage rates (relative to the respective decellularized sample) for dextrans of varying molecular weight accordingly to the experimental condition that the lymphatics were implemented in the microfluidic system.

From this assessment, we were able to take into account differences in the geometry between systems to experimentally measure if the lymphatic endothelium dampens or enhances the clearance of solutes in the corresponding system (monolayer or engineered vasculatures). Experimental measurements determined that for the monolayer system, the addition of the lymphatics proceeded to slower drainage as represented by values falling below unity in the normalized drainage rate (**Figure 24**). Conversely, for both microvascular systems, we start to observe values greater than unity which translates to increased drainage due to the presence of the lymphatic endothelium within the three-dimensional vascular structures. Thus, lymphatics contribute to the physiological drainage functionality in the engineered microvascular platforms, beyond just providing an increased vascular surface and additional microchannels. However, these findings are yet to elucidate the physical basis leading to the enhanced transport of solutes by our engineered lymphatic microvascular system. This will be the subject of the following section.

3.2 Computational Modelling of Lymphatic Solute Drainage

Given that our previous assessment is limited to providing a bulk measurement of the drainage of interstitial solutes into the lymphatics, we sought to find an alternate approach to obtain higher spatiotemporal characterization of the underlying transport phenomena. As such, we implemented the COMSOL Multiphysics software to facilitate the *in silico* study of solute drainage in our tissue engineered systems. A two-dimensional geometry was developed based on a cross-sectional view of a lymphatic sprout within the gel region. The ascribed geometry of the sprout was based on the morphological characterization conducted in previous chapters, while the gel domain extended to the full width of the center channel and the height was based on the approximated distance between sprouts (~65 μm). An additional domain (0.5 μm thick) was implemented between the sprout and gel region that represented the lymphatic endothelium. To this domain, the Kedem-Katchalsky equation was imposed which characterizes the flux of solutes across a semipermeable membrane[134]:

$$N = P_e \, \Delta C + (\Delta p_{EC} \, L_p) \cdot C \, (1 - \sigma_f)$$

where the diffusive flux is driven by the concentration difference times the diffusive permeability, and the convective flux is given by the scalar product between the fluid velocity (obtained from the Starling equation) and the local concentration. The convective term also incorporates a filtration reflection coefficient (σ_f) which considers the fraction of solutes that permeate across the endothelium along with the fluid flux[135]. Fluid mechanics throughout the system was governed by the Brinkmann equation within the gel region and Stokes flow in nonporous regions. The transport of solutes throughout the rest of the system was governed by Fick's Second Law incorporating both diffusive and convective transport phenomena. The pressure and concentration boundary conditions were set to the same magnitudes as implemented in the experimental drainage assay with a constant value set at the inlet and a convective outflow boundary set at the outlet (**Figure 25**). Transient numerical solutions were generated for a total computational time of 1000 seconds, similarly as the experimental assay (~15 minutes). The intrinsic transport properties of the lymphatic endothelium, including the diffusive permeability and hydraulic conductivity, were determined experimentally as described below.

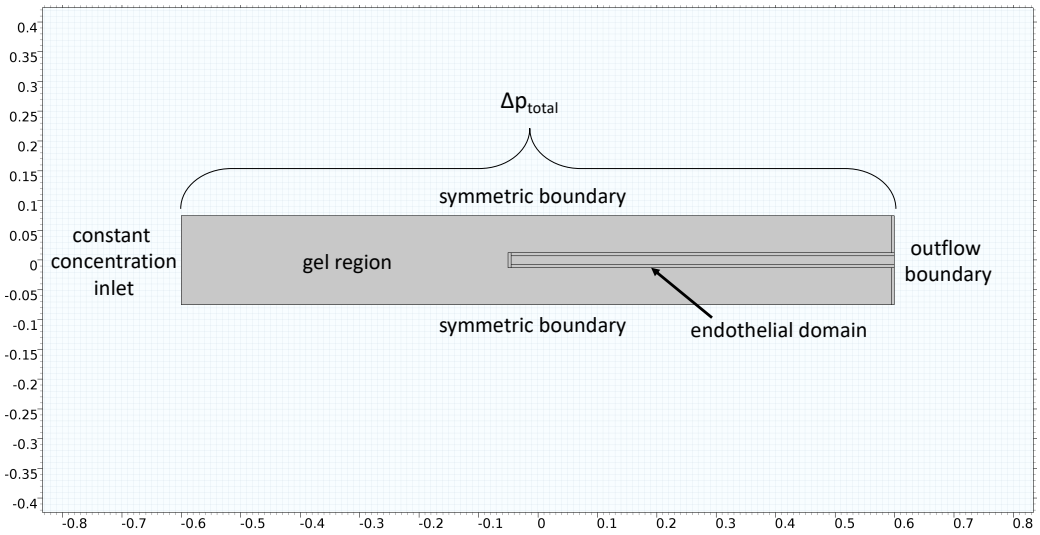

Figure 25: Geometry and boundary conditions of the computational model for lymphatic solute drainage developed in COMSOL Multiphysics.

To quantify the diffusive transport across the lymphatic endothelium, a diffusive permeability assay was implemented based on previous protocols. Briefly, devices were perfused with a fluorescent tracer at the lymphatic media channel, and allowed to diffusive through the

endothelium while confocal z-stacks of at least 100 µm deep were collected in steps of 5 µm and at time intervals of 2 minutes. Considering the principle of mass conservation, the diffusive flux (N_d) of the solutes from the lymphatic endothelium into the gel region can be quantified by taking the temporal derivative of the total concentration (C) in the gel control volume (V_g):

$$N_d = \frac{\partial}{\partial t} \int_{V_g} C \, dV = A_s \, P_e \, \Delta C.$$

This mass conservation analysis can be expressed as a membrane diffusive transport equation where the total diffusive flux is driven by the concentration difference (ΔC) times the surface area of the vasculature (A_s), and the diffusive permeability of the endothelium (P_e)[133]. Following these quantitative arguments, and the assumption that the fluorescence intensity is linearly proportional to the concentration of the fluorescent tracer, imaging analysis[133] can be implemented to obtain the diffusive permeability as:

$$P_e = \frac{\Delta I_g}{\Delta t} \frac{1}{I_{v,i} - I_{g,i}} \frac{V_g}{A_s}$$

where ΔI_g corresponds to the increase of average fluorescence intensity in the gel region after a given time interval (Δt), respectively, and $I_{v,i}$ and $I_{g,i}$ indicate the initial, average fluorescence intensity within the lymphatic vasculature and gel volume, respectively. This measurement was repeated at 3 different locations per device for different fluorescent tracers of varying molecular weight, given the dependency of diffusive transport on the hydrodynamic-Stokes radius (size) of the tracer[136].

Fluid transport across the lymphatics was described on the basis of the endothelial hydraulic conductivity which was measured following a similar assay as previously described for interstitial flow measurements using FRAP. For this assessment, interstitial flow velocities (v) in devices with lymphatics were measured accordingly to the same pressure head differences (Δp_{total}) performed for the estimation of the hydraulic permeability. Following these measurements, we implemented a hydrodynamic circuit analogy were the major sources of hydraulic resistance (ratio of differential pressure and volumetric flow rate) in the system originate from the gel and lymphatic endothelium.

Considering that these hydraulic resistances act in series[105], the differential pressure across the endothelium (Δp_{ec}) can be estimated by:

$$\Delta p_{ec} = \Delta p_{total} - \frac{w\,\mu\,v}{K}$$

where the differential pressure across the gel is governed by Darcy's law, as previously described. Knowing the pressure drop across the endothelium, we can apply the Starling equation[137] to establish the proportionality between the pressure difference and fluid flux across the lymphatics, known as the hydraulic conductivity (L_p):

$$L_p = \frac{v}{\Delta p_{ec}}$$

where the oncotic pressure contribution is neglected given homogenous distribution of solutes throughout the system. This quantification was performed for every distinctive condition that the lymphatic endothelial cells were introduced and cultured in the microfluidic system (monolayer, growth factors- and interstitial flow-grown lymphatics).

Additional parameters such as the diffusion coefficient (D) and reflection coefficient (σ_f) for the different fluorescent-solutes were based on previous studies from our lab. Given the high degree of similarity for the diffusion coefficient value corresponding to 70kDa-dextran from our analysis to previous studies in our lab, we approximated the diffusion coefficients of the other fluorescent-dextrans from these studies[58,138,139]. Additionally, from this previous study[77], a range of values for the reflection coefficient were considered in which the highest bound value ascribed to the lymphatic endothelium corresponded to that measured in blood microvascular networks given that the junctions of the lymphatics are exceedingly leakier. The collection of all the parameter values implemented for the simulations are summarized in Table 1.

Table 1: Experimental and computational default parameters for lymphatic drainage model.

Parameter	Symbol	Value
Source concentration of 3 kDa dextran	$c_{o,\ 3kDa}$	3.3 x 10^{-2} mol/m^3
Source concentration of 10 kDa dextran	$c_{o,\ 10kDa}$	1.0 x 10^{-3} mol/m^3
Source concentration of 70 kDa dextran	$c_{o,\ 70kDa}$	1.4 x 10^{-3} mol/m^3
Diffusion coefficient of 3kDa dextran	D_{3kDa}	14.5 x 10^{-11} m^2/s
Diffusion coefficient of 10 kDa dextran	D_{10kDa}	9 x 10^{-11} m^2/s
Diffusion coefficient of 70 kDa dextran	D_{70kDa}	4.5 x 10^{-11} m^2/s
Hydraulic conductivity of monolayer lymphatics	$L_{p\ M}$	3.9 x 10^{-6} m/Pa s
3 kDa dextran permeability in monolayer lymphatics	$P_{M,\ 3kDa}$	7.0 x 10^{-8} m/s
10 kDa dextran permeability in monolayer lymphatics	$P_{M,\ 10kDa}$	1.3 x 10^{-8} m/s
70 kDa dextran permeability in monolayer lymphatics	$P_{M,\ 70kDa}$	1.2 x 10^{-8} m/s
Hydraulic conductivity of growth factor-grown lymphatics	$L_{p\ GF}$	3.6 x 10^{-6} m/Pa s
3 kDa dextran permeability in growth factor-grown lymphatics	$P_{GF,\ 3kDa}$	2.3 x 10^{-8} m/s
10 kDa dextran permeability in growth factor-grown lymphatics	$P_{GF,\ 10kDa}$	4.3 x 10^{-9} m/s
70 kDa dextran permeability in growth factor-grown lymphatics	$P_{GF,\ 70kDa}$	3.8 x 10^{-9} m/s
Hydraulic conductivity of high flow-grown lymphatics	$L_{p\ HF}$	8.1 x 10^{-6} m/Pa s
3 kDa dextran permeability in high flow-grown lymphatics	$P_{HF,\ 3kDa}$	7.2 x 10^{-8} m/s
10 kDa dextran permeability in high flow-grown lymphatics	$P_{HF,\ 10kDa}$	3.0 x 10^{-8} m/s
70 kDa dextran permeability in high flow-grown lymphatics	$P_{HF,\ 70kDa}$	2.4 x 10^{-8} m/s
Reflection coefficient of 3 kDa dextran	$\sigma_{f,\ 3kDa}$	0.2-0.4
Reflection coefficient of 10 kDa dextran	$\sigma_{f,\ 10kDa}$	0.4-0.8
Reflection coefficient of 70 kDa dextran	$\sigma_{f,\ 70kDa}$	0.4-0.8

Numerical results depict the uniform movement of solutes across the gel region as it approaches the lymphatic sprout. Once the solutes are located at the front end of the sprout, the pressure difference across the endothelium drives the entrance of solutes into the lumen compartment. It is at this region that the transport of solutes is accelerated, compared to the solutes that continue traveling within the gel region (**Figure 26**). This local increase in transport rate can be attributed to a lower hydraulic resistance exhibited by the lumen compartment (R_{lumen}), as compared to the resistance imposed by the gel region (R_{gel}) which can be validated on the basis of scaling:

$$\frac{R_{gel}}{R_{lumen}} \sim \frac{\mu\, L/_{K\, r^2}}{\mu\, L/_{r^4}} \sim \frac{r^2}{K}$$

where the same geometric parameters, length (L) and radius (r), are attributed to each region for direct comparison, and with the dynamic viscosity (μ) and hydraulic permeability (K) also contributing to this estimation. Upon taking the ratio of resistances, we find that the scaling analysis reduces to a comparison in length scale where the hydraulic permeability is on the order of 10^{-14}, and the squared length of the radius is approximately 10^{-10} which results in a difference of 4 orders of magnitude. Thus, the lumen compartment provides a path of significantly less resistance where the solutes are preferentially transported, along with the fluid flow direction. Additionally, we can continue this analysis to verify the resistance contributed by lymphatic endothelium as:

$$\frac{R_{endothelium}}{R_{lumen}} \sim \frac{1/_{L_p\, r\, L}}{\mu\, L/_{r^4}} \sim \frac{r^3}{L_p\, \mu\, L^2}$$

where the hydraulic conductivity (L_p) and the surface area of the sprout provide an estimate to the resistance to fluid passage through the endothelium. For different parameters corresponding to either the growth factor- or high flow-grown lymphatics, this ratio results in a value of either 0.7 or 0.3, respectively, which suggests that the endothelium does not act as a substantial barrier to fluid transport. Since the resistance by the lymphatic endothelium is comparable to that of the

lumen, then both are negligible compared to the resistance imposed by the gel region. To further validate this, we also compared the hydraulic resistance between the gel and endothelium as:

$$\frac{R_{gel}}{R_{endothelium}} \sim \frac{{}^{\mu\, L}/_{K\, r^2}}{{}^{1}/_{L_p\, r\, L}} \sim \frac{L_p\, \mu\, L^2}{K\, r}$$

from which we obtain a difference of at least 3 orders of magnitude, thus affirming that both resistances contributed by the lymphatic sprout (endothelial and luminal) are exceedingly lower than transport across the gel. Overall, these scaling arguments reveal that lymphatic sprouts facilitate solute drainage by providing a faster pathway for solute convection with minimal hindrance to fluid transport. This aligns with our previous experimental observations that 3D lymphatics achieve higher solute drainage rates, compared to a monolayer system.

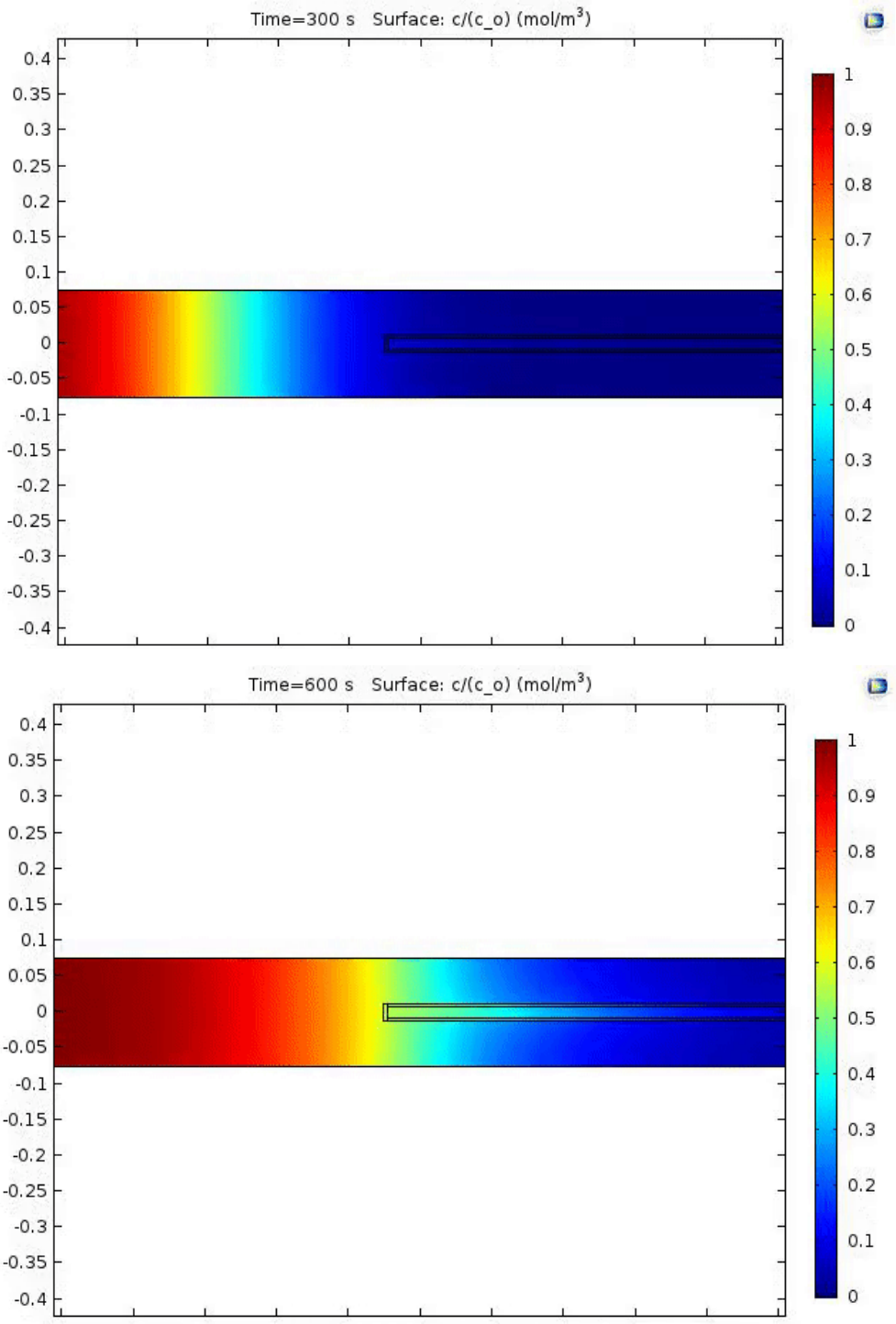

Figure 26: Computational model results for lymphatic solute drainage developed in COMSOL Multiphysics depicting the normalized concentration of solutes representing 10 kDa dextran at different stages during drainage: the first (upper) image showing the approaching solutes to the sprout at 300 seconds and the second (lower) image showing the spatial distribution of solutes at 600 seconds.

To further investigate distinctive mechanisms in the transport of solutes through the lymphatic sprout, we also implemented a model that captured the solute drainage in decellularized samples, similar to the previous experimental condition, to provide a comparative basis. As such, most of the parameters for the decellularized model remained the same, as with the lymphatic sprout model, with the simple modification that the domain corresponding to the endothelial wall was removed. Thus, generating an empty lumen compartment from its previous structure, as it would similarly occur after we perform decellularization in our samples. Since fluid transport across the endothelium was mostly unhindered, the convective flux of the diluted species into the lumen yielded similar distribution and rates between models (**Figure 27**), except in cases were a high reflection coefficient was implemented in the simulations for the lymphatic sprout model. However, an interesting phenomenon was observed in both model systems, where the local accelerated movement of solutes within the lumen compartment creates pronounced concentration gradients in the radial/lateral direction. This concentration difference drives the diffusive flux of solutes from the lumen compartment back into the interstitial space, regardless if the lumen contained an endothelial barrier or not (decellularized). Evidently, solutes that "leaked" out would then travel at a slower rate across the system until they were brought back into the lumen compartment by either convection or diffusion. To quantitatively evaluate this "leakage" flux, post-processing was implemented to depict a series of arrows that described the directionality and magnitude of the diffusive flux along the lumen (**Figure 27**). Such results suggest that for a greater magnitude of solutes that diffused out of the lumen, a slower drainage rate follows. The magnitude of diffusive flux also varied accordingly to the diffusion and permeability coefficient of the solute, correspondingly to their distinctive hydrodynamic radius. As such, with decreasing molecular weight, a greater amount of solutes would diffuse out from the decellularized lumen, in comparison to the drainage of the same molecule by the lymphatic sprout system (**Figure 27**). Overall, differences in drainage rates between models are a direct consequence of competing transport modes (diffusion versus convection) and their relative magnitude accordingly to each situation. We continue our analysis towards identifying the interplay between different transport parameters that determine these distinctive rates of solute drainage across each system.

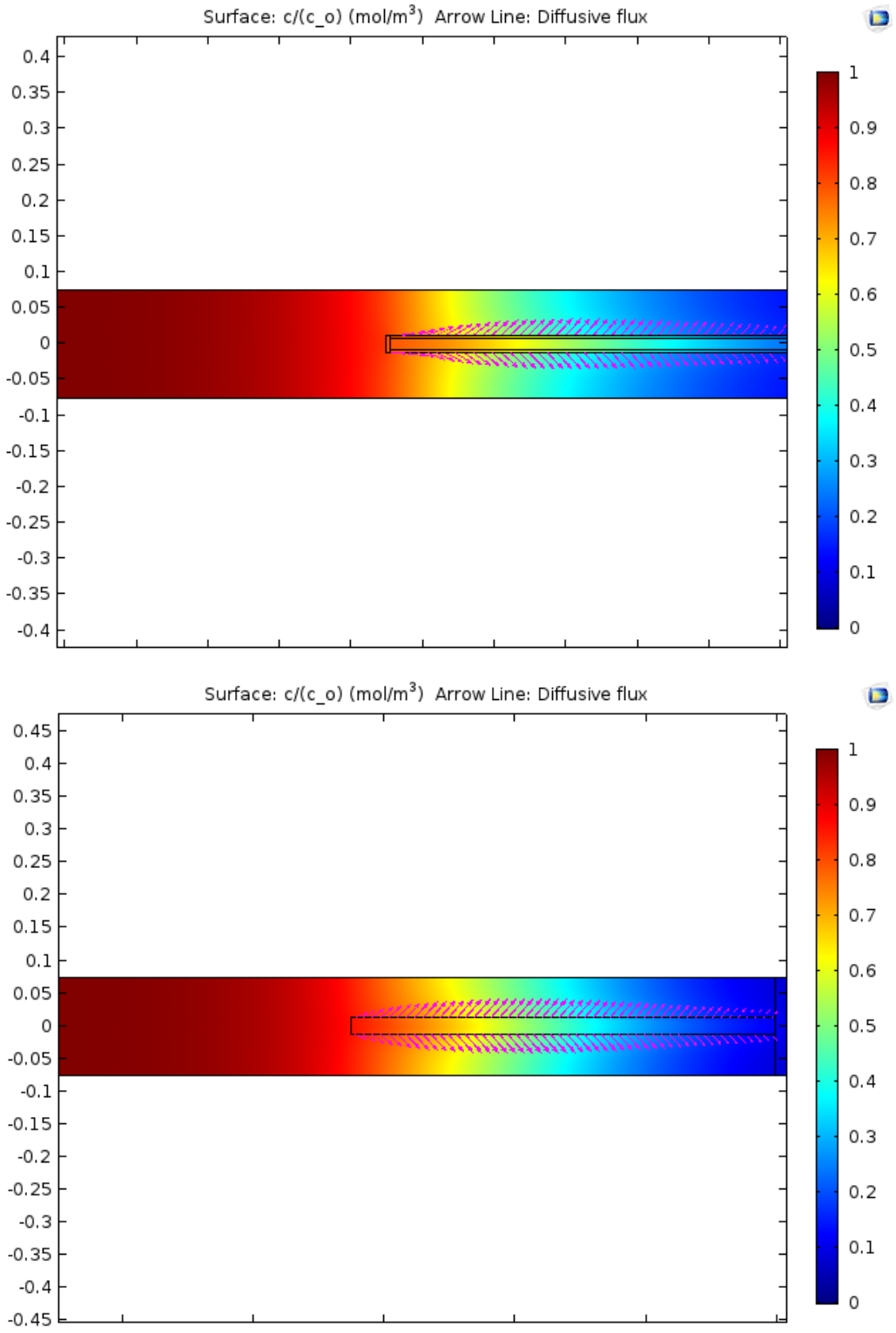

Figure 27: Computational model results for lymphatic sprout solute drainage (upper image) and decellularized-sprout solute drainage (lower image). Both models depict the normalized concentration of solutes representing 10 kDa at 800 seconds and the magenta-color arrows indicate the magnitude and directionality of the diffusive flux at the lumen surface.

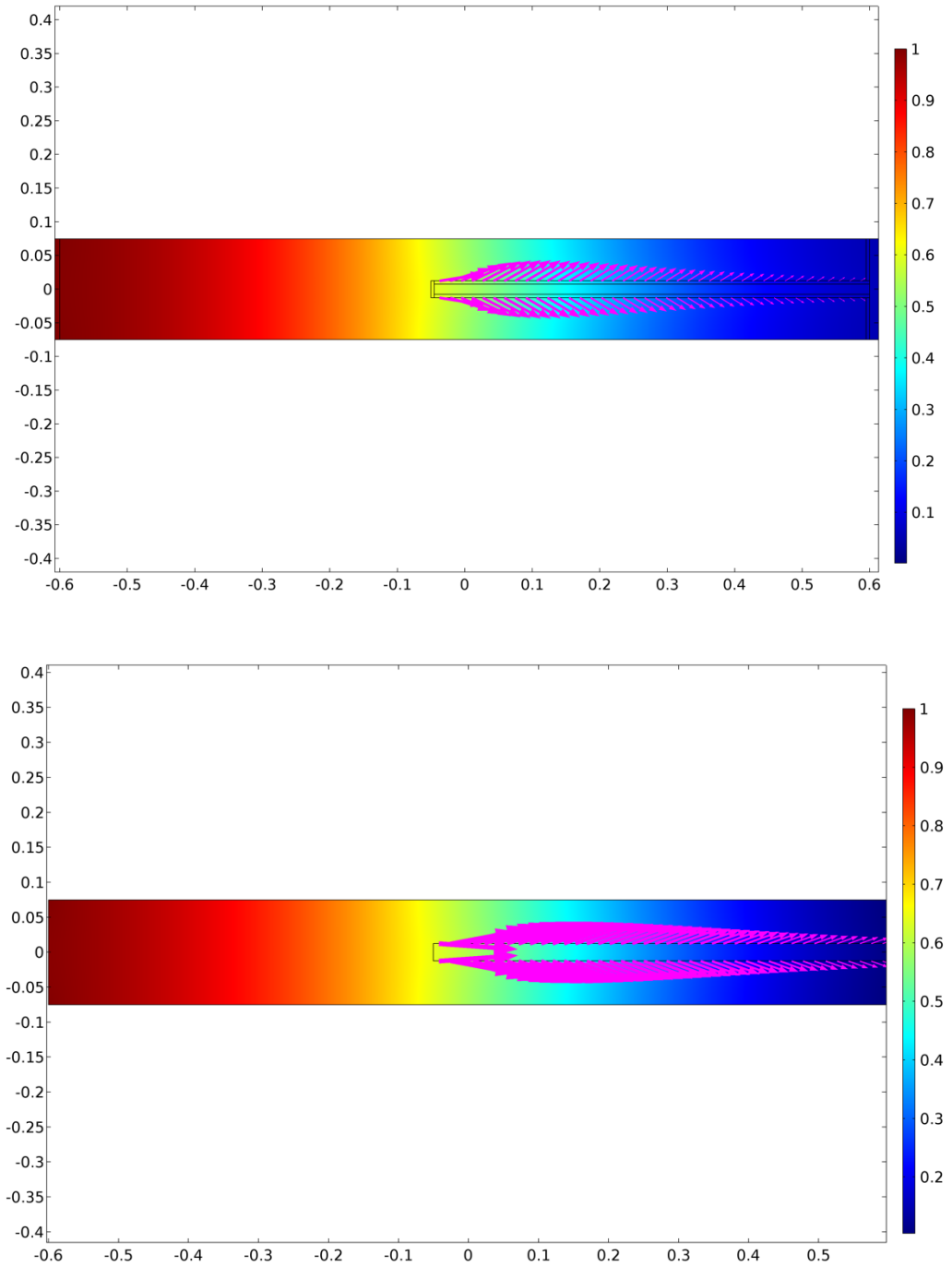

Figure 28: Computational model results for lymphatic sprout solute drainage (upper image) and decellularized-sprout solute drainage (lower image). Both models depict the normalized concentration of solutes representing 3 kDa at 500 seconds and the magenta-color arrows indicate the magnitude and directionality of the diffusive flux at the lumen surface.

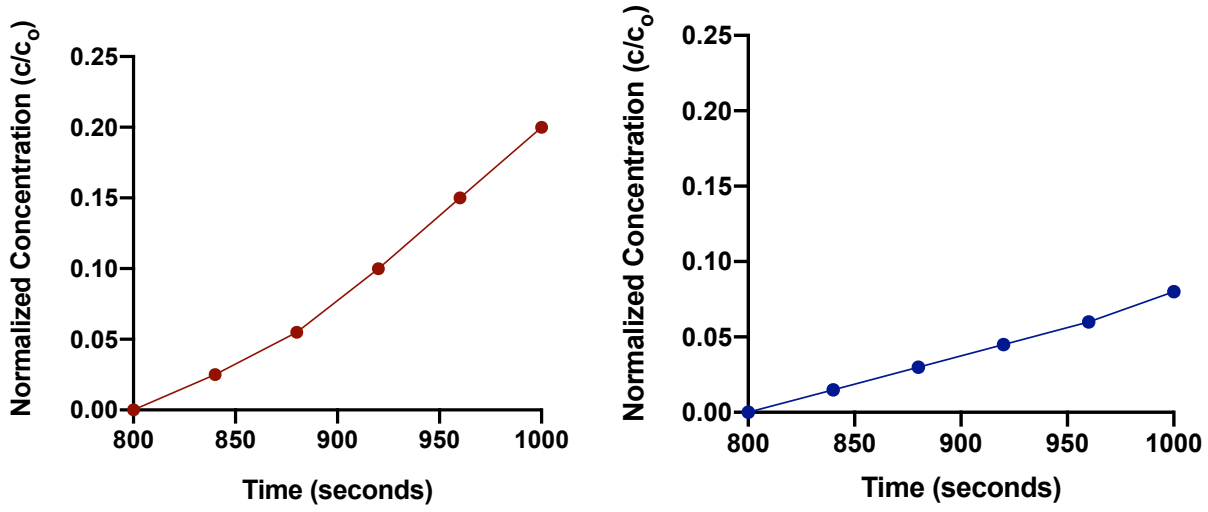

Figure 29: Concentration plot corresponding to a concentration probe placed at the end of the lumen compartment, thus measuring the increase in solute concentration during drainage by the lymphatic sprout model (left) and the decellularized-sprout system (right). Both plots pertain to 10 kDa dextran-based solute properties.

To further verify these computational results, we extracted an additional set of data from the simulations in which a concentration probe was added at the end of the lumen channel to measure the increase in concentration during drainage. Subsequently, we quantified the corresponding drainage rate based on the concentration measurements from the last 200 seconds of the model. Since the implemented models only capture the transport of a single lymphatic sprout, direct measurements cannot be taken with our tissue-scale, experimental measurements for drainage rates. However, the ratio of drainage rates between the lymphatic sprout and the decellularize system can be applied, and taken as comparative basis to the normalized measurement that we also implemented in our experimental drainage assay. Remarkably, we found a high degree of agreement between our experimental measurements and computational results, across the different systems and for solutes/tracers of varying molecular weight (**Figure 30**), hence supporting our theoretical framework to describe the underlying transport phenomena and parameters that give rise to the distinctive drainage rates accordingly to the implemented system.

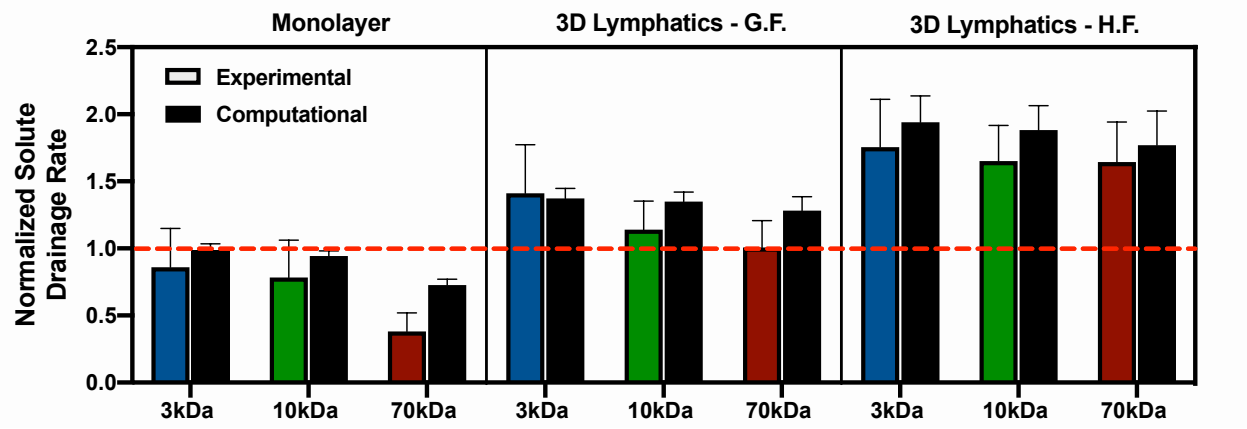

Figure 30: Normalized solute drainage rates for dextrans of varying molecular weight for the different experimental conditions and showing both computational and experimental results for the implemented lymphatic system.

Finally, to have a simplified framework for understanding the underlying differences in transport phenomena, we further implemented scaling analysis with an emphasis on the relative timescales of solute transport within the lumen region. For this, we evaluated the Peclet number with appropriate adjustments to the scaling arguments accordingly to the studied system. For the lymphatic sprout model, the scaling parameters for the Peclet number follow as:

$$Pe_{lymph,\parallel} = \frac{(1-\sigma_f)u/L}{D/L^2} = \frac{(1-\sigma_f)u\,L}{D}$$

where u indicates the average luminal velocity of the fluid, L corresponds to the sprout length, D continues to indicate the diffusion coefficient of the molecule and the reflection coefficient (σ_f) corrects for hindrance effects on the solutes. As we noted earlier, the timescale approximations in this analysis considers the relative competition of each phenomenon in the same, parallel direction. On a similar basis, the Peclet number for the decellularized sprout would be described as:

$$Pe_{decell,\parallel} = \frac{u/L}{D/L^2} = \frac{u\,L}{D}$$

which simplifies to the traditional Peclet number expression. For both of these parameters, the range of values come out to be from 15 to 47 for the lymphatic sprout model, and from 24 to 77 for the decellularized system. Thus, the convective flux of solutes dominates their luminal transport, for both systems, which is in line with our previous analysis that this fluid pathway provides a faster route for solute drainage. However, diffusion of solutes simultaneously occurs at the lateral/radial direction which is responsible for the solute leakage from the lumen into the gel region observed in our computational results. As such, the Peclet number for this analysis would consider the diffusive transport timescale in the radial direction as:

$$Pe_{decell,\perp} = \frac{u/L}{D/r^2} = \frac{u\,r^2}{D\,L}$$

for the decellularized system. Similarly, modifying the scaling arguments for the diffusive rate in the lymphatic sprout yields:

$$Pe_{lymph,\perp} = \frac{(1-\sigma_f)\,u/L}{P/r} = \frac{(1-\sigma_f)\,u\,r}{P\,L}$$

where P is the diffusive permeability of the endothelium. Taking this new parameterization for the relative transport rate, we calculated that the Peclet numbers are in the range of 0.02 to 0.06, for the decellularized system, and 1.2 to 7, for the lymphatic sprout model, which implies that the diffusive rate by which these solutes are leaking out of the lumen has a significant contribution in the overall drainage in both model systems. However, the presence of the lymphatic endothelium dampens the relative magnitude of this diffusive leakage, as demonstrated in the simulation results and scaling analysis. Thus, enhancing the solute drainage rates compared to bare, empty channels which is also consistent with the normalized drainage measurements presented in the previous experimental section.

3.3 Steady State Vascular Transport and Protein Concentration Analysis

From our previous experimental and analytical techniques, we were able to validate the physiological drainage functionality of our tissue engineered lymphatic microvascular system. It should be noted that this analysis was limited to the transient phenomenon of solute and protein clearance from the interstitial space, which is representative of physiological scenarios where medication or therapeutic biologics are subcutaneously injected into the interstitium to be then drained by the lymphatics[116] (further studied in Chapter 5). However, lymphatic drainage is ubiquitous and its primary function is to maintain hydraulic and osmotic pressure homeostasis across different tissues on a steady state basis[2]. Thus, our analysis for this engineered vascular system would be complemented by evaluating the vascular transport of proteins under both dynamic conditions and and chemical equilibrium. For this, we are faced with experimental limitations given that the contribution by the blood vasculature should be accounted in the engineered system to accurately recapitulate the physiological and steady transport across vasculatures. Current efforts in our lab are underway to integrate our previously developed blood microvascular system and the lymphatic vascular model, described in this work, within the same on-chip environment (discussed in Chapter 6). Such system would allow us to comprehensively model the steady flux of proteins that exits from the blood vasculature into the interstitial matrix, and drained by our lymphatic vascular model. Although this novel platform is currently under development, our prior and extensive characterization of the transport phenomena in both vascular models allows us to develop the framework to predict the experimental parameters that would allow us to physiologically recapitulate the steady transport of proteins across both vascular systems.

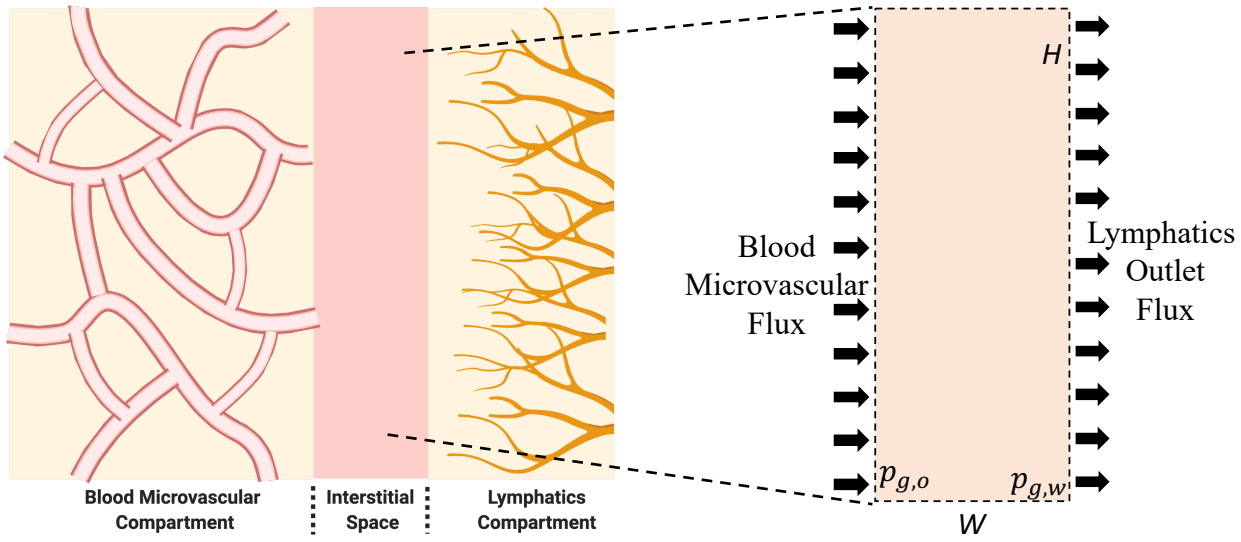

Figure 31: Schematic representation of the on-chip integration of the blood and lymphatic microvascular platforms (left) and the interstitial space region taken as the control volume (right).

We start this analysis by defining a simplified system that would model the tissue interstitium. Based on current microfluidic designs, the on-chip system integrates each vascular model at different compartments with a central gel region acting as the scaffold that bridges between the two vasculatures (**Figure 31**). As such, we can restrict our analysis to this gel region as a one-dimensional system and consider the transport contribution of each vascular compartment as a flux boundary condition. The fluid transport across this gel system can be described on the basis of Darcy's law, discussed earlier in this work as:

$$u = \frac{k}{\mu}\frac{(p_{g,o} - p_{g,w})}{w}$$

where $p_{g,o}$ and $p_{g,i}$ indicate pressures at the initial, blood vascular interface boundary and opposite, lymphatic outlet boundary, respectively, while k represents the hydraulic permeability (previously characterized) and u corresponds to the average interstitial fluid velocity. Additionally, to account for the fluid flux from each vascular compartment, a boundary condition is applied at each adjacent side of the gel region where the fluid flux is given by the Starling equation:

$$u = \frac{A_{s,B}H}{V_{T,B}}L_{p_B}(p_B - p_{g,o}) = \frac{A_{s,L}H}{V_{T,L}}L_{p_L}(p_{g,w} - p_L)$$

where L_p and A_s/V_T correspond to the hydraulic conductivity and vascular surface area per unit tissue volume, respectively. Both parameters have distinctive values corresponding to the particular vascular system, blood (B) or lymphatic (L). Given that oncotic-driven pressure differences are negligible in our *in vitro* systems, hydraulic pressure differences across each vascular compartment determines the rate of fluid transport. For this, we consider a uniform intravascular pressure distribution for the blood (p_B) and lymphatic (p_L) vasculatures. Finally, the length of this boundary (H) is multiplied into the equation to obtain the resultant fluid velocity at each periphery. By applying mass conservation and incompressibility, we can establish that all three independent equations described above, relate to the same fluid velocity. Since all the transport and geometric parameters have been previously characterized, we can solve the corresponding equations to obtain the pressure distribution necessary to impose a physiological interstitial fluid velocity of 0.1 μm/s.

Despite having a total of four unknown pressures, we can consider the fluid pressure at the lymphatic vasculature as the zero-pressure reference, thus allowing us to solve for the remaining pressures. A MATLAB algorithm was generated to solve the system of equations for the desired pressures (see Appendix B). From the solution, we find that by pressurizing the blood microvasculature to a gauge value of 500 Pa, relative to the lymphatic outlet, we are able to establish physiological interstitial fluid flow exiting the blood compartment and drained by the lymphatics. Previous work by our lab have achieved this experimental set-up in our on-chip microvascular networks.

We next consider the protein transport within this interstitial space to which we apply the non-dimensional mass conservation equation for a steady state condition in a uniform velocity field and neglecting uptake or degradation within the computational domain:

$$0 = \frac{D}{u\,w}\frac{\partial^2 \hat{C}}{\partial \hat{x}^2} - \frac{\partial \hat{C}}{\partial \hat{x}} = \frac{1}{Pe}\frac{\partial^2 \hat{C}}{\partial \hat{x}^2} - \frac{\partial \hat{C}}{\partial \hat{x}}$$

where the Peclet number (Pe) naturally arises from the dimensional analysis of the equation and allows us simplify our analysis by weighting the dominant transport mode. On a similar basis to our previous fluid transport analysis, the relative contribution of mass transport by the blood and

lymphatic vasculatures are taken into account with boundary flux conditions. For the blood compartment, the rate at which extruded proteins enter the gel region is given by:

$$N_B = \frac{A_{s,B}H}{V_{T,B}} P_B\left(C_B - C_{g,o}\right) + u\left(1 - \sigma_{f,B}\right) C_B$$

where the diffusive flux is given by the local difference in concentration between the blood compartment (C_B) and the adjacent gel periphery ($C_{g,o}$) times the endothelial permeability (P_B) and the effective endothelial surface area. The convective flux contribution is the product of the local fluid velocity and the solute concentration exiting the compartment while considering reflection effects ($\sigma_{f,B}$) through the endothelium. Accounting for the flux at the lymphatic compartment, we implemented an outflow boundary where the convective flux dominates the transport of proteins through the lymphatics given the results of our scaling analysis in the previous section. As such, the flux equation simplifies to:

$$N_L = u\left(1 - \sigma_{f,L}\right) C_{g,w}$$

where the local concentration at the adjacent lymphatic outlet ($C_{g,o}$) is transported through the lymphatics by convection with filtration effects ($\sigma_{f,L}$) included. For this analysis, we are interested in predicting the ratio of concentrations between the steady protein content in the interstitial space relative to the blood intravascular concentration (C_g/C_B). This allows us to compare the steady state concentration distribution in our *in vitro* system to that of *in vivo* and clinical measurements where this normalized concentration ratio is often implemented. As a model protein, we considered the specific case of albumin transport in our engineered vascular systems. Given our prior characterization on the transport properties of this protein in both our blood and lymphatic microvascular systems, we can directly apply our measured values to this analysis. We first simplify our calculation by considering that the convective transport of albumin would dominate its steady state distribution ($Pe \sim 10$), thus a uniform concentration within the interstitial matrix would follow. Then, we consider that the equilibrium interstitial concentration is determined by the balanced flux of each vascular compartment as:

$$N_B = N_L \,,$$

$$\frac{A_{s,B}H}{V_{T,B}} P_B\left(C_B - C_g\right) + u\left(1 - \sigma_{f,B}\right) C_B = \; u\left(1 - \sigma_{f,L}\right) C_g$$

from which we can directly solve for the normalized concentration (C_g/C_B). We extended our MATLAB algorithm to solve for this mass transport analysis which indicated that the average concentration of albumin in the interstitial region would be 0.32x of the blood intravascular content. We validated this estimation by implementing a COMSOL-based model to obtain a numerical solution to this transport analysis. In line with our calculations, the computational results indicated a uniform concentration distribution in the interstitial region which resulted to be at a value of 0.31x to that of the blood intravascular concentration. This value is well within the reported ranges for clinical assessments of plasma proteins (0.3 - 0.4)[140]. Thus, the integration of the lymphatic vascular platform, described in this work, with our blood microvascular system has the potential to recapitulate the homeostatic, equilibrium concentration of proteins across the interstitial matrix.

Chapter 4: Immune cell recruitment by engineered lymphatics via inflammatory chemotactic axes

4.1 Recapitulating Pathological Immune Cell Recruitment by Engineered Lymphatics

In addition to regulating the transport of diluted proteins and other macromolecules in the interstitium, the lymphatic vasculature plays host to various immune cell trafficking events during host immune responses[9]. In fact, lymphatic capillaries provide systematic surveillance to potential infiltration of pathogenic entities by trapping foreign materials during drainage that end up directed to the lymph nodes. It is at these lymph sacs that residing immune cells, such as lymphocytes and macrophages, are activated by the antigens and/or pathogens which is then followed by their immunogenic response[3]. Additionally, patrolling immune cells in the systemic circulation or at the stromal site of infection can also be activated by local inflammatory signals which leads to them to capture pathogen-specific antigens, migrate towards neighboring lymphatic capillaries and present the antigens to lymphocytes at the lymph nodes, thus facilitating immunogenicity[141].

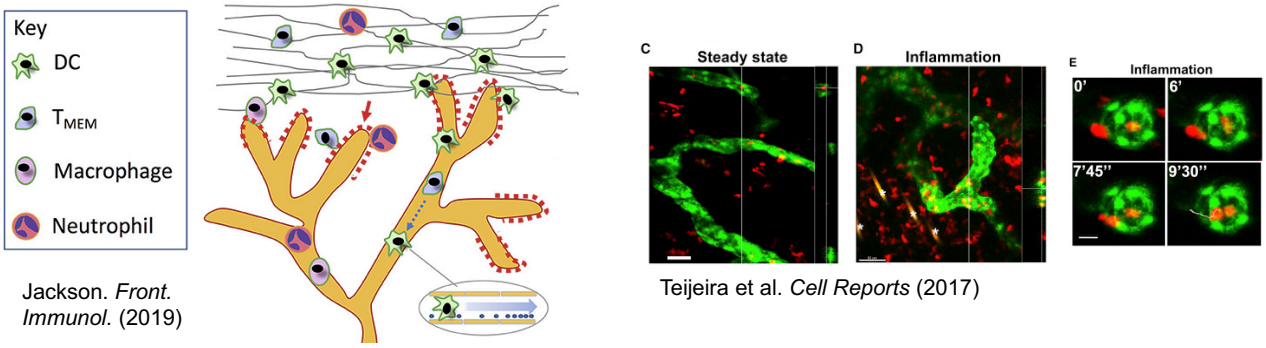

Figure 32: Schematic depicting the different immune cells that infiltrate lymphatic capillaries during immune response[141] (left), and *in vivo* images[142] (right) of immune cells, shown in red and orange, infiltrating the lymphatics, shown in green, during homeostatic and inflamed tissue conditions.

In the event of tissue infection and inflammation, local stromal cells are activated by pathogenic signals, such as bacterial lipopolysaccharide, and respond with the release of inflammatory cytokines including tumor necrosis factor alpha (TNF-α), transforming growth factor-β (TGF-β),

interleukins, amongst many others[141]. This inflamed microenvironment has significant downstream effects on the blood and lymphatic vasculatures such as: increasing the permeability of blood capillaries, which leads to the higher influx of plasma and proteins in the tissue site, thus elevating interstitial fluid flow and lymphatic drainage[143]. Once the tissue site is primed by various pro-inflammatory signals, innate and adaptive immune cells are called upon by blood and lymphatic endothelial-secreted chemokines which then initiates their appropriate immune activation and response[141,144] (**Figure 32**). This cascade of local alterations to the cellular microenvironment underlines the numerous and complex interactions of biochemical and mechanical signals implicated during the host immune response. Thus, in order to adequately study the signaling and migratory events that lead to the recruitment of immune cells to the lymphatics, the full range of fluid, protein and cellular transport phenomena are to be recapitulated in *in vitro* studies.

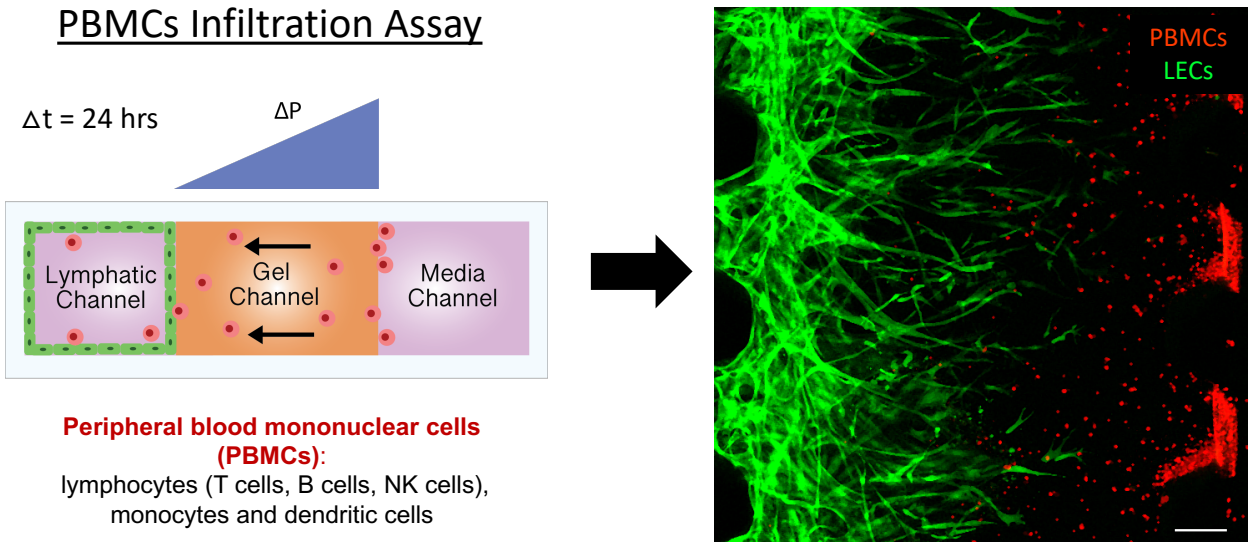

Figure 33: Schematic depicting our PBMCs infiltration assay where the PBMCs are, shown in red using a membrane dye, are introduced into the adjacent media channel under a hydraulic pressure difference inducing pathological flow towards the lymphatics, shown in green.

In addition to modeling lymphatic drainage of interstitial proteins, our platform is amenable to recreating the pathological microenvironment that facilitates the recruitment of immune cells by the lymphatics. As such, immune cells can be introduced into the system at the adjacent media

channel while establishing the appropriate hydraulic pressure difference across the gel compartment to establish pathological interstitial flow (**Figure 33**). Additionally, recombinant-human cytokines can be introduced into the system to mimic stromal secreted inflammatory factors. For the addition of immune cells in our platform, we chose to introduce peripheral blood mononuclear cell (PBMCs) which includes a broad population of immune cells that are naturally found in the systemic circulation, and are known to extravasate and migrate to the lymphatic periphery (**Figure 33**).

Briefly, human blood collected from healthy donors (Research Blood Components, Massachusetts, USA) with anticoagulant sodium citrate, was mixed at a ratio of 1:1 with a buffer solution, consisting of DPBS supplemented with 0.1% BSA (Sigma) and 1 mM of ethylenediaminetetraacetic acid (ThermoFisher), and carefully layered over Ficoll® Paque Plus (Sigma) in a Corning 50 mL centrifuge tube. Then, the layered blood samples were centrifuged at 400 rcf for 35 minutes. Following centrifugation, the upper layer, consisting of plasma, was removed by aspiration, and the remaining buffy layer (containing PBMCs) is transferred to a separate centrifuge tube. Additional purification from any remaining platelets was performed by diluting the isolated PBMCs in buffer solution supplemented to the remaining volume of the 50 mL tube, and centrifuging the resuspended cells at 250 rcf for 10 minutes. Platelets would mostly remain in the supernatant, which was aspirated, and PBMCs remained agglomerated at the bottom. This final step was repeated twice, as recommended by the standard isolation protocol to yield >90% of PBMC purity. All isolation procedures were done at room temperature. Immediately after purification, PBMCs were stained with Cell Tracker™ Green CMFDA Dye (Invitrogen) at a 10 μM concentration for 10 minutes, followed by washing with the buffer solution, and resuspended in cell culture media to a final concentration 1 x 10^6 cells/mL. After the final resuspension, 200 μL of the PBMC solution (~200,000 PBMCs) is perfused into the media channel devoid of lymphatic cells in devices at day 4 of cell culture. Once the PBMCs were introduced into the devices, a hydraulic pressure head was established to drive fluid flow towards the lymphatic channel at pathological interstitial fluid velocities (~4 μm/s) measured in inflamed tissues. Following 24 hours, epifluorescence images were acquired at the lymphatic channel, and the total number of PBMCs was quantified using the TrackMate-plugin in ImageJ. As an initial comparative study, we performed this assay on both growth factors- and high flow-grown three-dimensional lymphatics, as well as the standard lymphatic monolayer system and bare gel samples.

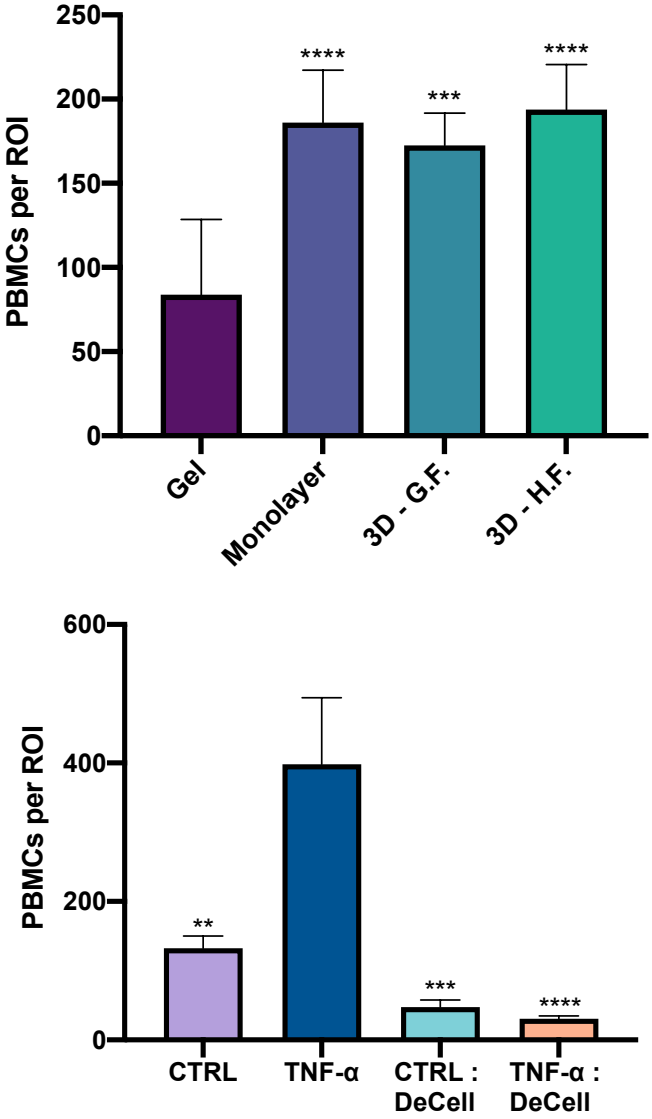

Figure 34: Quantitative analysis from the PBMCs infiltration assay performed on varying experimental conditions as described in the plot (upper). Quantitative analysis from the PBMCs infiltration assay performed on high-flow engineered lymphatics with certain devices stimulated with TNF-α and/or decellularized (lower). Statistical significance is reported with respect to the gel sample (upper) and the TNF-α stimulated lymphatics (lower).

Interestingly, all the experimental conditions that included a lymphatic endothelium exhibited significantly higher numbers of infiltrated PBMCs compared to the bare gel samples (**Figure 34**). This is in line with other *in vitro* studies where the migration and trafficking of immune cells, especially dendritic cells, is augmented in the presence of lymphatic endothelial cells[145]. Such findings suggest that the lymphatics actively recruit patrolling immune cells which is likely due to paracrine signaling between the two cell types. Therefore, in the event of tissue infection and inflammation, these lymphatic-secreted biochemical cues would orchestrate an increased influx of immune cells as a response to the pathogenic contamination[146].

To validated the increased recruitment of immune cells under inflammatory conditions, devices with high flow-engineered lymphatics were pre-treated with 20 ng/mL of TNF-α (Peprotech) overnight. Prior to PBMC perfusion, any remaining TNF-α was washed away to ensure that inflammatory stimulus was solely imparted on the lymphatics. Additionally, based on our previous solute drainage measurements, we also considered decellularized samples to examine if the increased infiltration is solely due to changes in the physical structure of the matrix, by the invading lymphatics sprouts, that could then facilitate the migration of the immune cells. Results from this set of experiments validated that, under inflammatory stimulus, lymphatics significantly increase the recruitment of PBMCs (**Figure 34**). Additionally, decellularized samples consistently exhibited lower infiltration numbers regardless if the device was preconditioned with the inflammatory cytokine TNF-α (**Figure 34**). This provides additional evidence that the increased PBMC infiltration to the lymphatics is a direct consequence of their intervention through biochemical factors, originating from the lymphatics, that provide directional signals to the immune cells.

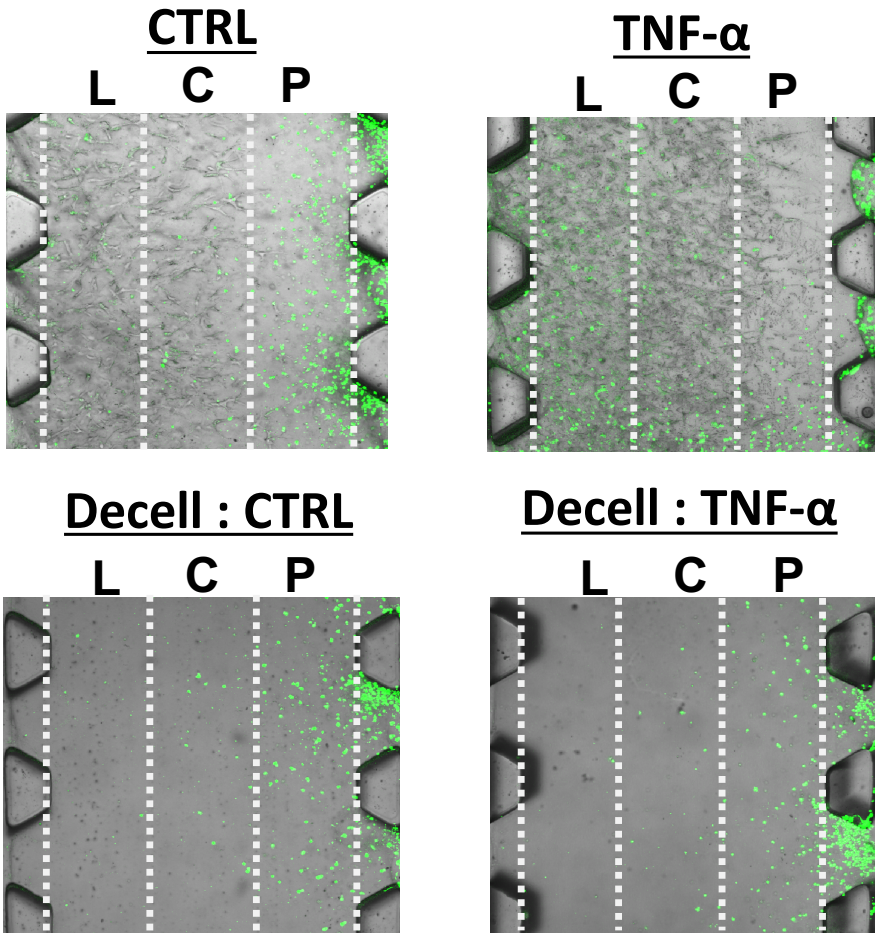

	L	C	P
CTRL	0.05	0.08	0.64
TNF-α	0.77	0.36	0.15
Decell : CTRL	0.04	0.11	0.60
Decell : TNF-α	0.02	0.10	0.67

Figure 35: Representative images showing PBMC distribution within the gel region for each experimental condition where L, C and P correspond to the region co-localized with the lymphatics, the central region and region closest to the PBMCs media channel, respectively (upper). Heat map of PBMC distribution within the gel region for specified conditions and locations (lower).

To further examine the preferential migration and infiltration of PBMCs, confocal imaging of the gel region was done to visualize the spatial distribution of PBMCs immediately after performing the infiltration assay. Quantitative analysis of the images was performed by subdividing the gel in three equally-spaced regions along its width (**Figure 35**), and measuring the average fluorescence intensity of each region which correlated with the density of immune cells. The average intensity for each region was then scaled by implementing linear normalization with ranges set per each corresponding device. Both, images and quantitative data indicate that PBMCs where preferentially localized closer to the media region where they are introduced, for all conditions except the TNF-α-stimulated lymphatics (**Figure 35**). For the latter, the highest population of PBMCs corresponded to the region co-localized with the lymphatic vessels. This provides additional evidence that the inflamed lymphatics are eliciting the preferential migration and infiltration of PBMCs. In the later section we will closer examine the specific chemotactic factors involved in our pathological immune response model.

4.2 Inflammatory Chemotactic Axes during Lymphatic Immune Cell Recruitment

Efforts to understand the basis of immune cell migration to specific sites, during immune response, have elucidated the role of chemokines as homing molecules for immune recruitment[146]. These chemotactic cytokines guide immune cell to different sites and at different steps during immunogenic response which requires the careful coordination and delivery of cell-secreted ligands to the specific immune cell surface receptor, also termed as axes[147] (**Figure 36**). In addition to guiding immune effector cells to sites of infection and inflammation, chemokines coordinate interactions between immune cells during the adaptive immune response[146]. Perhaps the most studied and documented immune chemotactic pathway during inflammation is the lymphatic secreted ligands CCL21 and CCL19 that attract immune cells via their CCR7 receptor during various pathological events including immunogenic response and cancer metastasis[148–150]. Of similar interest, the stromal and endothelial secreted CXCL12, also known as the stromal cell-derived factor-1, that coordinates the homing of immune cells to the bone marrow for immune maintenance and development through the CXCR4 surface receptor[151,152].

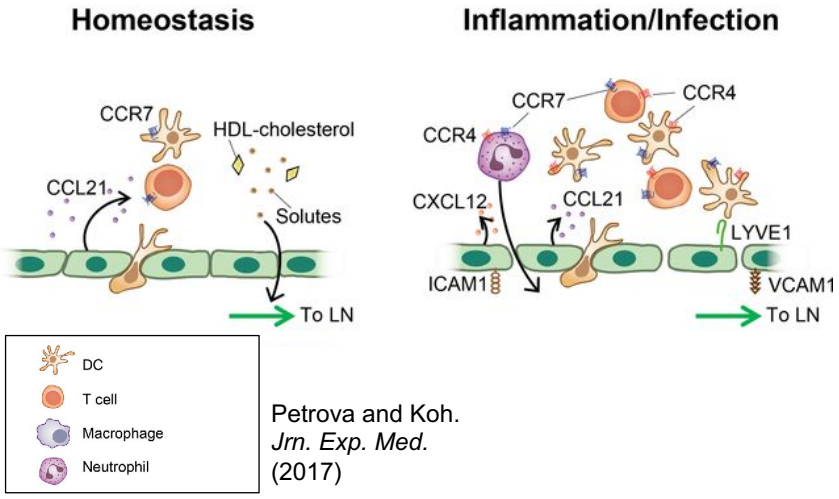

Figure 36: Schematic depicting different physiological scenarios of immune cell recruitment by lymphatic capillaries[153]. Under homeostatic conditions, low numbers of immune cells enter the lymphatics during immune maintenance and surveillance (left). However, in the event of a localized infection, an inflammatory response by the lymphatics ensues, which recruits a greater number and population of immune cells (right).

To determine if the immune cell surface receptors, to these chemotactic axes, are elicited during immune recruitment in our tissue engineered system, we performed receptor blocking experiments where an additional incubation step was implemented before the final resuspension step, with PBMCs incubated in a buffer solution containing CCR7 and/or CXCR4 antibodies, control IgG_{2A} and IgG_{2B} isotypes for 30 minutes. All the humanized antibodies were obtained from the same vendor (R&D Systems) and used at a concentration of 5 μg/mL. Additionally, all the pre-conditioned PBMC samples were introduced into devices with high-flow grown lymphatics stimulated with TNF-α to model an inflamed microenvironment. After performing the PBMCs infiltration assay, the amount of infiltrated PBMCs was quantified as done in previous experiments.

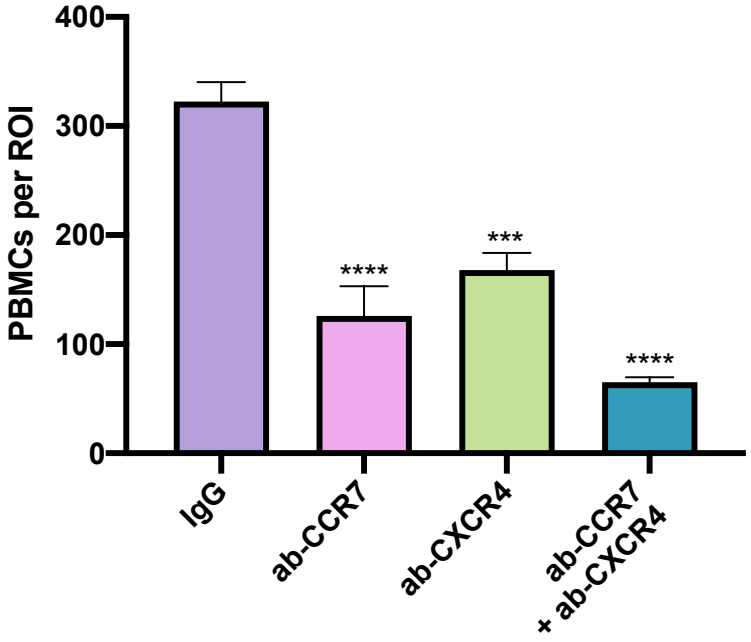

	L	C	P
IgG	0.64	0.41	0.46
CCR7	0.05	0.06	0.51
CXCR4	0.02	0.01	0.70
CCR7 + CXCR4	0.03	0.12	0.58

Figure 37: Quantitative analysis from the PBMCs infiltration assay performed on high-flow engineered lymphatics stimulated with TNF-α and with corresponding conditions of PBMCs reconstituted in neutralizing antibodies or IgG isotypes (upper). Statistical significance is reported with respect to the experimental condition with PBMCs reconstituted in IgG isotypes. Heat map of PBMC distribution within the gel region for specified conditions and locations (lower).

For this panel of experiments, we observed a consistent, and significant, decrease in the number of infiltrated PBMCs when their cell surface receptors, CCR7 and/or CXCR4, are functionally blocked, compared to the IgG isotype control, despite being introduced into devices with inflammatory-stimulated lymphatics (**Figure 37**). Furthermore, analysis of the spatial distribution of PBMCs within the gel region reveals that solely for the IgG isotype control samples, the PBMCs preferentially migrated and co-localized at the inflamed lymphatics region (**Figure 37**). All other samples with neutralizing antibody treatment displayed higher PBMC numbers closer to the media channel. Thus, the CCR7 and CXCR4 immune cell surface receptors, responsible for immune homing, are elicited in our engineered pathological model for immune cell recruitment by the lymphatics in response to local inflammatory stimulus. It should be noted, however, that additional immune cell receptors are likely activated during the recruitment of PBMCs in our infiltration assay, and future studies to interrogate activated immune chemotactic receptors during lymphatic recruitment can be performed with this platform.

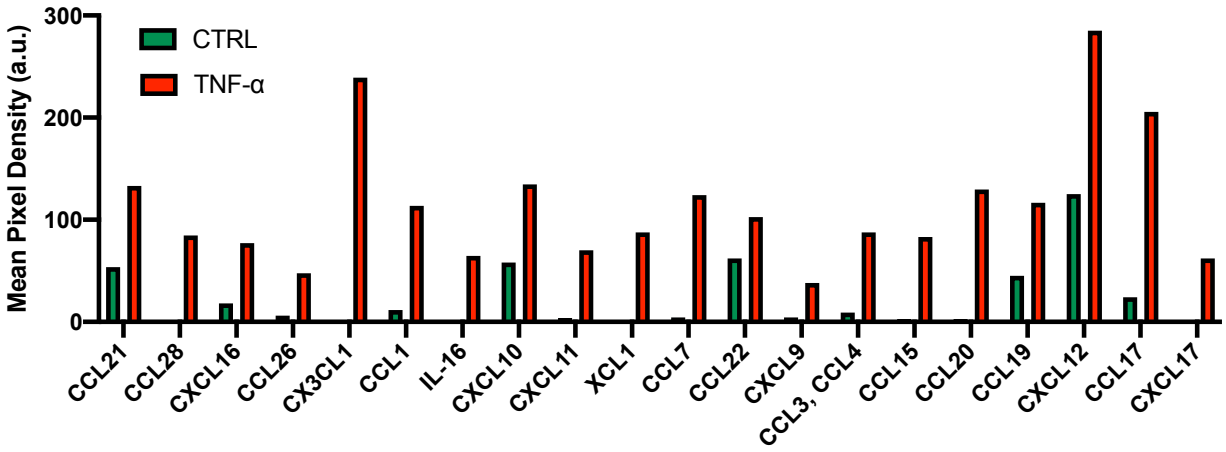

Figure 38: Quantitative analysis of cytokine secretion by lymphatics grown under interstitial flow with one experimental group pre-conditioned with TNF-α prior to collecting their respective supernatant.

To comprehensively validate the increase activation and recruitment of PBMCs by lymphatic-secreted chemokines during inflammation, we quantified cytokine expression by collecting the supernatant from lymphatic cells cultured under the similar experimental conditions. Prior to collection, lymphatic endothelial cells (~10^6 cells) were seeded on a Corning™ Transwell

Membrane Inserts with 0.4um pores (Sigma). After 24 hours of culture a lymphatic monolayer is established on the transwell insert, and 1 mL of fibrin gel was injected on top of the monolayer and allowed to polymerize. Subsequently, cell culture media was added to the top of the gel inducing interstitial flow (~4 μm/s) towards the lymphatics with one of the transwell inserts having cell culture media supplemented with 20 ng/mL of TNF-α. Following 24 hours of culture under these conditions, the supernatants were collected and assayed in a Proteome Profiler Human Chemokine Array (ARY017, R&D systems) following manufacturer's protocol. Quantitative analysis of the cytokine intensity between both experimental conditions revealed a persistent increase in chemokine secretion by the TNF-α-conditioned lymphatics, with an approximate 2.5-fold increase for CCL19, CCL21 and CXCL12 (**Figure 38**). Conclusively, the immune surface receptors CCR7 and CXCR4 mediate the increase infiltration of PBMCs while the engineered lymphatics secrete corresponding ligands that activate these chemotactic receptors within our inflammatory immune recruitment model.

4.3 Flow-Induced Concentration Gradients of Lymphatic-Secreted Chemokines

From our experimental work in the previous sections, we verified that the increased immune recruitment by our engineered lymphatic system is mediated by key chemotactic axes in which the lymphatics act as a localized source of chemokines that attract the immune cells. However, when considering the physiological environment by which these chemokines are secreted into the extracellular matrix, most of them remain soluble or, alternatively, bind to the matrix, which would result in concentration gradients[154–156]. Thus, facilitating the directed migration and recruitment of the immune cells to the specific tissue or vasculature via graded chemical concentrations[157,158]. In fact, such concentration gradients are ubiquitous in biological processes, including spatially-defined cellular differentiation (morphogenesis)[159], and are a key phenomenon for long range cell signaling including cancer metastasis[160]. In order to emulate the paracrine signaling that leads to the recruitment of immune cells in our engineered system, we must validate that these biochemical signals are delivered under a similar physiological transport mechanism.

Table 2: Experimental and computational default parameters for chemokine transport model.

Diffusion coefficient of chemokines	D_{ch}	14.5 x 10^{-11} m^2/s
Flux of chemokines from the lymphatics	N_{ch}	1 x 10^{-6} – 2.5 x 10^{-6} mol/m^2 s
Hydraulic conductivity of high flow-grown lymphatics	$L_{p\ HF}$	8.1 x 10^{-6} m/Pa s
Chemokine permeability in high flow-grown lymphatics	$P_{HF,\ ch}$	7 x 10^{-8} m/s
Reflection coefficient of chemokines	$\sigma_{f,\ ch}$	0.2
Consumption rate of chemokines by PBMCs	R_{ch}	0.5 x C mol/s

To model the spatial distribution of chemotactic factors during the immune recruitment assay, we extended upon the preceding lymphatic drainage model, and incorporated an additional domain consisting of solid (impermeable) spheres embedded in the gel region which represented the migrating PBMCs. Transport equations were implemented based on our previous framework, and a reaction term was also incorporated, to account for the consumption of chemokines by the immune cells, based on similar studies. Pressure boundary conditions were set at the same magnitude as the immune recruitment experiments to establish pathological interstitial flow. A zero-concentration boundary condition was imposed at the inlet and convective outflow boundary at the outlet. Of special interest is the local secretion of chemokines by the lymphatics which was represented in the model as a constant flux condition at the endothelial domain. Despite not having experimental characterization of the secretion rates, we do have quantitative insight on the relative increase of secreted chemokines between the TNF-α-stimulated lymphatics and the unstimulated condition from the cytokine array analysis. For the diffusivity and endothelial transport properties corresponding to the chemokines, an average value was implemented based on the range of molecular weights corresponding to the chemokines of interest (CCL21, CCL19 and CXCL12)[161]. A quasi-steady state assumption was implemented in the numerical solution. Given that the timescale for diffusive and convective phenomena is 10-100 orders of magnitude less than the timescale for cell migration (1-10 μm/hr)[78,161], thus the spatial distribution of the chemokine reaches equilibrium prior to any cellular events. From this, we are able to obtain a generalized picture on the distribution of chemokines relative to the immune cells as they migrate through the system. All parameters used for the simulations are listed in Table 2.

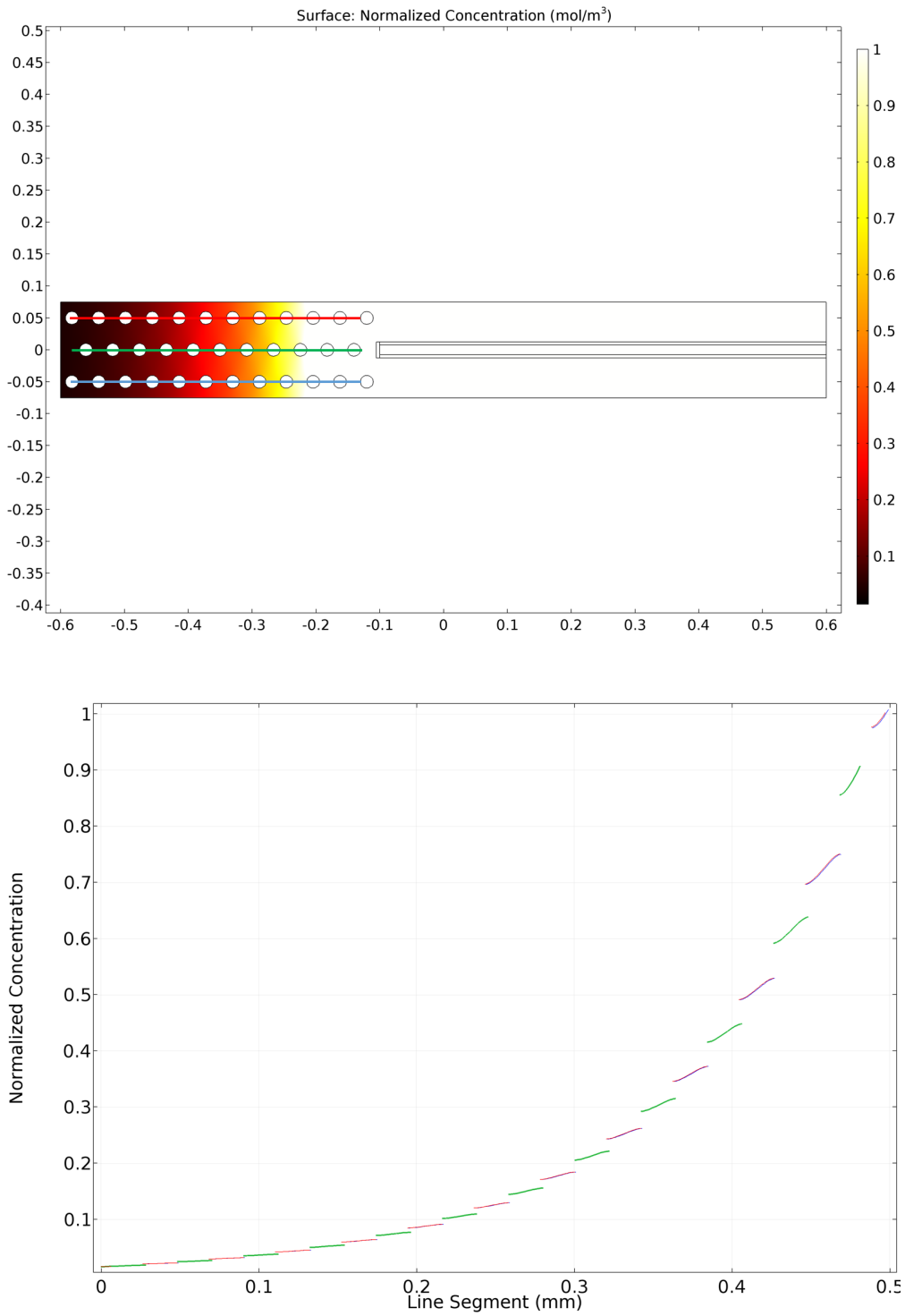

Figure 39: Computational model results for lymphatic chemokine transport developed in COMSOL Multiphysics depicting the normalized concentration of the chemokines. (upper) A series of line probes are positioned over the spheres representing PBMCs and the corresponding concentration is shown depicted in the spatial concentration plot (lower).

Computational modelling of chemokine transport affirms the ability of our platform to recapitulate concentration gradients of lymphatic-secreted chemokines (**Figure 39**). In fact, numerical results indicate that the spatial distribution of the chemokine follows a steep concentration gradient leading towards the lymphatics. This gradient is facilitated by the relative competition between the interstitial flow that skews the symmetric diffusion profile of the chemokines, thus resulting in a trail of lower concentration as the farther distances from the chemokine source (lymphatics). We can provide additional quantitative basis to this phenomenon by considering the scaling analysis provided by the Peclet number, as described in previous sections. The corresponding value for the Peclet number is roughly 10 (considering the length from the concentration line probe), which is within the characterized range of flow-induced transcellular gradients of cell secreted factors. However, an additional aspect is to be evaluated which is the relative difference between homeostatic and inflamed lymphatics with varying rates of chemokine secretion. From our previous experimental results, we found that the chemokines of interest are secreted at a 2.5x increased rate for inflammatory-stimulated lymphatics. We applied this relative increase to the flux of species by the lymphatic sprout in our model to which we found a significantly steeper profile in the concentration gradient of the chemokines (**Figure 40**). As extensively studied *in vitro*[162–164], such increase in spatial gradients of chemotactic factors results in faster and persistent migration patterns by immune cells which is in line with our experimental findings that higher numbers of immune cells infiltrate our inflamed lymphatics model.

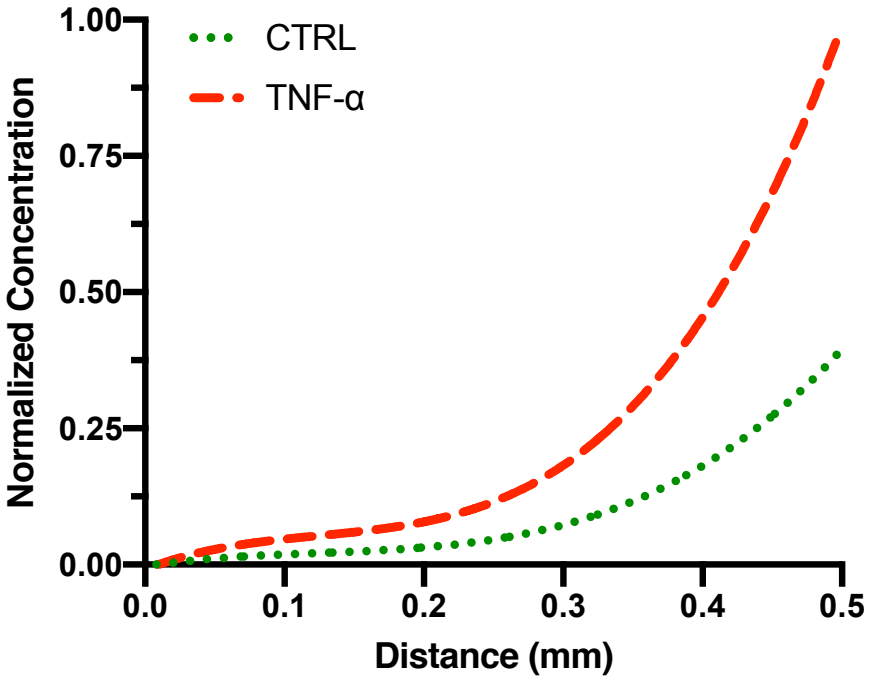

Figure 40: Computational model results for lymphatic chemokine transport developed in COMSOL Multiphysics depicting the normalized concentration spatial profile of the chemokines considering differences in secretion rate by untreated (control) lymphatics and TNF-α-stimulated samples.

Chapter 5: Pharmacokinetics and Vascular Absorption of subcutaneously-delivered therapeutic monoclonal antibodies

5.1 Screening Vascular Absorption of Therapeutic Monoclonal Antibodies

Since the introduction of their hybridoma-based synthesis in 1975, monoclonal antibodies (mABs) have become a standard research tool, and the prevalent treatment modality for various diseases, including cancer therapy[165]. Their popular implementation for therapeutics resides in the ability to engineer mABs with specific binding targets and affinity kinetics to a variety of target molecules including soluble proteins, cell-surface receptors, and pathogenic agents[165]. For mAB-based cancer therapeutics, this flexibility has been exploited by developing mABs that induce anti-cancer response through different mechanisms[165] (**Figure 41**) including: directly targeting cancer cells to induce apoptosis, altering the host response by checkpoint blockade immunotherapy, and conjugating cytotoxic agents (radioisotopes and toxic drugs) to the mABs for directed delivery to cancer cells. However, the therapeutic outcome of mAB-based treatments is not only dependent on the careful design of their binding kinetics and induced-cellular response, but, concurrently, on their adequate delivery and transport in the host; thus, ensuring that sufficient mABs arrive at the molecular targets to induce the intended therapeutic effect[166].

Subcutaneous delivery of therapeutics has been a preferred method of administration by patients and healthcare works, over intravenous injections, due to their increased patient throughput (by reducing administration time and cost), and amenability for self-administered or caregiver-supported dosing at home[167,168]. Under such effort, several mABs and Fc-fusion proteins have been recently approved for subcutaneous administration, with a growing interest by other companies to standardize the delivery of their mAB-based treatments through subcutaneous injection[169]. Yet, despite its ease of use and cost-effectiveness, aspects regarding the dosing, and percentage that enters the systemic circulation and is distributed amongst the desired organ/tissue target remains poorly understood[166]. As such, there is currently a lack of reliable preclinical evaluation protocols

to predict the biological distribution of subcutaneously-delivered biologics in patients, thus skewing efforts to develop mAB-based treatments that are administered through this route.

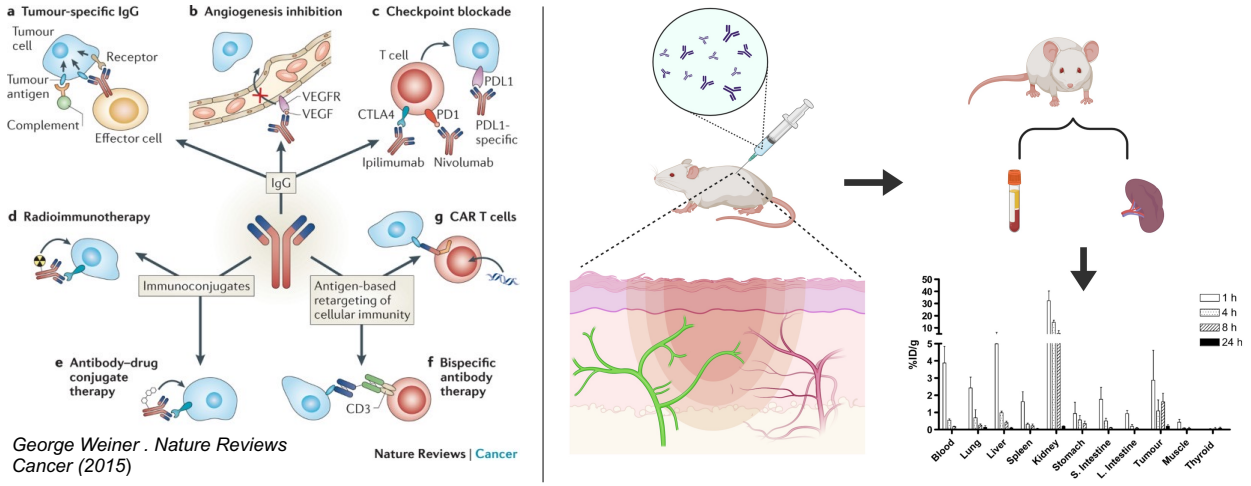

Figure 41: Different therapeutic strategies of monoclonal antibody-based cancer treatments[165] (left). Schematic steps of a standard biodistribution *in vivo* study of subcutaneously-delivered monoclonal antibodies (right).

In an effort to preclinically evaluate the efficacy of subcutaneously-delivered mABs, *in vivo* studies have been thoroughly implemented to study the biodistribution of the mABs by sampling blood and harvesting organs from the subject to determine the resulting amounts of the mABs at different organ/tissue sites[170] (**Figure 41**). Despite providing data into the physiological transport of the mABs, such approach cannot discern the preferred vascular pathway, blood or lymphatic, undertaken by the mAB upon injection, nor the rate of transport to each vascular compartment. Furthermore, this approach requires constant sampling and multiple animal subjects in order to obtain an approximate temporal profile of the concentration across the different compartments. Results from these *in vivo* studies are also marked by interspecies differences which hinders their applicability to predict human response[166]. Given the experimental difficulties and limitations by this approach, biopharmaceutical efforts have been guided towards developing new protocols to predict the biodistribution of novel mABs with tools that better emulate the human-specific physiological transport.

With the recent and promising advances of microphysiological platforms as robust systems to predict human physiology and drug response[171], we extended the capabilities of our microvascular

platforms to study the vascular absorption of mABs developed by our industry collaborator, Amgen Inc. Given that we are interested in studying the transport of subcutaneously delivery mABs, we implemented human-sourced dermal endothelial cells for engineering the microvasculature in our microfluidic platforms. As such, we had a dedicated system to measure the vascular absorption to the dermal blood microvasculature, and the dermal lymphatic microvascular platform, developed in this work, to study the lymphatic drainage of the mABs (**Figure 42**). The mABs provided by Amgen Inc. were conjugated with FITC, which allowed us to perform our vascular absorption assays via fluorescent imaging, as described in previous sections. For proprietary reasons, the name or binding targets of the mABs cannot be disclosed at the moment; however, such information is not relevant to our transport study, thus its omission should not affect the outcome of our results and analysis. We will refer to the mABs as a numbered list (mAB1, mAB2, …) with the assigned number for each mAB consistent across the different plots shown. We also implemented the trastuzumab, an FDA-approved mAB for the treatment of breast cancer[171], as comparative benchmark against the panel of mABs in our study.

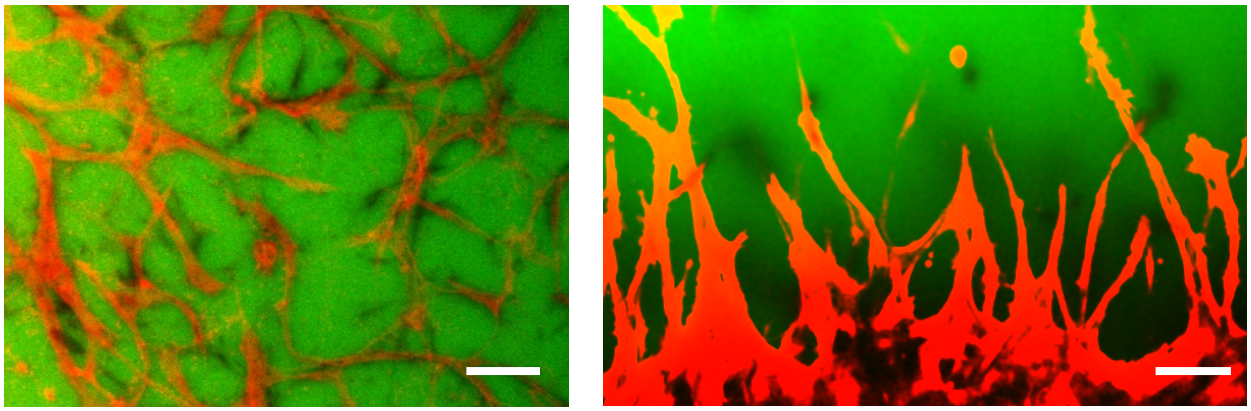

Figure 42: Representative images of the dermal blood microvascular platform (left), with red showing the lectin staining on the endothelial cells and green corresponding to the FITC-mAB, and the dermal lymphatic microvascular model (right) with red showing the RFP-expressing lymphatic endothelial cells and the FITC-mAB as green. All scale bars are 50 µm.

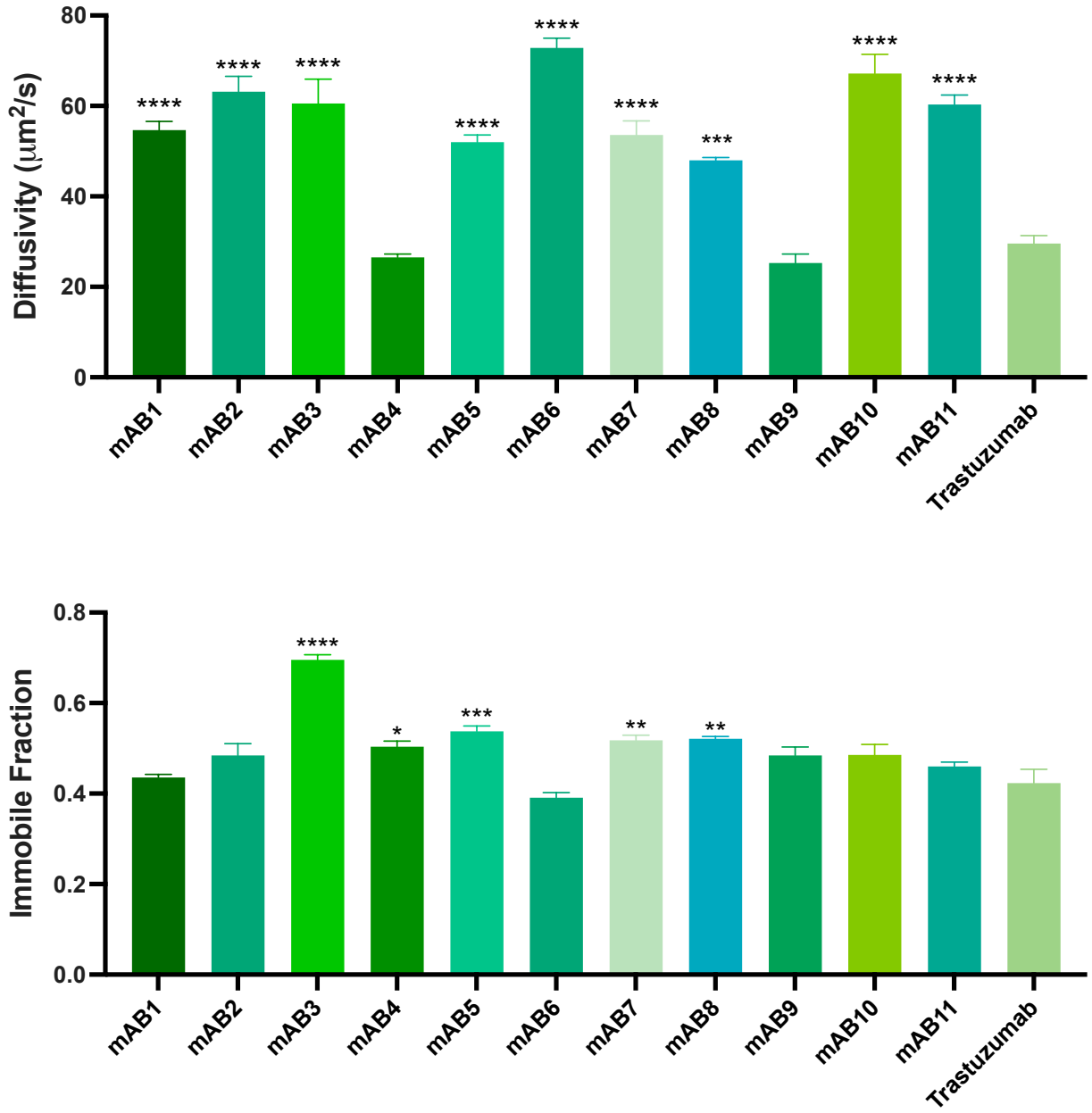

Figure 43: Quantitative analysis corresponding to the diffusivity of the mABs measured by fluorescence recovery (upper), and the corresponding immobile fraction (lower). Statistical significance is reported in refrence to trastuzumab in both plots.

Prior to measuring the absorption into the respective vascular compartments, we took advantage of the fluorescence signal from the mABs to measure its transport across the extracellular space. For this, we implemented FRAP, as previously described, to which we are able to extract the diffusion coefficient and immobile fraction of the different mABs (**Figure 43**) by implementing

the MATLAB frap_analysis plugin. The full panel of mABs are humanized IgG1-based mABs (except for mAB11 which is IgG2-based), with only distinctive molecular affinities at their antigen-binding fragment (Fab) regions. Thus, their molecular sizes correspond to the standard 150 kDa of IgGs. Interestingly, despite their similar size, we found that the mABs exhibited varying magnitudes of diffusivities, with differences up to 63% amongst the mAB panel, with statistical significance against the lower diffusivity exhibited by trastuzumab. We also measured the fraction of immobile species, corresponding to the proportion of mABs that remained bound to the extracellular matrix, to which we found a high degree of binding amongst all the mABs, including trastuzumab. This could be attributed to non-specific charge and binding interactions that mABs are well-known to exhibit, such as in their implementation for enzyme-linked immunosorbent assays where non-specific binding contributes to unwanted background/noise signal. Collectively, these results start to demonstrate marked differences in the transport between mABs, despite their similar size, which are also followed by strong binding interactions in the tissue space. Looking back at differences in the diffusion coefficient, mABs are known to self-aggregate upon injection, which would lower their diffusive mobility by increasing their effective size, and, thus, steric interactions in the tissue medium. Such effects could possibly be reflected in our system upon introducing the mABs into the matrix compartment.

Once the mABs were transported across the matrix, we continued our analysis to assess the vascular absorption rate correspondingly to the blood or lymphatic interface. For the dermal blood microvasculature, we focused on the diffusive permeability of the mABs, given that this would be the only mode of transport and direct entry into the systemic circulation from the interstitial space. For the permeability assessment, we carefully introduced the mABs into the interstitial space, and allowed its diffusion into the vascular lumen compartments. Hence, the reported permeability value corresponds to measuring of the basal-to-apical diffusive transport of the mABs. While for the dermal lymphatics, we focused on the convective transport during interstitial drainage by the lymphatics, on the basis of our previous scaling analysis (see Chapter 3), in which the Peclet number consistently indicates dominance of the convective transport of solutes. Thus, we implemented our previously described solute drainage rate as the metric to consider the absorption to the lymphatic compartment.

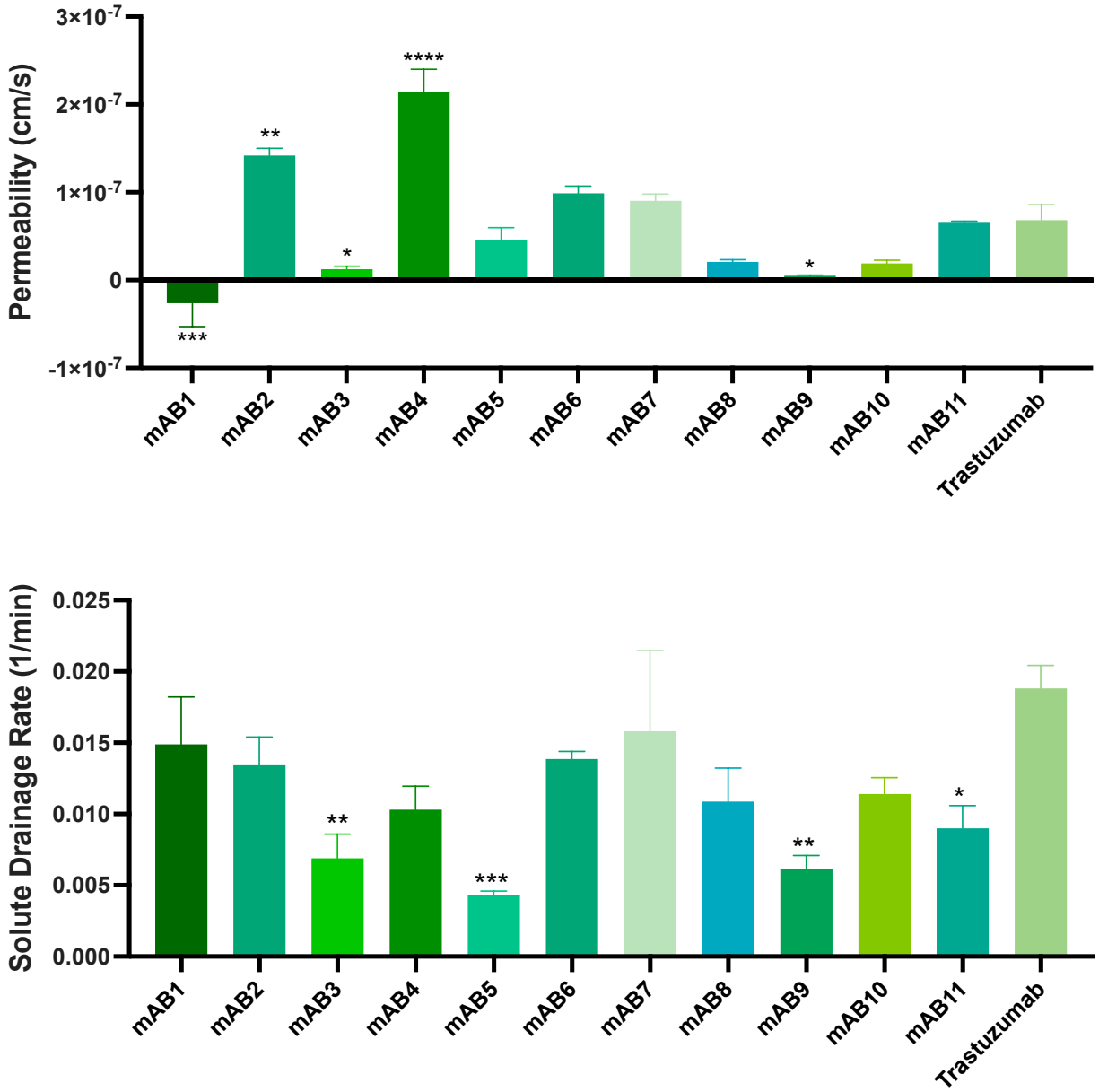

Figure 44: Quantitative analysis corresponding to the diffusive permeability in for the dermal blood microvasculature (upper), and dermal lymphatics solute drainage rate (lower). Statistical significance is reported in reference to trastuzumab in both plots.

With respect to the absorption at the blood vascular interface, we observed significant differences in the permeability amongst the mAB panel (**Figure 44**), with remarkable differences in values up to 2-orders of magnitude. However, given the exceedingly low values of permeability (down to an order of 10^{-11}), we performed additional statistical analysis to validate if the measured data are

significantly different from a zero-mean value. By this analysis, we found that the coupled value and variance from mAB1, mAB3, mAB5, and, even, trastuzumab did not result in values that could be disregarded as zero. As such, these measurements reveal that the transport of mABs across the blood endothelium occurs at rates such that values approach the fluorescence detection limit of our confocal imaging system. This is especially relevant for mAB1, which exhibited a negative mean value for its permeability. Although one could argue that active transport (transcytosis) could, in fact, recycle the mABs back into the matrix compartment, this transcytotic transport would still be occurring at exceedingly slow timescale. Thus, absorption through the blood vasculature does not appear to be the predominant vascular pathway favored by the mABs, which is in line with previous *in vivo* pharmacokinetics study. As we turn our attention to the lymphatic absorption of these mABs (**Figure 44**), we first observe that all the mABs and trastuzumab exhibit physiological ranges of solute drained rates, in comparison to *in vivo* clearance assays (0.005-0.025 min^{-1}). Thus, supporting the expectation that the mABs would most likely be absorbed by the lymphatics at the tissue site, owing to its physiological function. We can provide additional quantitative basis to this hypothesis by scaling analysis, to directly compare the dominant vascular absorption rate. For this, we consider the Peclet number, which in this case compares the blood diffusive permeability rate (P_B) to that of the lymphatic convective absorption rate, measured as the solute drainage rate (k_{lymph}), by the following analysis:

$$Pe_{B/L} = \frac{k_{lymph}}{P_B \;\; S.A._B^*}$$

where $S.A._B^*$ denotes the specific blood vascular surface area per unit tissue volume, with units of m^{-1}. Considering the full range of measured rates, the lowest and highest Peclet number are, correspondingly, 13 and 333, thus confirming that lymphatic convective transport consistently dominates the absorption of the mABs. In addition, we also observed that in comparison to trastuzumab, which exhibited the highest drainage rate, a selected few mABs exhibited significantly slower drainage rates. We hypothesize that such differences in absorption rates would alter the temporal biodistribution of mABs in the systemic circulation. This will be addressed through additional analysis in the later section where we will discuss the physiological-based modelling of mAB pharmacokinetics.

Given that we consistently observed distinctive trends in the transport properties corresponding to an all IgG-based mAB panel, it would be insightful and practical to understand how alterations in their Fab region led to these distinctive trends. In fact, these localized modifications have been shown to give rise to unique biophysical properties (charge, non-specific binding interactions, hydrophobicity), and correspondingly influence the absorption of the mABs[172,173]. However, these biophysical properties were not systematically varied amongst the provided mABs, as such these attributes emerged at spontaneous degrees, upon Fab modifications. Thus, not allowing for control-refrence comparisons amongst the mAB panel, and rendering difficult any direct extrapolation of trends or relationships between our measured transport parameters and their wide range of physical attributes and interactions. To address this limitation, efforts are underway, with Amgen Inc., to implement advanced-learning algorithms[172,173] that can efficiently and accurately identify unnoticed trends within the extensive data set between their biophysical characterization parameters (from ~30 distinctive assays), and our contributed data on the corresponding physiological transport properties of the mABs.

5.2 Pharmacokinetics Modelling of Monoclonal Antibody Transport and Bioavailability

In the previous section, we leveraged the physiological capabilities of our microphysiological systems to directly measure the vascular absorption kinetics of the fluorescently-conjugated mABs, thus facilitating the development of pre-clinical assays that can predict the physiological transport of mABs into the corresponding vascular compartments. However, these measurements do not provide a direct estimate to the corresponding biodistribution of the mABs once they are introduced into a host. For this, additional compartmental analysis is required to account for the systemic, physiological transport of the mAB across different tissue and vascular sites[174,175]. Under this approach, we can develop a mathematical framework to predict the efficacy of the therapeutic agent, in terms of the resultant concentration in the systemic circulation that would later reach the molecular target at a specific organ/tissue. Furthermore, such mathematical modeling can be implemented to optimize dosing strategies including dose concentration and injection location.

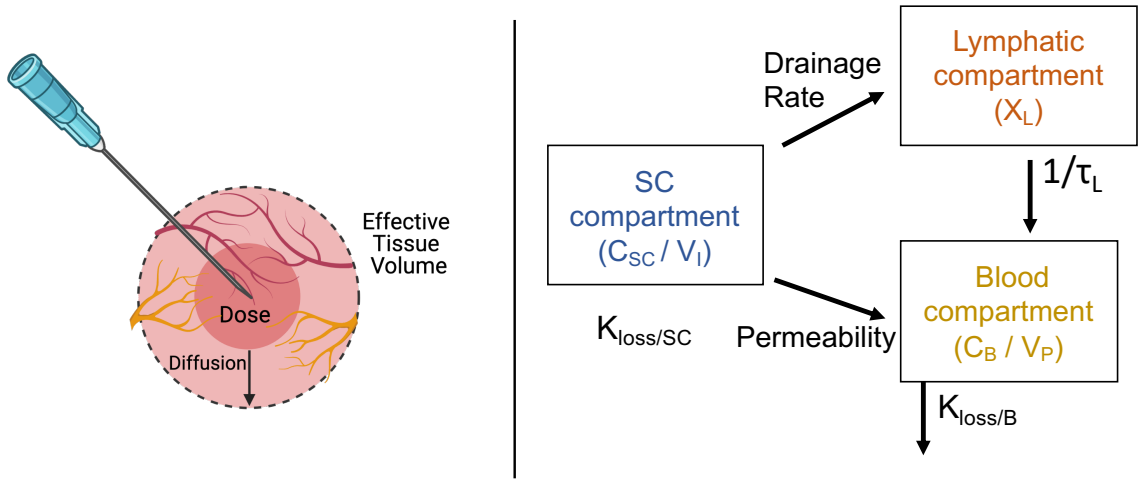

Figure 45: Schematic of the mAB dose injection at the subcutaneous compartment which defines an initial tissue volume where the mABs are located, which then extends under the effects of diffusion (left). A schematic diagram of the compartmental pharmacokinetics analysis following the subcutaneous injection of the mABs.

We start our analysis by defining the relevant compartments across which the mABs are accumulated and transported once they are introduced into the host. Under a physiological basis, we delineate these compartments by the tissue and vascular spaces through which the mAB travels under physiological processes. As such, when the dose is initially injected in the subcutaneous region, the mABs are contained within that dose volume (V_D) introduced into the tissue site. Within this initial volume, local blood and lymphatic capillaries initiate the absorption of the mABs into their corresponding compartments, which are then transported into the systemic circulation and diluted in the blood plasma (**Figure 45**). However, while vascular absorption is occurring, the mABs, that remain in the interstitial space, can diffuse out into the surrounding matrix, thus encompassing a greater volumetric tissue space, than that of the initial dose volume (**Figure 45**). This, in turn, increases the area of vascular interfaces that absorb the mABs from this subcutaneous compartment. To account for this, we considered that from the initial dose volume, assume spherical for simplicity, the mABs diffuse out into the tissue thus encapsulating an effective tissue volume which we define as:

$$V_T = \frac{4}{3}\pi \left(r_{Dose} + \sqrt{6\,D\,t}\right)^3$$

where r_{Dose} corresponds to the radius encircling the initial dose volume, and D indicates the diffusion coefficient of the mAB, which was approximated from previous measurements for IgG[176], and t indicates the time since injection. As depicted in the above equation, we scaled the increase in radius by the three-dimensional diffusive migration of the mABs in the matrix. Within this tissue volume, we also need to account for the interstitial region where the mABs remain prior to their absorption to a vascular compartment. Thus, we define this interstitial region by subtracting the corresponding fraction of local blood and lymphatic vascular compartments in the effective tissue volume as:

$$V_I = V_T\,(1 - \phi_B - \phi_L)$$

where ϕ_B and ϕ_L indicate to the vascular blood and lymphatic volume fraction, respectively. Thus far, we have carefully defined the corresponding volumes, at the different tissue and vascular spaces, since the transport of mABs follows with drastic changes in their concentration, owing to the distinctive volumetric allocation across compartments. To this point, we will consider the transport on the basis of species amount, instead of species concentration, thus accounting for any dilution or concentrate effects while shifting compartments.

From the vascular absorption rates that we previously measured, vascular permeability (P_B) and solute drainage rate (k_{lymph}), we can describe the species flux from the interstitial, subcutaneous compartment into the local vascular spaces (lymphatic or blood). For the species flux into the lymphatics, we consider that the implemented solute drainage rate (k_{lymph}) bulks together the transport parameters describing the convective flux into the lymphatic compartment as:

$$k_{lymph} \approx \left(1 - \sigma_f\right) u_{TE}\, S.A._L^*$$

where σ_f is the solute reflection coefficient, u_{TE} corresponds to the lymphatic transendothelial fluid velocity, and $S.A._L^*$ indicates the specific lymphatic vascular surface area per unit tissue volume. Additionally, we also accounted for local elimination by consumption and degradation by a first-

order rate constant ($k_{loss,SC}$). Thus, the rate change in species amount at this subcutaneous (interstitial) compartment is governed by:

$$\frac{d(V_I C_{sc})}{dt} = -k_{lymph} V_I C_{sc} - P_B \, S.A._B^* \, V_I (C_{sc} - C_B) \; - k_{loss,sc} V_I C_{sc}$$

where C_{sc} and C_B correspond to the concentration in the local subcutaneous and blood compartments, respectively. Note that the interstitial volume term remains within the time differential since this value changes over time, as we previously described. Therefore, the differential operator is applied to the time-dependent function that we used to describe the interstitial tissue compartment.

Since we do not require a concentration term to describe the transport of species across the lymphatic compartment, we can directly consider a total species term for the rate change of species at this compartment as:

$$\frac{dX_L}{dt} = k_{lymph} V_I C_{sc} - \left(\frac{1}{\tau}\right) X_L$$

where τ corresponds to the transit time for which lymphatic-collected plasma is re-introduced into the systemic circulation. This transit time is taken from *in vivo* studies where a time estimate is provided for the lymphatic recirculation of local plasma from a distant dermal site, such as a limb, back to the vena cava by the lymphatic outflow[174,177]. Finally, the corresponding mass transport equation at the blood compartment is given by:

$$V_P \frac{dC_B}{dt} = P_B \, S.A._B^* \, V_I (C_{sc} - C_B) + \left(\frac{1}{\tau}\right) X_L - k_{loss,B} V_P C_B$$

where V_p indicates the total volume of circulating plasma which remains mostly constant over time for a given host, and $k_{loss,P}$ accounts for systemic consumption and filtration. It should be noted that we are limiting our analysis to a 24-hour window, which is within the typical time frame at which the maximum amount of mABs would enter the systemic circulation. For longer times, additional compartments need to be accounted such as specific organs at which the mABs would be deposited

following their entry to the blood, which could be the subject of our future works. Furthermore, we are disregarding additional binding kinetics at the interstitial compartment that would introduce delays in the local depletion of IgG such as reversible binding interactions with matrix components, and cellular uptake and recycling; however, previous pharmacokinetics models have shown that these kinetics typically have negligible effects on the maximum content that reaches the blood[178].

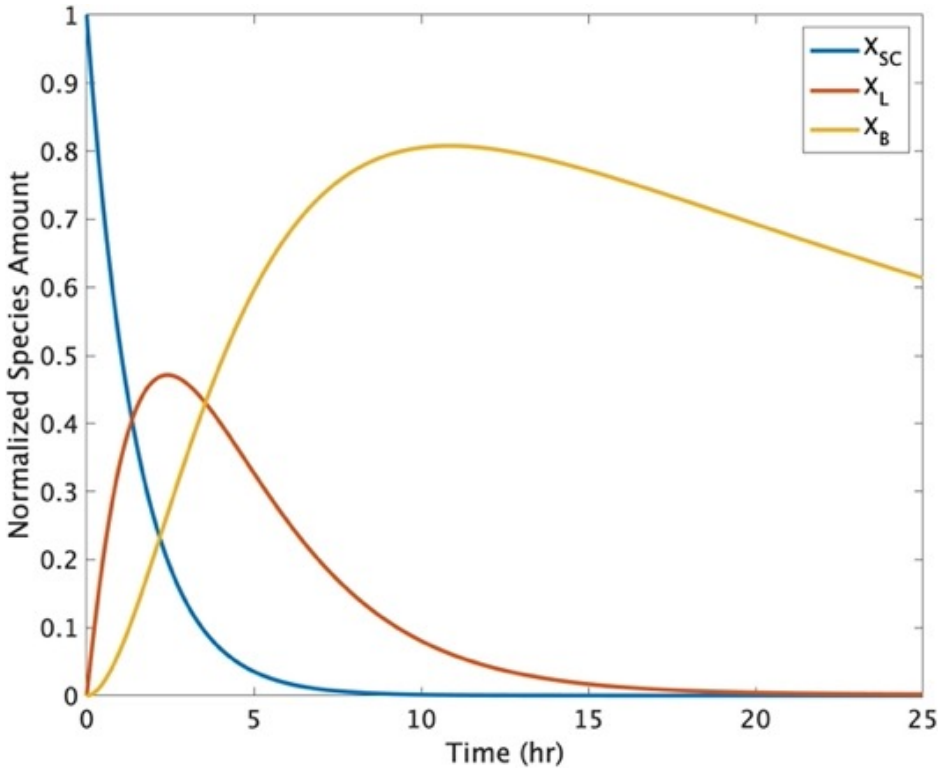

Figure 46: Temporal plot of the normalized species amount across the different physiological compartments from our pharmacokinetics model. X_{SC}, X_L and X_B correspond to the species in the subcutaneous, lymphatic and blood compartments, respectively.

The previous set of differential equations were compiled in a MATLAB algorithm (see Appendix 3), and numerically solved using the ode23s MATLAB solver. From numerical solution, we can predict the temporal profiles of the species amount at each physiological compartment (**Figure 46**). For the input parameters in the model, we considered the vascular absorption rates from our previous measurements and coupled it with previous *in vivo* studies on the elimination rates, and volumetric measurements of the organ and vascular compartments in small mice[177,179,180]. This

allowed to compare our modelling results with *in vivo* pharmacokinetics measurements. From the plotted curves, we can confirm that most of the vascular absorption would occur towards the lymphatic compartment (**Figure 46**), which is in agreement with our scaling analysis in the previous section and *in vivo* studies[181]. Note that we are plotting the species amount, from which we can observe a consistently lesser amount of species at the local blood compartment, compared to that at the systemic plasma, however, the corresponding concentration across these compartments remains mostly the same over longer times due to recirculation. Furthermore, due to elimination kinetics, the total amount of mABs that would reach the systemic circulation would be significantly lower than that from the administered dose. This underlies additional consideration for clinical efforts to ensure that an adequate amount of mABs reaches their molecular target to provoke a therapeutic response. Under this effort, we can implement our pharmacokinetics model to predict the maximum amount of mABs that would reach the systemic circulation (plasma compartment) relative to that of the administered dose, which is pharmacokinetic parameter referenced as the bioavailability. Previous *in vivo* pharmacokinetics studies with trastuzumab have measured that its maximum bioavailability in mice was approximately 80%, which reasonably comparable to our model prediction of 75%. Additional efforts are underway with Amgen Inc. to implement the framework of our pharmacokinetics model, with refinements to the parameter values for the elimination rates specific to their mABs, and compare the model predictions to their in-house *in vivo* pharmacokinetics measurements, which we cannot disclose at the moment.

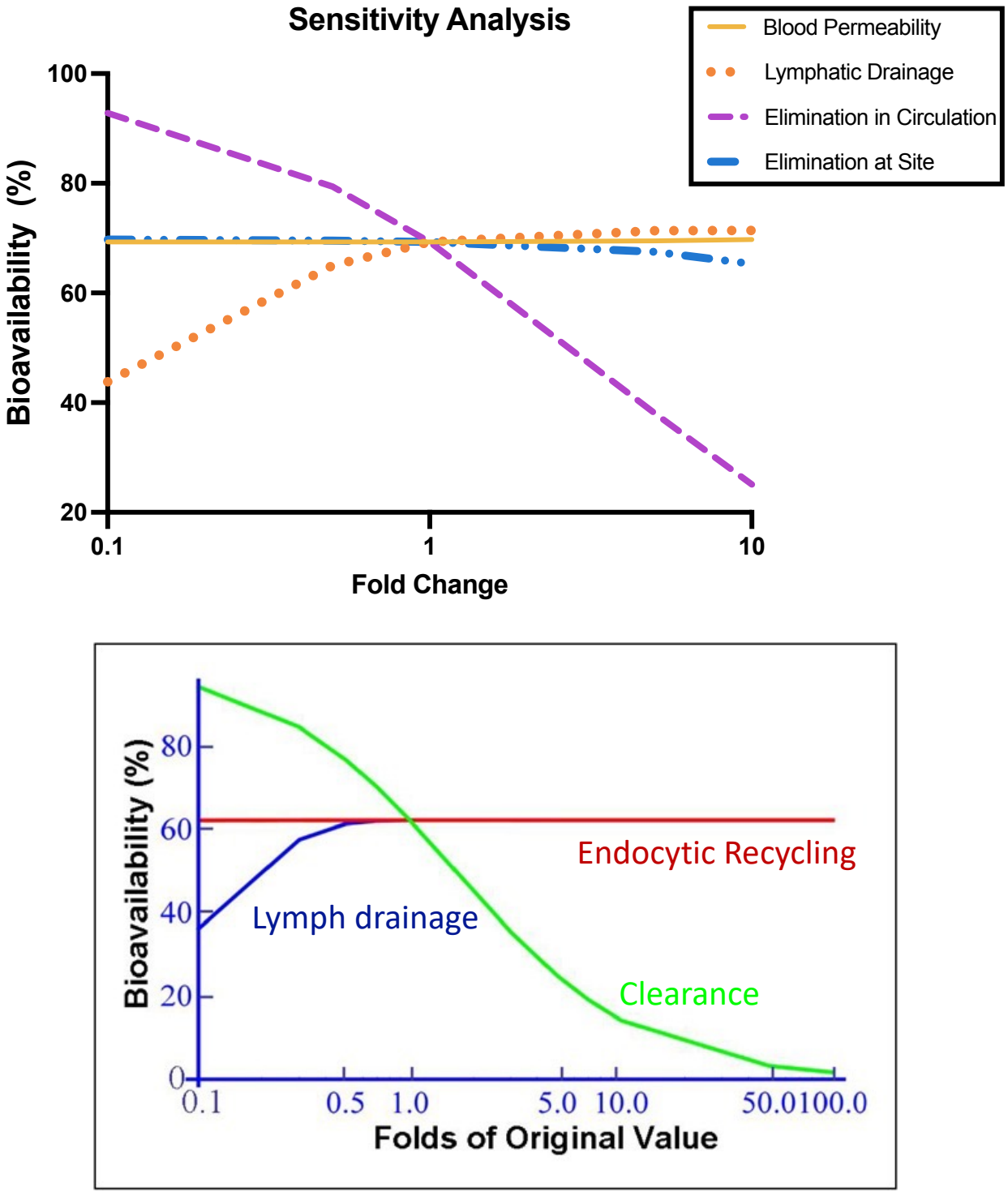

Figure 47: Sensitivity analysis plot comparing the corresponding bioavailability to changes in pharmacokinetics parameters from our model (upper) and from a pharmacokinetics model implementing *in vivo* values[178] (lower).

We also performed a sensitivity analysis to measure the relative contribution of the pharmacokinetics parameters on the bioavailability (**Figure 47**). From this analysis, we were able to identify parameters, such as the blood vascular permeability and local elimination rate, that had minimal to no effects on the bioavailability, within the value ranges studied. Whereas, slower lymphatic drainage would contribute to a lower bioavailability, which is attributed to longer times that the mABs are exposed to local elimination kinetics at the subcutaneous compartment, thus depleting the total amount of mABs prior to entering the systemic circulation. However, the dominant factor determining the bioavailability of the mAB corresponds to the elimination rate in the systemic blood compartment. Thus, strategies to minimize the degradation and filtration of mABs once they are in the host circulation, would maximize the bioavailability, and likely its therapeutic response. Additionally, we compared our sensitivity analysis output to that performed by other studies, where *in vivo* values are implemented for the pharmacokinetics modelling[178]. Remarkably, we found a high degree of agreement between our model output and the sensitivity predictions from the physiological-based model (**Figure 47**). Thus, validating the physiological-relevance of our measured vascular absorption rates and our mathematical pharmacokinetics framework.

Since the framework of the model allows us to account for different schemes in the volumetric distribution of the physiological system and host, we can scale-up our analysis to human biodistribution studies. For this, the larger volumes corresponding to human physiology would be implemented in combination with clinically-measured reaction and elimination kinetics[179,182]. Additionally, such model can be implemented to optimize treatments strategies, such as dosing concentration and time intervals between injections, as well as predicting the physiological transport of other therapeutic agents, including low-molecular weight drugs and growth factors[179,182].

Chapter 6: Conclusions and Future Work

In this thesis, we address the need for a physiologically relevant *in vitro* model that recapitulates critical aspects of the *in vivo* lymphatics, including their tissue architecture and physio-/pathological transport functionality. For this purpose, we implemented microfluidic-based cell culture system that allowed us to compartmentally culture the lymphatics under the appropriate biological stimuli to induce their self-organization into *in vivo*-like capillaries. Furthermore, we leveraged the capabilities of our microfluidic system to recreate the transport of fluid, interstitial solutes and immune cells to perform biological assays for functional characterization and validation of the on-chip entered lymphatics. Following our biological studies, we successfully recapitulated key biological mechanisms in the physiology of lymphatics and its pathological implications. Thus, rendering our microphysiological platform amenable for pre-clinical applications that would be technically challenging to perform with *in vivo* models, such as our study on the subcutaneous vascular absorption of therapeutic antibodies.

From our first set of studies in Chapter 2, we utilize our microfluidic platform to develop an optimized protocol for tissue engineering lymphatic capillaries into a microphysiological system, under either biochemical- or mechanotransduction-based lymphangiogenic stimulus. However, such platform also finds utility for drug screening lymphangiogenesis inhibitors[183], given that draining lymphatic capillaries, at the tumor microenvironment, provide disseminating cancer cells with an accessible escape route for metastasis[184]. In fact, initial studies by our lab have elucidated that simultaneous blood- and lymphatic-angiogenesis results in their cooperative invasion; thus, effective treatments to mitigate metastatic cancer should account for the vascular invasion by both systems[185]. Conversely, screening applications with our platform could be focused on developing regenerative medicine strategies for promoting therapeutic lymphangiogenesis to treat reoccurring lymphedema at inflamed tissue sites[186].

Having established the strategies to grow lymphatic microvasculature within our microfluidic system, we further investigated the physiological capabilities of our platform by quantifying the drainage functionality of the engineered lymphatics (Chapter 3). Results from this section validated that our on-chip lymphatics exhibit solute drainage rates within the same magnitudes as *in vivo* measurements. Additionally, we provided experimental and computational results that demonstrate superior drainage functionality in tissue constructs that integrate a physiologically-

engineered lymphatic microvascular bed, as opposed to other systems that incorporate acellular channels as drainage conduits. Beyond physiological, homeostatic conditions, dysfunctional lymphatic drainage plays a crucial role in the pathogenesis of different diseases with the most common being lymphedema. More recently, impaired meningeal lymphatic drainage at the brain parenchyma has been implicated in the progression of Alzheimer disease (AD) due to facilitated beta amyloid accumulation[186,187]. In continuation of AD research work at our lab, additional efforts from this thesis were devoted to developing an AD-meningeal lymphatics on-chip platform (**Figure 48**). Such platform will allow us to probe the pathological implications of lymphatic drainage during AD-amyloid beta accumulation, and blood-brain-barrier dysfunction.

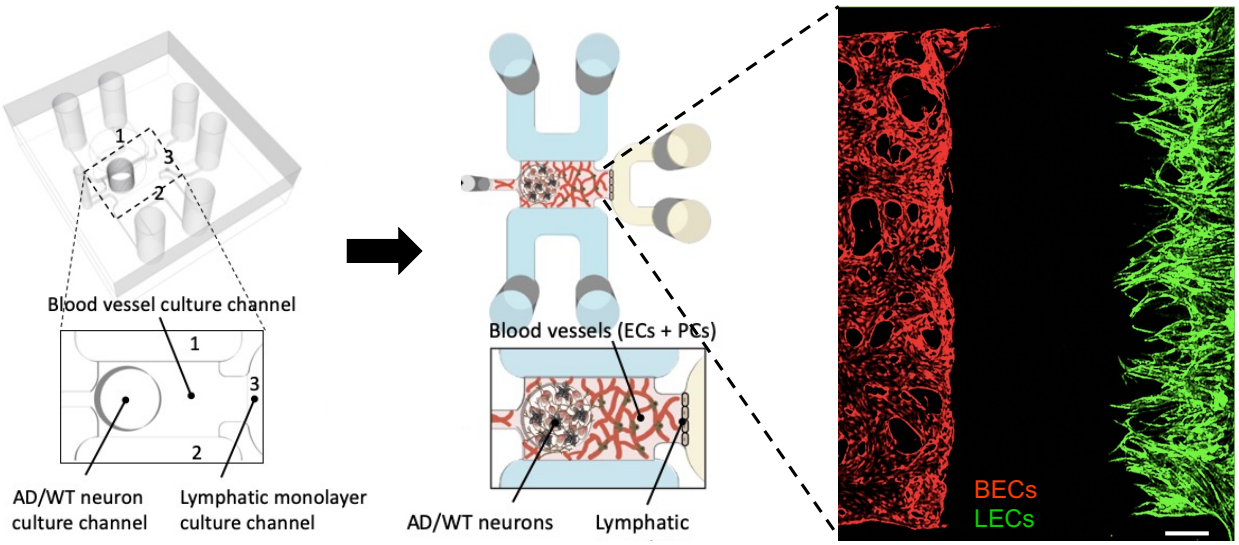

Figure 48: Schematic diagram of the Alzheimer's disease meningeal lymphatics on-chip platform, with a corresponding confocal image of the integration of the blood vasculature (red) and lymphatics (green). Scale bar is 500 µm.

In addition to the uptake of interstitial fluid and macromolecules, the initial lymphatic capillaries provide a crucial pathway for patrolling immune cells to reach lymph node-housed immune cells and activate their immunogenic response against the particular pathogen. From our work in Chapter 4, we recapitulated key aspects of the lymphatic-recruitment of immune cells under inflammatory-chemotactic cues. Since we are able to replicate the co-stimulatory signaling between immune cells and lymphatic capillaries, we could conveniently implement our system to interrogate distinctive chemotactic axes or cell-adhesion molecules that orchestrate the recruitment

of immune cells during the host immune response to a specific pathogenic invasion. Furthermore, in line with our previous work[188], we can utilize this novel platform to screen the immunotherapeutic response of genetically-modified immune cells (GMC-SF-overexpressing dendritic cells[189] or CAR T cells[190]) that transit across the lymphatic interface to reach their corresponding cellular target, either tumor or other immune cells.

In the last study chapter (Chapter 5), we demonstrated the pre-clinical utility of our system to screen the vascular absorption for different therapeutic monoclonal antibodies in order to gain insight into their physiological transport following subcutaneous delivery. Furthermore, we coupled our experimental measurements, for the vascular absorption rate at each vascular interface (blood and lymphatic), with a physiological-based framework to predict the pharmacokinetics of a subcutaneous-delivered dose of the therapeutic antibodies. However, we limited our current study to their pharmacokinetics reaching the systemic circulation. Hence, future efforts by our lab will build upon the fluidic coupling of multiple, organotypic microphysiological platforms[191], thus allowing us to predict the specific uptake of the antibodies to the intended organ/tissue sites. Despite the technological difficulty of performing such study, we can rely on our previously developed microfluidic-based pumping system, MicroHeart[106] (see Appendix 1), which is precisely designed to recapitulate vascular flows in our microphysiological systems; thus, we could connect multiple organotypic-models to this system and replicate the systemic circulation, as well sample the recirculating media to directly quantify and predict the bioavailability of the therapeutics

References

1. Moore, J. E. & Bertram, C. D. Lymphatic System Flows. *Annu. Rev. Fluid Mech.* **50**, 459–482 (2018).
2. Olszewski, W. L. The lymphatic system in body homeostasis: physiological conditions. *Lymphatic research and biology* vol. 1 (2003).
3. Krishnamurty, A. T. & Turley, S. J. Lymph node stromal cells: cartographers of the immune system. *Nature Immunology* vol. 21 369–380 (2020).
4. Cifarelli, V. & Eichmann, A. The Intestinal Lymphatic System: Functions and Metabolic Implications. *CMGH* vol. 7 503–513 (2019).
5. James, J. M., Nalbandian, A. & Mukouyama, Y. suke. TGFβ signaling is required for sprouting lymphangiogenesis during lymphatic network development in the skin. *Dev.* **140**, 3903–3914 (2013).
6. Stacker, S. A. *et al.* Lymphangiogenesis and lymphatic vessel remodelling in cancer. *Nature Reviews Cancer* vol. 14 159–172 (2014).
7. Wiig, H. & Swartz, M. A. Interstitial fluid and lymph formation and transport: Physiological regulation and roles in inflammation and cancer. *Physiological Reviews* vol. 92 1005–1060 (2012).
8. Quick, C. M., Venugopal, A. M., Gashev, A. A., Zawieja, D. C. & Stewart, R. H. Intrinsic pump-conduit behavior of lymphangions. *Am. J. Physiol. - Regul. Integr. Comp. Physiol.* **292**, 1510–1518 (2007).
9. Liao, S. & Padera, T. P. Lymphatic function and immune regulation in health and disease. *Lymphat. Res. Biol.* **11**, 136–143 (2013).
10. Gasteiger, G. & Rudensky, A. Y. Interactions between innate and adaptive lymphocytes. *Nature Reviews Immunology* vol. 14 631–639 (2014).
11. Chaplin, D. D. Overview of the immune response. *J. Allergy Clin. Immunol.* **125**, S3–S23 (2010).
12. Margaris, K. N. & Black, R. A. Modelling the lymphatic system: Challenges and opportunities. *Journal of the Royal Society Interface* vol. 9 601–612 (2012).
13. Zhang, F., Zarkada, G., Yi, S. & Eichmann, A. Lymphatic Endothelial Cell Junctions: Molecular Regulation in Physiology and Diseases. *Frontiers in Physiology* vol. 11 509 (2020).
14. Swartz, M. A. The physiology of the lymphatic system. *Advanced Drug Delivery Reviews* vol. 50 3–20 (2001).
15. Schmid-Schonbein, G. W. Microlymphatics and lymph flow. *Physiological Reviews* vol. 70 987–1028 (1990).
16. Aukland, K. & Reed, R. K. Interstitial-lymphatic mechanisms in the control of extracellular fluid volume. *Physiol. Rev.* **73**, 1–78 (1993).
17. Campbell, K. T. & Silva, E. A. Biomaterial Based Strategies for Engineering New

Lymphatic Vasculature. *Adv. Healthc. Mater.* **9**, 2000895 (2020).

18. Swartz, M. A. & Lund, A. W. Lymphatic and interstitial flow in the tumour microenvironment: Linking mechanobiology with immunity. *Nature Reviews Cancer* vol. 12 210–219 (2012).
19. Stacker, S. A. *et al.* Lymphangiogenesis and lymphatic vessel remodelling in cancer. *Nature Reviews Cancer* vol. 14 159–172 (2014).
20. Jiang, X., Nicolls, M. R., Tian, W. & Rockson, S. G. Lymphatic Dysfunction, Leukotrienes, and Lymphedema. *Annual Review of Physiology* vol. 80 49–70 (2018).
21. Yuan, Y., Arcucci, V., Levy, S. M. & Achen, M. G. Modulation of Immunity by Lymphatic Dysfunction in Lymphedema. *Front. Immunol.* **10**, 76 (2019).
22. Mumprecht, V. & Detmar, M. Lymphangiogenesis and cancer metastasis. *J. Cell. Mol. Med.* **13**, 1405–1416 (2009).
23. Liao, S., von der Weid, P. Y., Network, I. R. & Diseases, S. I. for C. Lymphatic system: an active pathway for immune protection. *Semin. Cell Dev. Biol.* **38**, 83–9 (2015).
24. Stacker, S. A. *et al.* Lymphangiogenesis and lymphatic vessel remodelling in cancer. *Nat. Rev. Cancer* **14**, 159–172 (2014).
25. Tammela, T. & Alitalo, K. Lymphangiogenesis: Molecular Mechanisms and Future Promise. *Cell* **140**, 460–476 (2010).
26. Petrova, T. V *et al.* Lymphatic endothelial reprogramming of vascular endothelial cells by the Prox-1 homeobox transcription factor. *EMBO J.* **21**, 4593–9 (2002).
27. Banerji, S. *et al.* LYVE-1, a new homologue of the CD44 glycoprotein, is a lymph-specific receptor for hyaluronan. *J. Cell Biol.* **144**, 789–801 (1999).
28. Kaipainen, A. *et al.* Expression of the fms-like tyrosine kinase 4 gene becomes restricted to lymphatic endothelium during development. *Proc. Natl. Acad. Sci. U. S. A.* **92**, 3566–70 (1995).
29. Oka, M. *et al.* Inhibition of endogenous TGF-beta signaling enhances lymphangiogenesis. *Blood* **111**, 4571–9 (2008).
30. Sabine, A., Saygili Demir, C. & Petrova, T. V. Endothelial Cell Responses to Biomechanical Forces in Lymphatic Vessels. *Antioxid. Redox Signal.* **25**, 451–465 (2016).
31. Ng, C. P., Helm, C.-L. E. & Swartz, M. A. Interstitial flow differentially stimulates blood and lymphatic endothelial cell morphogenesis in vitro. *Microvasc. Res.* **68**, 258–264 (2004).
32. Helm, C.-L. E., Fleury, M. E., Zisch, A. H., Boschetti, F. & Swartz, M. A. Synergy between interstitial flow and VEGF directs capillary morphogenesis in vitro through a gradient amplification mechanism. *Proc. Natl. Acad. Sci. U. S. A.* **102**, 15779–84 (2005).
33. Triacca, V., Güç, E., Kilarski, W. W., Pisano, M. & Swartz, M. A. Transcellular Pathways in Lymphatic Endothelial Cells Regulate Changes in Solute Transport by Fluid Stress. *Circ. Res.* **120**, 1440–1452 (2017).
34. Sabine, A. *et al.* FOXC2 and fluid shear stress stabilize postnatal lymphatic vasculature. *J.*

Clin. Invest. **125**, 3861–3877 (2015).

35. Shields, J. D. *et al.* Autologous Chemotaxis as a Mechanism of Tumor Cell Homing to Lymphatics via Interstitial Flow and Autocrine CCR7 Signaling. *Cancer Cell* **11**, 526–538 (2007).
36. Brown, M. *et al.* Lymphatic exosomes promote dendritic cell migration along guidance cues. *J. Cell Biol.* jcb.201612051 (2018) doi:10.1083/jcb.201612051.
37. El-Ali, J., Sorger, P. K. & Jensen, K. F. Cells on chips. *Nature* **442**, 403–411 (2006).
38. Whitesides, G. M., Ostuni, E., Takayama, S., Jiang, X. & Ingber, D. E. Soft Lithography in Biology and Biochemistry. *Annu. Rev. Biomed. Eng.* **3**, 335–373 (2001).
39. Breslauer, D. N., Lee, P. J. & Lee, L. P. Microfluidics-based systems biology. *Mol. Biosyst.* **2**, 97 (2006).
40. Chin, C. D. *et al.* Microfluidics-based diagnostics of infectious diseases in the developing world. *Nat. Med.* **17**, 1015–1019 (2011).
41. Boussommier-Calleja, A., Li, R., Chen, M. B., Wong, S. C. & Kamm, R. D. Microfluidics: A New Tool for Modeling Cancer–Immune Interactions. *Trends in Cancer* vol. 2 6–19 (2016).
42. Polacheck, W. J., Li, R., Uzel, S. G. M. & Kamm, R. D. Microfluidic platforms for mechanobiology. *Lab Chip* **13**, 2252–67 (2013).
43. Miura, T. & Yokokawa, R. Tissue culture on a chip: Developmental biology applications of self-organized capillary networks in microfluidic devices. *Dev. Growth Differ.* **58**, 505–515 (2016).
44. Zheng, Y. *et al.* In vitro microvessels for the study of angiogenesis and thrombosis. *Proc. Natl. Acad. Sci. U. S. A.* **109**, 9342–7 (2012).
45. Miller, J. S. *et al.* Rapid casting of patterned vascular networks for perfusable engineered three-dimensional tissues. *Nat. Mater.* **11**, 768–774 (2012).
46. Yeon, J. H., Ryu, H. R., Chung, M., Hu, Q. P. & Jeon, N. L. In vitro formation and characterization of a perfusable three-dimensional tubular capillary network in microfluidic devices. *Lab Chip* **12**, 2815 (2012).
47. Hsu, Y.-H., Moya, M. L., Hughes, C. C. W., George, S. C. & Lee, A. P. A microfluidic platform for generating large-scale nearly identical human microphysiological vascularized tissue arrays. *Lab Chip* **13**, 2990 (2013).
48. Sato, M. *et al.* Microcirculation-on-a-Chip: A Microfluidic Platform for Assaying Blood- and Lymphatic-Vessel Permeability. *PLoS One* **10**, e0137301 (2015).
49. Thompson, R. L. *et al.* Design principles for lymphatic drainage of fluid and solutes from collagen scaffolds. *J. Biomed. Mater. Res. Part A* **106**, 106–114 (2018).
50. Ayuso, J. M., Gong, M. M., Skala, M. C., Harari, P. M. & Beebe, D. J. Human Tumor-Lymphatic Microfluidic Model Reveals Differential Conditioning of Lymphatic Vessels by Breast Cancer Cells. *Adv. Healthc. Mater.* **9**, 1900925 (2020).
51. Gong, M. M. *et al.* Human organotypic lymphatic vessel model elucidates

microenvironment-dependent signaling and barrier function. *Biomaterials* **214**, 119225 (2019).

52. Kim, S., Chung, M. & Jeon, N. L. Three-dimensional biomimetic model to reconstitute sprouting lymphangiogenesis in vitro. *Biomaterials* **78**, 115–128 (2016).
53. Chung, M., Ahn, J., Son, K., Kim, S. & Jeon, N. L. Biomimetic Model of Tumor Microenvironment on Microfluidic Platform. *Adv. Healthc. Mater.* **6**, 1700196 (2017).
54. Lee, S. *et al.* Modeling 3D Human Tumor Lymphatic Vessel Network Using High-Throughput Platform. *Adv. Biol.* **5**, 2000195 (2021).
55. Smith, Q. & Gerecht, S. Going with the flow: Microfluidic platforms in vascular tissue engineering. *Current Opinion in Chemical Engineering* vol. 3 42–50 (2014).
56. Serrano, J. C., Gupta, S. K., Kamm, R. D. & Guo, M. In Pursuit of Designing Multicellular Engineered Living Systems: A Fluid Mechanical Perspective. *Annu. Rev. Fluid Mech.* **53**, 411–437 (2021).
57. Polacheck, W. J., German, A. E., Mammoto, A., Ingber, D. E. & Kamm, R. D. Mechanotransduction of fluid stresses governs 3D cell migration. *Proc. Natl. Acad. Sci. U. S. A.* **111**, 2447–2452 (2014).
58. Zervantonakis, I. K. *et al.* Three-dimensional microfluidic model for tumor cell intravasation and endothelial barrier function. *Proc. Natl. Acad. Sci. U. S. A.* **109**, 13515–13520 (2012).
59. Farahat, W. A. *et al.* Ensemble Analysis of Angiogenic Growth in Three-Dimensional Microfluidic Cell Cultures. *PLoS One* **7**, e37333 (2012).
60. Chen, M. B. *et al.* On-chip human microvasculature assay for visualization and quantification of tumor cell extravasation dynamics. *Nat. Protoc.* **12**, 865–880 (2017).
61. Shin, Y. *et al.* Microfluidic assay for simultaneous culture of multiple cell types on surfaces or within hydrogels. *Nat. Protoc.* **7**, 1247–1259 (2012).
62. Leddy, H. A. & Guilak, F. Site-specific molecular diffusion in articular cartilage measured using fluorescence recovery after photobleaching. *Ann. Biomed. Eng.* **31**, 753–760 (2003).
63. Leddy, H. A., Awad, H. A. & Guilak, F. Molecular diffusion in tissue-engineered cartilage constructs: Effects of scaffold material, time, and culture conditions. *J. Biomed. Mater. Res.* **70B**, 397–406 (2004).
64. Samal, P., van Blitterswijk, C., Truckenmüller, R. & Giselbrecht, S. Grow with the Flow: When Morphogenesis Meets Microfluidics. *Adv. Mater.* **31**, 1805764 (2019).
65. Daems, M., Peacock, H. M. & Jones, E. A. V. Fluid flow as a driver of embryonic morphogenesis. *Development (Cambridge, England)* vol. 147 (2020).
66. Rutkowski, J. M. & Swartz, M. A. A driving force for change: interstitial flow as a morphoregulator. *Trends in Cell Biology* vol. 17 44–50 (2007).
67. Boardman, K. C. & Swartz, M. A. Interstitial flow as a guide for lymphangiogenesis. *Circ. Res.* **92**, 801–808 (2003).
68. Goldman, J. *et al.* Regulation of lymphatic capillary regeneration by interstitial flow in

skin. *Am. J. Physiol. Circ. Physiol.* **292**, H2176–H2183 (2007).

69. Chary, S. R. & Jain, R. K. Direct measurement of interstitial convection and diffusion of albumin in normal and neoplastic tissues by fluorescence photobleaching. *Proc. Natl. Acad. Sci. U. S. A.* **86**, 5385–5389 (1989).

70. Wiig, H. & Swartz, M. A. Interstitial fluid and lymph formation and transport: Physiological regulation and roles in inflammation and cancer. *Physiological Reviews* vol. 92 1005–1060 (2012).

71. Wiig, H. Pathophysiology of tissue fluid accumulation in inflammation. *Journal of Physiology* vol. 589 2945–2953 (2011).

72. Carroll, N. J., Jensen, K. H., Parsa, S., Holbrook, N. M. & Weitz, D. A. Measurement of flow velocity and inference of liquid viscosity in a microfluidic channel by fluorescence photobleaching. *Langmuir* **30**, 4868–4874 (2014).

73. Jönsson, P., Jonsson, M. P., Tegenfeldt, J. O. & Höök, F. A method improving the accuracy of fluorescence recovery after photobleaching analysis. *Biophys. J.* **95**, 5334–5348 (2008).

74. Moreno-Arotzena, O., Meier, J., del Amo, C. & García-Aznar, J. Characterization of Fibrin and Collagen Gels for Engineering Wound Healing Models. *Materials (Basel).* **8**, 1636–1651 (2015).

75. Durlofsky, L. & Brady, J. F. Analysis of the Brinkman equation as a model for flow in porous media. *PHYS. FLUIDS* **30**, 3329–3341 (1987).

76. Bacabac, R. G. *et al.* Dynamic shear stress in parallel-plate flow chambers. *J. Biomech.* **38**, 159–167 (2005).

77. Offeddu, G. S. *et al.* Application of Transmural Flow Across In Vitro Microvasculature Enables Direct Sampling of Interstitial Therapeutic Molecule Distribution. *Small* **15**, 1902393 (2019).

78. Li, R. *et al.* Interstitial flow promotes macrophage polarization toward an M2 phenotype. *Mol. Biol. Cell* **29**, 1927–1940 (2018).

79. Costa, A. Permeability-porosity relationship: A reexamination of the Kozeny-Carman equation based on a fractal pore-space geometry assumption. *Geophys. Res. Lett.* **33**, L02318 (2006).

80. Martys, N. & Garboczi, E. J. Length scales relating the fluid permeability and electrical conductivity in random two-dimensional model porous media. *Phys. Rev. B* **46**, 6080–6090 (1992).

81. Lohela, M., Saaristo, A., Veikkola, T. & Alitalo, K. Lymphangiogenic growth factors, receptors and therapies. *Thrombosis and Haemostasis* vol. 90 167–184 (2003).

82. Rauniyar, K., Jha, S. K. & Jeltsch, M. Biology of vascular endothelial growth factor C in the morphogenesis of lymphatic vessels. *Frontiers in Bioengineering and Biotechnology* vol. 6 7 (2018).

83. Güç, E. *et al.* Local induction of lymphangiogenesis with engineered fibrin-binding VEGF-C promotes wound healing by increasing immune cell trafficking and matrix

remodeling. *Biomaterials* **131**, 160–175 (2017).

84. Cao, R. *et al.* Hepatocyte growth factor is a lymphangiogenic factor with an indirect mechanism of action. *Blood* **107**, 3531–3536 (2006).

85. Kajiya, K., Hirakawa, S., Ma, B., Drinnenberg, I. & Detmar, M. Hepatocyte growth factor promotes lymphatic vessel formation and function. *EMBO J.* **24**, 2885–2895 (2005).

86. Nguyen, V. P. K. H. *et al.* Differential response of lymphatic, venous and arterial endothelial cells to angiopoietin-1 and angiopoietin-2. *BMC Cell Biol.* **8**, 10 (2007).

87. Kajiya, K. *et al.* Promotion of lymphatic integrity by angiopoietin-1/Tie2 signaling during inflammation. *Am. J. Pathol.* **180**, 1273–1282 (2012).

88. Wu, X. & Liu, N. *THE ROLE OF ANG/TIE SIGNALING IN LYMPHANGIOGENESIS*. *Lymphology* vol. 59 https://journals.uair.arizona.edu/index.php/lymph/article/view/17004 (2010).

89. Serrano, J. C. Engineering Three-Dimensional Lymphatic Vasculature On-Chip Through Biochemical and Mechanical Stimulus. (Massachusetts Institute of Technology, 2016).

90. Pirbodaghi, T., Vigolo, D., Akbari, S. & DeMello, A. Investigating the fluid dynamics of rapid processes within microfluidic devices using bright-field microscopy. *Lab Chip* **15**, 2140–2144 (2015).

91. Shayan, R. *et al.* A system for quantifying the patterning of the lymphatic vasculature. *Growth Factors* **25**, 417–425 (2007).

92. Betterman, K. L. & Harvey, N. L. Histological and morphological characterization of developing dermal lymphatic vessels. in *Methods in Molecular Biology* vol. 1846 19–35 (Humana Press Inc., 2018).

93. Lutter, S., Xie, S., Tatin, F. & Makinen, T. Smooth muscle-endothelial cell communication activates Reelin signaling and regulates lymphatic vessel formation. *J. Cell Biol.* **197**, 837–849 (2012).

94. Maier, A. K. B. *et al.* Netrin-4 mediates corneal hemangiogenesis but not lymphangiogenesis in the mouse-model of suture-induced neovascularization. *Investig. Ophthalmol. Vis. Sci.* **58**, 1387–1396 (2017).

95. Taniguchi, K. *et al.* Suppression of Sproutys Has a Therapeutic Effect for a Mouse Model of Ischemia by Enhancing Angiogenesis. *PLoS One* **4**, e5467 (2009).

96. Zhang, Y. *et al.* Heterogeneity in VEGFR3 levels drives lymphatic vessel hyperplasia through cell-autonomous and non-cell-autonomous mechanisms. *Nat. Commun.* **9**, 1–15 (2018).

97. Milasan, A., Dallaire, F., Mayer, G. & Martel, C. Effects of LDL Receptor Modulation on Lymphatic Function. *Sci. Rep.* **6**, 1–13 (2016).

98. Wood, L. B., Ge, R., Kamm, R. D. & Asada, H. H. Nascent vessel elongation rate is inversely related to diameter in in vitro angiogenesis. *Integr. Biol.* **4**, 1081 (2012).

99. Zampell, J. C. *et al.* HIF-1α: coordinates lymphangiogenesis during wound healing and in response to inflammation. *FASEB J.* **26**, 1027–1039 (2012).

100. Paavonen, K., Puolakkainen, P., Jussila, L., Jahkola, T. & Alitalo, K. Vascular endothelial growth factor receptor-3 in lymphangiogenesis in wound healing. *Am. J. Pathol.* **156**, 1499–1504 (2000).

101. Clark, R. Fibrin and Wound Healing. *Ann. N. Y. Acad. Sci.* **936**, 355–367 (2006).

102. Frye, M. *et al.* Matrix stiffness controls lymphatic vessel formation through regulation of a GATA2-dependent transcriptional program. *Nat. Commun.* **9**, 1–16 (2018).

103. Wufsus, A. R., MacEra, N. E. & Neeves, K. B. The hydraulic permeability of blood clots as a function of fibrin and platelet density. *Biophys. J.* **104**, 1812–1823 (2013).

104. Walker-Samuel, S. *et al.* Investigating low-velocity fluid flow in tumors with convection-MRI. *Cancer Res.* **78**, 1859–1872 (2018).

105. Vickerman, V. & Kamm, R. D. Mechanism of a flow-gated angiogenesis switch: early signaling events at cell–matrix and cell–cell junctions. *Integr. Biol.* **4**, 863 (2012).

106. Offeddu, G. S. *et al.* Microheart: A microfluidic pump for functional vascular culture in microphysiological systems. *J. Biomech.* **119**, 110330 (2021).

107. JACKSON, D. G. Biology of the lymphatic marker LYVE-1 and applications in research into lymphatic trafficking and lymphangiogenesis. *APMIS* **112**, 526–538 (2004).

108. Wigle, J. T. *et al.* An essential role for Prox1 in the induction of the lymphatic endothelial cell phenotype. *EMBO J.* **21**, 1505–1513 (2002).

109. Pan, Y. & Xia, L. Emerging roles of podoplanin in vascular development and homeostasis. *Frontiers of Medicine* vol. 9 421–430 (2015).

110. Petrova, T. V. & Koh, G. Y. Biological functions of lymphatic vessels. *Science (80-.).* **369**, (2020).

111. Swartz, M. A. & Fleury, M. E. Interstitial Flow and Its Effects in Soft Tissues. *Annu. Rev. Biomed. Eng.* **9**, 229–256 (2007).

112. Mendola, A. *et al.* Mutations in the VEGFR3 Signaling Pathway Explain 36% of Familial Lymphedema. *Mol. Syndromol.* **4**, 257–266 (2013).

113. Morfoisse, F. *et al.* Lymphatic vasculature requires estrogen receptor-α signaling to protect from lymphedema. *Arterioscler. Thromb. Vasc. Biol.* **38**, 1346–1357 (2018).

114. Sano, M. *et al.* Potential role of transforming growth factor-beta 1/Smad signaling in secondary lymphedema after cancer surgery. *Cancer Sci.* **111**, 2620–2634 (2020).

115. Arita, A. *et al.* Signaling pathways in lymphoma: Pathogenesis and therapeutic targets. *Future Oncology* vol. 9 1549–1571 (2013).

116. Trevaskis, N. L., Kaminskas, L. M. & Porter, C. J. H. From sewer to saviour-targeting the lymphatic system to promote drug exposure and activity. *Nature Reviews Drug Discovery* vol. 14 781–803 (2015).

117. Pain, S. J. *et al.* Quantification of Lymphatic Function for Investigation of Lymphedema: Depot Clearance and Rate of Appearance of Soluble Macromolecules in Blood. *J. Nucl. Med.* **43**, (2002).

118. O'Mahony, S. *et al.* Imaging of Lymphatic Vessels in Breast Cancer–Related

Lymphedema: Intradermal Versus Subcutaneous Injection of 99mTc-Immunoglobulin. *Am. J. Roentgenol.* **186**, 1349–1355 (2006).

119. Proulx, S. T., Ma, Q., Andina, D., Leroux, J. C. & Detmar, M. Quantitative measurement of lymphatic function in mice by noninvasive near-infrared imaging of a peripheral vein. *JCI Insight* **2**, (2017).

120. Sevick-Muraca, E. M., Kwon, S. & Rasmussen, J. C. Emerging lymphatic imaging technologies for mouse and man. *Journal of Clinical Investigation* vol. 124 905–914 (2014).

121. Andres, R. Y. & Schubiger, P. A. Radiolabelling of antibodies: Methods and limitations. *NuklearMedizin* **25**, 162–166 (1986).

122. Polomska, A. K. & Proulx, S. T. Imaging technology of the lymphatic system. *Advanced Drug Delivery Reviews* (2020) doi:10.1016/j.addr.2020.08.013.

123. Brambilla, D., Proulx, S. T., Marschalkova, P., Detmar, M. & Leroux, J.-C. Microneedles for the Noninvasive Structural and Functional Assessment of Dermal Lymphatic Vessels. *Small* **12**, 1053–1061 (2016).

124. Doan, T. N., Bernard, F. C., McKinney, J. M., Dixon, J. B. & Willett, N. J. Endothelin-1 inhibits size dependent lymphatic clearance of PEG-based conjugates after intra-articular injection into the rat knee. *Acta Biomater.* **93**, 270–281 (2019).

125. Polomska, A. K. *et al.* Minimally invasive method for the point-of-care quantification of lymphatic vessel function. *JCI insight* **4**, (2019).

126. Zbyszynski, P., Toraason, I., Repp, L. & Kwon, G. S. Probing the subcutaneous absorption of a PEGylated FUD peptide nanomedicine via in vivo fluorescence imaging. *Nano Converg.* **6**, 22 (2019).

127. Karaman, S. *et al.* Decline of lymphatic vessel density and function in murine skin during aging. *Angiogenesis* **18**, 489–498 (2015).

128. Jain, A. & Cheng, K. The principles and applications of avidin-based nanoparticles in drug delivery and diagnosis. *Journal of Controlled Release* vol. 245 27–40 (2017).

129. Rothschild, M. A., Oratz, M. & Schreiber, S. S. Serum albumin. *Hepatology* **8**, 385–401 (1988).

130. Rügheimer, L., Hansell, P. & Wolgast, M. Determination of the charge of the plasma proteins and consequent Donnan equilibrium across the capillary barriers in the rat microvasculature. *Acta Physiol.* **194**, 335–339 (2008).

131. Almonte, L., Lopez-Elvira, E. & Baró, A. M. Surface-Charge Differentiation of Streptavidin and Avidin by Atomic Force Microscopy-Force Spectroscopy. *ChemPhysChem* **15**, 2768–2773 (2014).

132. Wiig, H., Kolmannskog, O., Tenstad, O. & Bert, J. L. Effect of charge on interstitial distribution of albumin in rat dermis in vitro. *J. Physiol.* **550**, 505–514 (2003).

133. Weinbaum, S., Cancel, L. M., Fu, B. M. & Tarbell, J. M. The Glycocalyx and Its Role in Vascular Physiology and Vascular Related Diseases. *Cardiovasc. Eng. Technol.* **12**, 37–71 (2021).

134. Kedem, O. & Katchalsky, A. Thermodynamic analysis of the permeability of biological membranes to non-electrolytes. *BBA - Biochim. Biophys. Acta* **27**, 229–246 (1958).

135. Zelman, A. Membrane Permeability: Generalization of the Reflection Coefficient Method of Describing Volume and Solute Flows. *Biophys. J.* **12**, 414–419 (1972).

136. Tarbell, J. M. Mass Transport in Arteries and the Localization of Atherosclerosis. *Annu. Rev. Biomed. Eng.* **5**, 79–118 (2003).

137. Starling, E. H. On the Absorption of Fluids from the Connective Tissue Spaces. *J. Physiol.* **19**, 312–326 (1896).

138. Funamoto, K. *et al.* Endothelial monolayer permeability under controlled oxygen tension. *Integr. Biol.* **9**, 529–538 (2017).

139. Uzel, S. G. M. *et al.* Simultaneous or Sequential Orthogonal Gradient Formation in a 3D Cell Culture Microfluidic Platform. *Small* **12**, 612–622 (2016).

140. Rutili, G. & Arfors, K. -E. Protein Concentration in Interstitial and Lymphatic Fluids from the Subcutaneous Tissue. *Acta Physiol. Scand.* **99**, 1–8 (1977).

141. Jackson, D. G. Leucocyte trafficking via the lymphatic vasculature-mechanisms and consequences. *Frontiers in Immunology* vol. 10 471 (2019).

142. Teijeira, A. *et al.* T Cell Migration from Inflamed Skin to Draining Lymph Nodes Requires Intralymphatic Crawling Supported by ICAM-1/LFA-1 Interactions. *Cell Rep.* **18**, 857–865 (2017).

143. Wilhelm, D. L. Mechanisms responsible for increased vascular permeability in acute inflammation. *Agents Actions* **3**, 297–306 (1973).

144. Hampton, H. R. & Chtanova, T. Lymphatic migration of immune cells. *Frontiers in Immunology* vol. 10 1168 (2019).

145. Miteva, D. O. *et al.* Transmural flow modulates cell and fluid transport functions of lymphatic endothelium. *Circ. Res.* **106**, 920–931 (2010).

146. Sokol, C. L. & Luster, A. D. The chemokine system in innate immunity. *Cold Spring Harb. Perspect. Biol.* **7**, 1–20 (2015).

147. Turner, M. D., Nedjai, B., Hurst, T. & Pennington, D. J. Cytokines and chemokines: At the crossroads of cell signalling and inflammatory disease. *Biochimica et Biophysica Acta - Molecular Cell Research* vol. 1843 2563–2582 (2014).

148. Mitra, B. *et al.* Microdevice integrating innate and adaptive immune responses associated with antigen presentation by dendritic cells. *RSC Adv.* **3**, 16002–16010 (2013).

149. Wang, Y. & Irvine, D. J. Convolution of chemoattractant secretion rate, source density, and receptor desensitization direct diverse migration patterns in leukocytes. *Integr. Biol.* **5**, 481–494 (2013).

150. Nandagopal, S., Wu, D. & Lin, F. Combinatorial Guidance by CCR7 Ligands for T Lymphocytes Migration in Co-Existing Chemokine Fields. *PLoS One* **6**, e18183 (2011).

151. Ricart, B. G., John, B., Lee, D., Hunter, C. A. & Hammer, D. A. Dendritic Cells Distinguish Individual Chemokine Signals through CCR7 and CXCR4. *J. Immunol.* **186**,

53–61 (2011).

152. Lin, F. & Butcher, E. C. T cell chemotaxis in a simple microfluidic device. *Lab Chip* **6**, 1462–1469 (2006).

153. Petrova, T. V. & Koh, G. Y. Organ-specific lymphatic vasculature: From development to pathophysiology. *Journal of Experimental Medicine* vol. 215 35–49 (2018).

154. Mizutani, C. M. *et al.* Formation of the BMP activity gradient in the drosophila embryo. *Dev. Cell* **8**, 915–924 (2005).

155. Ruhrberg, C. *et al.* Spatially restricted patterning cues provided by heparin-binding VEGF-A control blood vessel branching morphogenesis. *Genes Dev.* **16**, 2684–2698 (2002).

156. Patel, D. D. *et al.* Chemokines have diverse abilities to form solid phase gradients. *Clin. Immunol.* **99**, 43–52 (2001).

157. Schumann, K. *et al.* Immobilized chemokine fields and soluble chemokine gradients cooperatively shape migration patterns of dendritic cells. *Immunity* **32**, 703–713 (2010).

158. Weber, M. *et al.* Interstitial dendritic cell guidance by haptotactic chemokine gradients. *Science (80-.).* **339**, 328–332 (2013).

159. Ashe, H. L. & Briscoe, J. The interpretation of morphogen gradients. *Development* vol. 133 385–394 (2006).

160. Oudin, M. J. & Weaver, V. M. Physical and chemical gradients in the tumor microenvironment regulate tumor cell invasion, migration, and metastasis. *Cold Spring Harb. Symp. Quant. Biol.* **81**, 189–205 (2016).

161. Fleury, M. E., Boardman, K. C. & Swartz, M. A. Autologous morphogen gradients by subtle interstitial flow and matrix interactions. *Biophys. J.* **91**, 113–121 (2006).

162. Petrie Aronin, C. E. *et al.* Migrating Myeloid Cells Sense Temporal Dynamics of Chemoattractant Concentrations. *Immunity* **47**, 862-874.e3 (2017).

163. Schwarz, J. *et al.* Dendritic Cells Interpret Haptotactic Chemokine Gradients in a Manner Governed by Signal-to-Noise Ratio and Dependent on GRK6. *Curr. Biol.* **27**, 1314–1325 (2017).

164. Wang, Y. & Irvine, D. J. Convolution of chemoattractant secretion rate, source density, and receptor desensitization direct diverse migration patterns in leukocytes. *Integr. Biol. (United Kingdom)* **5**, 481–494 (2013).

165. Weiner, G. J. Building better monoclonal antibody-based therapeutics. *Nature Reviews Cancer* vol. 15 361–370 (2015).

166. Sánchez-Félix, M., Burke, M., Chen, H. H., Patterson, C. & Mittal, S. Predicting bioavailability of monoclonal antibodies after subcutaneous administration: Open innovation challenge. *Advanced Drug Delivery Reviews* vol. 167 66–77 (2020).

167. De Cock, E. *et al.* A time and motion study of subcutaneous versus intravenous trastuzumab in patients with HER2-positive early breast cancer. *Cancer Med.* **5**, 389–397 (2016).

168. Viola, M. *et al.* Subcutaneous delivery of monoclonal antibodies: How do we get there? *Journal of Controlled Release* vol. 286 301–314 (2018).

169. Bittner, B., Richter, W. & Schmidt, J. Subcutaneous Administration of Biotherapeutics: An Overview of Current Challenges and Opportunities. *BioDrugs* vol. 32 425–440 (2018).

170. Sharma, N., Saifi, M. A., Singh, S. B. & Godugu, C. In vivo studies: toxicity and biodistribution of nanocarriers in organisms. in *Nanotoxicity* 41–70 (Elsevier, 2020). doi:10.1016/b978-0-12-819943-5.00003-8.

171. Offeddu, G. S., Shin, Y. & Kamm, R. D. Microphysiological models of neurological disorders for drug development. *Current Opinion in Biomedical Engineering* vol. 13 119–126 (2020).

172. Boswell, C. A. *et al.* Effects of charge on antibody tissue distribution and pharmacokinetics. *Bioconjugate Chemistry* vol. 21 2153–2163 (2010).

173. Crowell, S. R. *et al.* Influence of charge, hydrophobicity, and size on vitreous pharmacokinetics of large molecules. *Transl. Vis. Sci. Technol.* **8**, 1–1 (2019).

174. Kagan, L. Pharmacokinetic modeling of the subcutaneous absorption of therapeutic proteins. *Drug Metabolism and Disposition* vol. 42 1890–1905 (2014).

175. Yellepeddi, V. *et al.* State-of-the-Art Review on Physiologically Based Pharmacokinetic Modeling in Pediatric Drug Development. *Clinical Pharmacokinetics* vol. 58 1–13 (2019).

176. Wolak, D. J., Pizzo, M. E. & Thorne, R. G. Probing the extracellular diffusion of antibodies in brain using in vivo integrative optical imaging and ex vivo fluorescence imaging. *J. Control. Release* **197**, 78–86 (2015).

177. Urva, S. R., Yang, V. C. & Balthasar, J. P. Physiologically based pharmacokinetic model for T84.66: A monoclonal anti-CEA antibody. *J. Pharm. Sci.* **99**, 1582–1600 (2010).

178. Zhao, L., Ji, P., Li, Z., Roy, P. & Sahajwalla, C. G. The Antibody Drug Absorption Following Subcutaneous or Intramuscular Administration and Its Mathematical Description by Coupling Physiologically Based Absorption Process with the Conventional Compartment Pharmacokinetic Model. *J. Clin. Pharmacol.* **53**, 314–325 (2013).

179. Baxter, L. T., Zhu, H., Mackensen, D. G., Butler, W. F. & Jain, R. K. Biodistribution of Monoclonal Antibodies: Scale-up from Mouse to Human Using a Physiologically Based Pharmacokinetic Model. *Cancer Res.* **55**, (1995).

180. Kota, J. *et al.* Lymphatic absorption of subcutaneously administered proteins: Influence of different injection sites on the absorption of darbepoetin alfa using a sheep model. *Drug Metab. Dispos.* **35**, 2211–2217 (2007).

181. McLennan, D. N. *et al.* Lymphatic absorption is the primary contributor to the systemic availability of epoetin alfa following subcutaneous administration to sheep. *J. Pharmacol. Exp. Ther.* **313**, 345–351 (2005).

182. Zhao, L., Ji, P., Li, Z., Roy, P. & Sahajwalla, C. G. The Antibody Drug Absorption Following Subcutaneous or Intramuscular Administration and Its Mathematical Description by Coupling Physiologically Based Absorption Process with the Conventional Compartment Pharmacokinetic Model. *J. Clin. Pharmacol.* **53**, 314–325 (2013).

183. Duong, T., Koopman, P. & Francois, M. Tumor lymphangiogenesis as a potential therapeutic target. *Journal of Oncology* (2012) doi:10.1155/2012/204946.

184. Achen, M. G., McColl, B. K. & Stacker, S. A. Focus on lymphangiogenesis in tumor metastasis. *Cancer Cell* vol. 7 121–127 (2005).

185. Osaki, T., Serrano, J. C. & Kamm, R. D. Cooperative Effects of Vascular Angiogenesis and Lymphangiogenesis. *Regen. Eng. Transl. Med.* **4**, 120–132 (2018).

186. Norrmén, C., Tammela, T., Petrova, T. V. & Alitalo, K. Biological basis of therapeutic lymphangiogenesis. *Circulation* **123**, 1335–1351 (2011).

187. Yamakawa, M. *et al.* Potential lymphangiogenesis therapies: Learning from current antiangiogenesis therapies-A review. *Med. Res. Rev.* **38**, 1769–1798 (2018).

188. Fang, T. *et al.* Remodeling of the Tumor Microenvironment by a Chemokine/Anti-PD-L1 Nanobody Fusion Protein. *Mol. Pharm.* **16**, 2838–2844 (2019).

189. Van De Laar, L., Coffer, P. J. & Woltman, A. M. Regulation of dendritic cell development by GM-CSF: Molecular control and implications for immune homeostasis and therapy. *Blood* vol. 119 3383–3393 (2012).

190. June, C. H., O'Connor, R. S., Kawalekar, O. U., Ghassemi, S. & Milone, M. C. CAR T cell immunotherapy for human cancer. *Science* vol. 359 1361–1365 (2018).

191. Herland, A. *et al.* Quantitative prediction of human pharmacokinetic responses to drugs via fluidically coupled vascularized organ chips. *Nat. Biomed. Eng.* **4**, 421–436 (2020).

Appendix A: MATLAB Code for Estimating the Pressures and Flow Rates in the MicroHeart Pump System [1]

An additional contribution, from this thesis work, was the development of a microfluidic-based pump which allows for the controlled delivery of media for vascular microphysiological applications (**Figure 49**). A theoretical framework was developed based on lumped element analysis to predict the performance of the pump for different fluidic configurations and a finite element model of the included check-valves (**Figure 49**). In the MATLAB algorithm provided below, the full framework describing the functionality of this micropump system is analyzed by the lumped element parameters and equations, thus the code can be extended to predict and optimize the operation of the MicroHeart for a variety of microphysiological systems

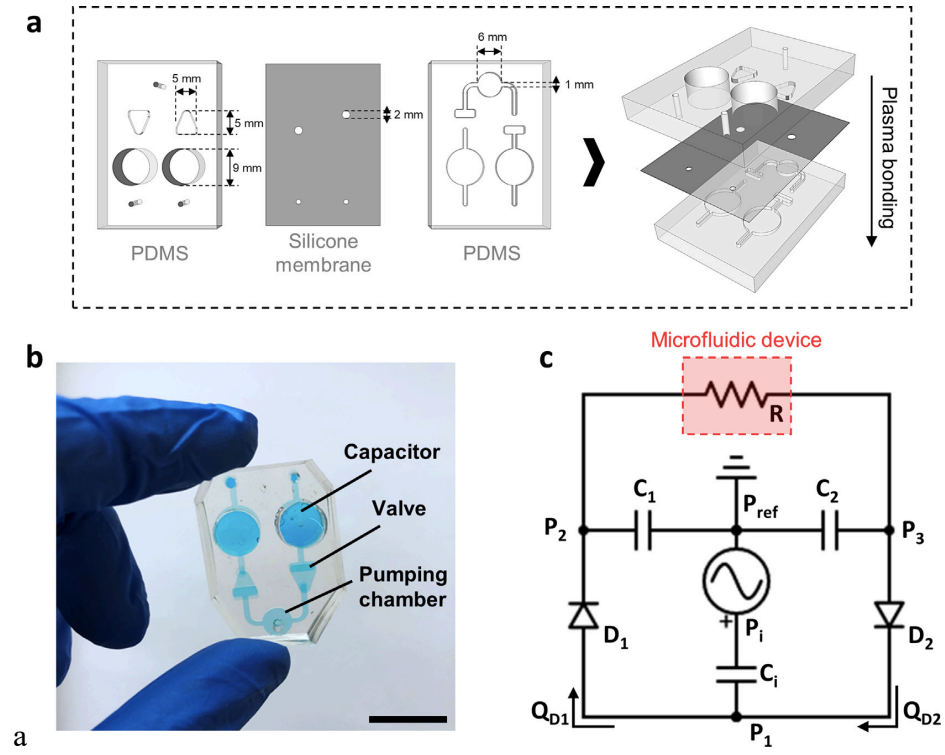

Figure 49: (a) Schematic representation of the MicroHeart fabrication and (b) photograph of the fully assembled MicroHeart. The scale bar is 1 cm. (c) Analogous electrical circuit used for lumped element modeling of flow in the MicroHeart.[106]

[1] Parts of this section have been previously published. See reference [106].

```
function Y_prime = Microheart_ODEs(t,Y)

global Rc Rch Rn Cin C1 C2 P T k Pth mu Ld Wd;

% % Note: User can change Rn to Rc depending on the connected system

Y_prime = zeros(3,1); % to ensure a column vector

% extract states
P1 = Y(1);
P2 = Y(2);
P3 = Y(3);

% generate input pressure derivative
tt = mod(t,T); % to produce a periodic waveform
if (tt<(0.1))
dPin = P/(0.1);
elseif (tt<(0.5*T)-0.1)
dPin = 0;
elseif (tt<0.5*T)
dPin = -P/(0.1);
else
dPin = 0;
end

% determine diode flows
if (P1-P2>400)
Rd1=(12*mu*(Ld))/((Wd)*((k)*((P1-P2)))^3);
Q1=(P1-P2)/(Rc+Rd1);
else
Q1=0;
end
if (P3-P1>400)
Rd2=(12*0.00078*(Ld))/((Wd)*((k)*((P3-P1)))^3);
Q4=(P3-P1)/(Rc+Rd2);
else
Q4=0;
end

% systems of ODEs
Y_prime(1) = -((Q1-Q4)/Cin) + dPin;
Y_prime(2) = ((Q1-((P2-P3)/(Rn)))/C1);
Y_prime(3) = ((-Q4+((P2-P3)/Rn))/C2);


------
```

```
clc,clear;

% % Description:
% Using an analogy to electrical circuits and Ohm's Law,
% this program provides the volumetric flow rates as well as the pressure
% distribution across a microfluidic pump (Microheart).

% % Written by Jean C. Serrano @ the Massachusetts Institute of Technology

% define global parameters
global Rc Rn Cin C1 C2 P T Rch k Pth mu Ld Wd;

% % Global System Parameters
mu= 0.00078; % media viscosity [Pa*s]


% % Microvascular Networks Parameters
Rn1= 0.000015; % initial radius of networks (at post entrance)[m]

Rn2= 0.000010; % radius of networks across the gel [m]

% for networks in minimacro device

Ln1= 0.0005; % length of networks at post (shorter section)[m]

Ln2= 0.002; % length of networks across the gel [m]

% % % for networks in microfluidic device
% %
% Ln1= 0.0002; % length of networks at post (shorter section)[m]
%
% Ln2= 0.0009; % length of networks across the gel [m]


% % Microfluidic Device Parameters
Lc= 0.02; % length of the media channel [m]

Wc= 0.001; % width of the media channel [m]

Hc= 0.001; % height of the media channel [m]


% % MicroHeart internal Channel Parameters
Lch= 0.01; % length of the media channel [m]

Wch= 0.002; % width of the media channel [m]

Hch= 0.0001; % height of the media channel [m]


% % Membrane Capacitors Parameters
am=0.0024;%(c(2,1))*0.001; % pump capacitor diaphragm radius [m]

a1=0.0047;%(c(3,1))*0.001; % capacitor 1 diaphragm radius [m]
```

```
a2=0.0047;%(c(4,1))*0.001; % capacitor 2 diaphragm radius [m]

v=0.5; % membrane Poisson's ratio

E=2145000; % membrane Young's Modulus [Pa]

Hm=0.000300; % plate thickness [m]

% % Check-Valve Parameters (Diode)

k=7e-8; % inverse plate stiffens [m/Pa]

Pth=400; % threshold pressure [Pa]

Ld= 0.002; % length of the valve channel [m]

Wd= 0.002; % width of the valve channel [m]

% Calculation of Hydraulic Resistance Values

Rch=(12*mu*(Lch))/((Wch)*(Hch)^3); % MicroHeart fluidic channels

Rc=(8*mu*Lc)/((pi())*(Hc)^4);

Rn1c=(8*mu*Ln1)/((pi())*(Rn1)^4);

Rn2c=(8*mu*Ln2)/((pi())*(Rn2)^4);

RT2=Rn2c/5;

RT1=(2*Rn1c)+RT2;

% for networks in minimacro device

Rn=RT1/60;

% % for networks in microfluidic
%
% Rn=RT1/20;

% % Calculation of Hydraulic Capacitance Values

Cin=((am^6)*(1-(v^2))*pi)/(16*E*(Hm^3));

C1=((a1^6)*(1-(v^2))*pi)/(16*E*(Hm^3));

C2=((a2^6)*(1-(v^2))*pi)/(16*E*(Hm^3));
```

```
% % Applied/Input Pressure Parameters

P=2000; % input pumping pressure [Pa]

T=1; % inverse pumping frequency [s]


% % Solve system ODEs

P1_init = 0;
P2_init = 0;
P3_init = 0;

[time,y_out] = ode23s('Microheart_ODEs',[0:0.00000001:4], [P1_init P2_init
P3_init]);


% Plot Input Pressure Time Derivative (for validation), Pressure Distribution
% and Flow Rate or Fluid Velocity

f = zeros(size(time));
tt = mod(time,T);
for ii = 1:length(f)
if (tt(ii) < (0.1))
f(ii) = P/(0.1);
elseif (tt(ii) < (0.5*T)-0.1)
f(ii) = 0;
elseif (tt(ii) < (0.5*T))
f(ii) = -P/(0.1);
else
f(ii) = 0;
end
end

tiledlayout(2,2)

nexttile
plot(time, f), xlabel ("time (s)"), ylabel("P (Pa)");

nexttile
plot(time,y_out(:,1),time,y_out(:,2),time, y_out(:,3),'LineWidth',2)
xlabel ("time (s)");
ylabel("P (Pa)");
legend('P1','P2','P3');

Q=(y_out(:,2)-y_out(:,3))/Rn; % Replace with Rc if its flow within
microfluidic channel
V=(Q/300)/(((pi())*(Rn2)^2))*1000;
% V=(Q/(Wch*Hch))*1000; % Velocity within microfluidic channel
nexttile([1 2])
plot(time,V,'LineWidth',2);
xlabel("time (s)");
% ylabel("Shear Stress (Pa)");
% ylabel("Flow Rate (m^{3}/s)");
ylabel("Flow Velocity (mm/s)");
```

Appendix B: MATLAB Code for Estimating the On-Chip Steady State Vascular Transport and Protein Concentration

This appendix displays the MATLAB code used to solve the transport analysis detailed in Chapter 3, Section 3. The algorithm allows the user to specify experimental conditions regarding the transport properties and microfluidic chip geometry, corresponding to their particular set up, and estimate the required blood intravascular pressure to establish physiological interstitial fluid flow and the interstitial steady state concentration (normalized to the blood intravascular content) of the plasma protein or therapeutic biologic of interest.

```
% % Description:
% Steady state fluid and solute transport analysis in a microfluidic system
% with an integrated blood and lymphatic microvascular model
% in the same chip. This analysis concerns the transport across the gel
% region from the blood vascular domain to the lymphatic outlet.

% % Written by Jean C. Serrano @ the Massachusetts Institute of Technology

 clc, clear;

% % Parameters

Hg= 0.005; % length of the gel channel [m]

Wg= 0.0005; % width of the gel channel [m]

mu= 0.00078; % media viscosity [Pa*s]

k=4e-14; % hydraulic permeability of gel [m^2]

LpB=1e-11; % hydraulic conductivity of the blood microvasculature [m/Pa.s]

S_VB=4000; % blood vascular surface area per unit tissue volume [1/m]

LpL=8e-6; % hydraulic conductivity of the blood microvasculature [m/Pa.s]

S_VL=7000; % blood vascular surface area per unit tissue volume [1/m]

uf=0.0000001; % physiological interstitial fluid velocity [m/s]

PB=4e-10; % blood vasculature diffusive permeability to albumin [m/s]

sigma_b=0.8; % blood vasculature reflection coefficient to albumin [1]

sigma_l=0.2; % lymphatic vasculature reflection coefficient to albumin [1]
```

```
Cb=1; % experimental concentration of blood intravascular albumin [mg/mL]

% % Equations for fluid transport

syms Pb Pg0 Pgw
eqn1 = (k/mu)*(Pg0-Pgw)/Wg == uf;
eqn2 = LpB*S_VB*Hg*(Pb-Pg0) == uf;
eqn3 = LpL*S_VL*Hg*(Pgw) == uf;


% % Solutions for fluid pressures

sol = solve([eqn1, eqn2, eqn3], [Pb, Pg0, Pgw]);
Pb_Sol = double(sol.Pb); % intravascular pressure in blood microvasculature
Pg0_Sol = double(sol.Pg0); % interstitial pressure adjacent to blood
microvasculature
Pgw_Sol = double(sol.Pgw); % interstitial pressure adjacent to lymph
microvasculature

disp ('Required blood intravascular pressure (in Pascals relative to the
lymphatic outlet pressure) to establish physiological flow')
Pb_s=round(Pb_Sol,0);
disp(Pb_s)

% % Equation for mass transport
syms Cg
eqn4 = (PB*S_VB*Hg*(Cb-Cg))+(uf*(1-sigma_b)*Cb) == (1-sigma_l)*uf*Cg;


% % Solution for interstitial gel region concentration

Cg_sol = double(solve(eqn4, Cg));

disp('Steady state normalized concentration (relative to blood intravascular
content) of albumin in the interstitial space')
Cg_s=round(Cg_sol,2);
disp(Cg_s)
```

Appendix C: MATLAB Code for Pharmacokinetics Modelling of Monoclonal Antibody Distribution and Bioavailability

We implemented a series of ordinary differential equations, as described in Chapter 5, to describe the physiological-based pharmacokinetics of subcutaneously-delivered monoclonal antibodies. The model considers the exchange across 4 different, physiological compartments: subcutaneous tissue, local blood vasculature, local lymphatic vasculature and systemic-circulating plasma. The transport across compartments is defined by physiological processes, as defined in Chapter 5. The MATLAB code below solves the system of differential equations that describes the rate change in concentration within each compartment, and outputs the normalized species amount at each compartment and the maximum systemic bioavailability.

```
function dydt=PK_ODEs(t,y)

global SDR P SV tau_L kEB kES Vd Vp DC phiB phiL Vtiss Vinter; % Transport
Parameters

dydt=zeros(3,1); % to ensure a column vector

% Compartment Volumes

Vtiss=4/3*pi*(((3*Vd/(4*pi))^(1/3))+((6*DC*t)^0.5))^(3);

Vinter=Vtiss*(1-phiB-phiL);


% System ODEs
dydt(1)=(-y(1)*SDR)-(P*SV*(y(1)-y(3)))+(-y(1)*kES)+(12*pi*DC*y(1)*(1-phiB-
phiL)*(((((3*Vd/(4*pi))^(1/3))+((6*DC*t)^0.5)))^2)*((6*DC*t)^-0.5))/Vinter;

dydt(2)=(y(1)*Vinter*SDR)-y(2)*((1/tau_L));

dydt(3)=((P*SV*Vinter*(y(1)-y(3)))+(y(2)*(1/tau_L))-(kEB*Vp*y(3)))/Vp;


end

-----
```

```
% % Description:
% Pharmacokinetic modelling of monoclonal antibody biodistribution
% based on vascular transport measurements from on-chip
% dermal blood and lymphatic microvasculature.

% % Written by Jean C. Serrano @ the Massachusetts Institute of Technology

clc,clear;

% % Define global parameters
global SDR P SV tau_L kEB kES Vd Vp DC phiB phiL Vinter; % Transport
Parameters

% % System Transport Parameters
Vd=5e-7; % dose volume [m^-3]

Vp=5e-3; % total plasma volume [m^-3]

DC=5e-12;% diffusion coefficient of IgG [m^2/s]

phiB=0.2; % blood vascular volume fraction [1]

phiL=0.15; % lymphatic volume fraction [1]

P=(6.83268E-08)/100; % blood vasculature diffusive permeability [m/s]

SDR=0.01881/60; % lymphatic solute drainage rate [1/s]

SV=7000; % blood vascular surface area per unit tissue volume [1/m]

tau_L=(3*3600); % lymphatic to plasma transit time[1/s]

kEB=0.025/3600; % elimination/dispostion rate from blood [1/s]

kES=0.0025/3600; % elimination/dispostion rate from site [1/s]


% Solve PK ODEs to initial SC concentration

Cdose = 1; % administered dose concentration [mg/mL]
Csc_init = (Cdose); % subcutaneous dose concentration [mg/mL]
CL_init = 0; % initial concentration in lymphatics [mg/mL]
CB_init = 0; % initial concentration in local blood [mg/mL]

[time,y_out] = ode23s('PK_ODEs',(0.000001:25*3600), [Csc_init CL_init
CB_init]);


% Compartment Volumes

Vtiss=4/3*pi.*(((3*Vd/(4*pi))^(1/3))+((6*DC*time).^0.5)).^(3);

Vinter=Vtiss*(1-phiB-phiL);
```

```
% Species Amount Values

Xsc=y_out(:,1).*Vd;

XL=y_out(:,2);

XB=y_out(:,3).*Vp;

% Plot Profiles

p=plot(time/3600,Xsc/(Cdose*Vd),time/3600,XL/(Cdose*Vd),time/3600,
XB/(Cdose*Vd),'LineWidth',2);
xlabel ("Time (hr)");
ylabel("Normalized Species Amount");
set(gca,'FontSize',15)
set(gca,'fontname','Agency FB')
lgd=legend('X_S_C','X_L','X_B');
lgd.FontSize = 14;
p(1).LineWidth = 2.5;
p(2).LineWidth = 2.5;
p(3).LineWidth = 2.5;

Bioavailability=100*(max(XB))/(Cdose*Vd)
```